Summer 2022

Study of Radiative Corrections in the MUon Scattering Experiment

Lin Li

Study of Radiative Corrections in the Muon Scattering Experiment

by

Lin Li

Bachelor of Science
Henan University, China, 2009

Master of Physical Electronics
Chinese Academy of Sciences, China, 2013

Submitted in Partial Fulfillment of the Requirements

for the Degree of Doctor of Philosophy in

Physics

College of Arts and Sciences

University of South Carolina

2022

Accepted by:

Steffen Strauch, Major Professor

Ralf Gothe, Committee Member

Fred Myhrer, Committee Member

Michael Kohl, Committee Member

Tracey L. Weldon, Vice Provost and Dean of the Graduate School

Acknowledgments

It would be impossible for me to finish my work without many people's support and help during this long journey, especially during this unprecedented pandemic and subsequent events. So I would like to take the chance to thank them one by one.

First, I want to show my greatest gratitude to Prof. Steffen Strauch, who is my dissertation advisor. He introduced me to the world of nuclear physics shortly after I joined the team in 2015. Then based on his recommendation, I started to contribute to the MUSE project. He is always full of wisdom and energy. I still remember the days when he explained how to understand the physics behind the MUSE experiment and how to move forward with this project. He is very nice and patient. There are several times that I was blocked by software setup and configuration, or by code flow, it is Dr. Strauch who promptly helped me out. So I appreciate his endless support and help in my research, life and my family. Thank you from the bottom of my heart.

I would like to thank my thesis committee members: Prof. Ralf Gothe, Prof. Fred Myhrer and Prof. Michael Kohl for their valuable comments and suggestions on the detector construction and theory discusstions on this work.

I would like to thank Pulak Talukdar and Yannick Ulrich on the theory support. The discussions about theoritical predictions on the radiative corrections with them are very helpful to this work.

I would like to thank Dr. Yodanka Ilieva for organizing the group meeting every week. Not only the research suggestions but also her kindness, makes our group a family. I would like to thank the former graduate students Colin Gleason, Aneta Netz, Tongtong Cao, and Hao Jiang for their support when I first joined in this

group. I would like to thank my office mates Nicolas Recalde, Brandon Tumeo and Anne Flannery for the discussions during the days before the pandemic. Especially for Anne, thank you for taking care of the scintillator detectors we made together while I cannot travel to PSI.

I would like to thank my coworkers in the MUSE collaboration. Many of them I don't have opportunities to meet with. It is a good experience to work with them to strive for the same goal. Ethan Cline and Ievgen Lavrukhin, whom I talked with before, their passion on research inspires me to challenge myself.

Finally, I want to show my gratitude and appreciation to my parents and my husband. They support me behind endlessly and help me to form who I am.

This work is supported in parts by the U.S. National Science Foundation: NSF PHY-2111050. The MUSE experiment is supported by the U.S. Department of Energy, the U.S. National Science Foundation, the Paul Scherrer Institute, and the US-Israel Binational Science Foundation.

Abstract

The root-mean-square (rms) radius of the proton charge is a fundamental quantity. In 2010, the studies of muonic hydrogen with high precision found a notably smaller value than the one from earlier non-muonic measurements. This discrepancy has led to theoretical and experimental investigations. A missing measurement in determining the proton radius is muon scattering, a measurement that the MUon Scattering Experiment (MUSE) collaboration proposed at Paul Scherrer Institute (PSI). MUSE will measure elastic electron-proton and muon-proton scattering data with positively and negatively charged beams in a four-momentum-transfer square range from $Q^2 = 0.002$ to 0.08 GeV^2. Each of the four sets of data will allow the extraction of the proton charge radius. In combination, the data test possible differences between the electron and muon interactions and additionally two-photon exchange effects.

MUSE uses a large acceptance detector system without a magnetic spectrometer. As the final-state lepton momentum remains unmeasured, the MUSE acceptance is integrated over a range of final-state lepton momenta to obtain the cross section. To extract the Born cross section, which contains the form factors, the radiative corrections in MUSE need to be determined. An event generator (ESEPP) is used in the target position to simulate the $\ell^{\pm}p \to \ell^{\pm}p$ and $\ell^{\pm}p \to \ell^{\pm}p\gamma$ processes and to study the radiative corrections for both electrons and muons. A dedicated downstream photon detector is introduced to suppress initial-state radiation effects by detecting the events with a hit in the detector that has a photon energy above the photon detector threshold.

The results show that, with the help of the photon calorimeter, the radiative corrections to the Born cross section are below 0.1 for electrons and 0.01 for muons under MUSE conditions. The radiative corrections for electrons are reduced by a factor of 3 using the photon calorimeter. The total uncertainties of the radiative corrections due to the knowledge of the setup in the experiment for electron scattering are smaller than 0.5%, while angular-dependent uncertainties related to the proton radius extraction for electrons are smaller than 0.38%. The total uncertainties of the radiative corrections from the uncertainties in the experimental input for muons are less than 0.05%. Due to this work, the relative systematic cross-section uncertainties of MUSE are enabled to be of tolerable size.

Table of Contents

Acknowledgments iii

Abstract v

List of Tables ix

List of Figures x

Chapter 1 Introduction 1

1.1 Measurements of the Proton Charge Radius 1

1.2 MUon Scattering Experiment 5

1.3 Radiative Corrections 7

Chapter 2 MUSE Setup 10

2.1 PSI πM1 Beamline 10

2.2 Beamline Detectors 12

2.3 Target 18

2.4 Scattered Particle Spectrometer 19

Chapter 3 Radiative Corrections 23

3.1 General Theory of Elastic Lepton-Proton Scattering 23

3.2 Radiative Corrections to Elastic Lepton-Proton Scattering 28

3.3 ESEPP Event Generator 31

3.4 $\ell^{\pm}p \to \ell'^{\pm}p'\gamma$ Distribution in MUSE Kinematics 33

3.5 Physics Models Comparison 37

3.6 Discussion 46

Chapter 4 Experimental Parameters that affect Radiative Corrections 49

4.1 Minimalistic Simulation with ESEPP Event Generator 49

4.2 Beam Momentum 50

4.3 Detector Properties 51

4.4 Uncertainties of Experiment Parameters 62

Chapter 5 Analysis and Results 63

5.1 ESEPP Simulation 63

5.2 Radiative Corrections for $\ell^{-}p$ scattering data in MUSE Kinematics . 65

5.3 Uncertainties of Radiative Corrections from ESEPP Simulation . . . 69

5.4 Cross Section Asymmetries 71

Chapter 6 Summary and Outlook 74

Bibliography 77

Appendix A SPS Construction and Time Resolution Measurement 88

List of Tables

Table 1.1 Estimated MUSE relative systematic uncertainties 8

Table 2.1 Design parameters for the scintillator walls 21

Table 3.1 Example of the input parameters of ESEPP in MUSE Kinematic . 33

Table 3.2 The integrated cross section from McMule for electrons 46

Table 3.3 The integrated cross section from McMule for muons 46

Table 4.1 SPS detection threshold $p'_{\min}$ for e^- 60

Table 4.2 SPS detection threshold $p'_{\min}$ for μ^- 60

Table 4.3 The uncertainties of experiment parameters 62

Table 5.1 Radiative corrections for ep scattering 68

Table 5.2 Radiative corrections for μp scattering 68

Table 5.3 Contribution to the uncertainties of radiative corrections from $p'_{\min}$ for ep scattering and various photon-calorimeter sizes 70

Table 5.4 Uncertainties of radiative corrections for e^-p scattering 71

Table 5.5 Uncertainties of radiative corrections for μ^-p scattering 71

List of Figures

Figure 1.1 Recent proton charge-radius results 4

Figure 1.2 Anticipated data for G_E relative to the dipole form factor for MUSE 6

Figure 2.1 The πM1 magnetic channel at PSI 11

Figure 2.2 Sketch of the MUSE experimental setup 12

Figure 2.3 BH detector for MUSE 13

Figure 2.4 Average time resolution of one BH plane 14

Figure 2.5 GEM detectors for MUSE 14

Figure 2.6 Beamline VETO detector for MUSE 15

Figure 2.7 Beam Monitor for MUSE 16

Figure 2.8 Photon calorimeter for MUSE 17

Figure 2.9 MUSE liquid hydrogen target system and performance 18

Figure 2.10 Straw Tube Tracker for MUSE 19

Figure 2.11 Scattered-particle scintillators for MUSE 20

Figure 2.12 Time resolution of SPS detectors 22

Figure 3.1 Kinematic diagram for elastic lepton-proton scattering in the lab frame 23

Figure 3.2 The one-photon exchange (Born term) Feynman diagram for elastic lepton-proton scattering 25

Figure 3.3 The Feynman diagrams representing the elastic scattering process 29

Figure 3.4 The Feynman diagrams representing the first-order bremsstrahlung processes 30

Figure 3.5 The ep cross section with elastic peak and radiative tail from the ESEPP event generator 35

Figure 3.6 The μp cross section with elastic peak and radiative tail from the ESEPP event generator 36

Figure 3.7 Photon distribution of photon polar angle versus photon energy from the ESEPP event generator 38

Figure 3.8 Relative radiative corrections vs the value of the scattering lepton kinetic energy for elastic ep and μp scattering 40

Figure 3.9 Comparison between ESEPP and Darklight event generator . . . 42

Figure 3.10 Comparison between ESEPP event generator and χPT calculation 44

Figure 3.11 Three cases of $\ell^{\pm}p \to \ell'^{\pm}p'\gamma$ from ESEPP in Geant4 simulation . 47

Figure 4.1 A sketch of a minimalistic simulation in MUSE shows the first-order bremsstrahlung process $\ell^{\pm}p \to \ell'^{\pm}p'\gamma$ 49

Figure 4.2 Examples of simulated scattering-angle resolutions 51

Figure 4.3 Nominal SPS front-wall acceptance 53

Figure 4.4 A schematic view of the measurement of the attenuation length with a source or hit position at y and light output signals at the up and down PMTs 54

Figure 4.5 Example of Geant4 simulation to study energy deposition of SPS 56

Figure 4.6 Simulated energy deposition for scattered leptons 57

Figure 4.7 The SPS efficiency as a function of scattering angle at various discriminator thresholds 58

Figure 4.8 Geant4 simulation estimates the geometrical acceptance 58

Figure 4.9 Estimated SPS momentum-detection efficiency 59

Figure 4.10 Example of the light-output signal of the calorimeter 61

Figure 4.11 Calorimeter light-output signal and resolution as a function of electron beam momentum 61

Figure 5.1 ESEPP simulation results 64

Figure 5.2 Simulated $ep \to ep\gamma$ photon distributions at the front face of the calorimeter 65

Figure 5.3 Simulated $\mu p \to \mu p\gamma$ photon distributions at the front face of the calorimeter 66

Figure 5.4 The radiative corrections for ep scattering 67

Figure 5.5 The radiative corrections for μp scattering 67

Figure 5.6 Cross section asymmetries for the differential cross sections 72

Figure 5.7 Cross section asymmetries for the integrated cross sections 73

Figure A.1 SPS construction processes 89

Figure A.2 A schematic view of the three-bar cosmic-ray method used to determine the counter's time resolution 90

Figure A.3 Example of a mean-time difference for three long SPS detectors . 91

Figure A.4 Rearrangement of the six counters to symmetrize the system of equations with normal order and complementary order 92

Figure A.5 Examples of time-resolution results from cosmic-ray measurements for a long bar and for a short bar 93

Chapter 1

Introduction

1.1 Measurements of the Proton Charge Radius

Ever since Rutherford demonstrated the positively-charged atomic nucleus experimentally in 1911 [1], the protons have been recognized as the basic building blocks of atomic nuclei. In the Standard Model of particle physics, protons are known to be composed of three valence quarks with strong force interaction in between. As a fundamental quantity, the proton root-mean-square (rms) charge radius has been studied extensively by experiments and theories to determine its precise value. Two ways are used to measure this value: electron-proton scattering and hydrogen spectroscopy.

Electron proton scattering has been used to probe the structure of the proton since the 1960s. The electron beam is a good tool for investigating the properties of protons since electrons have no substructure. Elastic electron scattering is used to measure the electric and magnetic form factors $G_E(Q^2)$ and $G_M(Q^2)$ [2], where Q^2 is the negative four-momentum transfer squared between electron and proton. The form factors are normalized at $Q^2 = 0$ to the proton's charge and magnetic moment, $G_E(0) = 1$ and $G_M(0) = \mu_p$. With form factors, the Born cross section (one-photon exchange) is given for ultra-relativistic electrons by

$$\frac{\mathrm{d}\sigma_{\mathrm{Born}}}{\mathrm{d}\Omega} = \left(\frac{\mathrm{d}\sigma}{\mathrm{d}\Omega}\right)_{\mathrm{Mott}} \frac{\tau}{\varepsilon(1+\tau)}[G_M^2(Q^2) + \frac{\varepsilon}{\tau}G_E^2(Q^2)], \tag{1.1}$$

where $\tau = \frac{Q^2}{4M^2}$, M is the mass of the proton, and $\varepsilon = [1 + 2(1+\tau)\tan^2(\theta_\ell/2)]^{-1}$ is the virtual photon polarization with the electron scattering angle θ_ℓ. The Mott cross section is the cross section for an electron scattering off a point charge.

The standard method to extract the form factors from measured cross sections is the Rosenbluth separation. The reduced cross section is defined as

$$\left(\frac{\mathrm{d}\sigma}{\mathrm{d}\Omega}\right)_{\mathrm{red}} = G_M^2(Q^2) + \frac{\varepsilon}{\tau}G_E^2(Q^2). \tag{1.2}$$

In a linear fit to the reduced cross section at constant Q^2 but different ε values, $G_E^2(Q^2)/\tau$ can be obtained from the slope of the line and $G_M^2(Q^2)$ can be obtained from the intersection, which means a number of cross section measurements are taken with different values of E and θ, but keeping Q^2 fixed. The root-mean-square charge radius of the proton (proton charge radius) is determined from the slope of the electric form factor at $Q^2 = 0$,

$$\langle r_p^2 \rangle = -6\hbar^2 \left.\frac{\mathrm{d}G_E(Q^2)}{\mathrm{d}Q^2}\right|_{Q^2=0}. \tag{1.3}$$

Another method to extract the proton radius is by atomic hydrogen spectroscopy [3]. In QED, the wave function of the S state of the hydrogen overlaps with the proton, while that of the P state does not. The proton charge radius can be obtained by the comparison between the measured transition frequency and the bound-state QED calculations which isolates the proton finite size term. The energy shift at the S state level is given by [4]

$$\Delta E = \frac{2}{3}\pi\alpha|\Psi_S(0)|^2 r_p^2, \tag{1.4}$$

where $\Psi_S(0)$ is the lepton wave function at the origin of the atom.

Prior to 2010, the results of proton radius obtained from these two methods agreed with each other. In 2010, a high precision electron-proton scattering experiment at Mainz (MAMI) published their result to be 0.8791(79) fm, which enhanced this agreement [5]. The recommended value of proton radius in CODATA-2010 was $r_p =$ 0.8775(51) fm determined from the combination of electron scattering and electronic hydrogen spectroscopy [6]. In the same year, Pohl et al. [7] used laser spectroscopy to measure the difference in energy between the 2S state and 2P state of the muonic

hydrogen (μH) based on the Lamb shift and found $r_p = 0.84184(67)$ fm, which differs by 7 standard deviations from the CODATA-2010 value. Muonic hydrogen is a bound state of a proton and a muon. The overlap between the bound lepton and the proton is proportional to m_r^3, where m_r is the reduced lepton mass. Because the muon mass is 200 times larger than the electron mass, the finite-size contribution in muonic atoms is largely enhanced. This discrepancy was confirmed by [8] which found the radius to be 0.84087(39) fm. Since the two methods are measuring the same observable [9], this discrepancy is called the proton radius puzzle (reviews are in [10, 11]). Many experimental and theoretical discussions arise to solve this puzzle.

From the theoretical side, some scientists suggested the physical calculations for scattering experiments or hydrogen energy levels are not accurate. For example, Pohl guessed that the Rydberg constant, a factor in the calculation of the differences between atomic energy levels, has been misgauged [7]. Some other scientists proposed that the proton radius puzzle might be caused by the difference between the μp and ep interactions which are related to the lepton universality violation. New physics is necessary to explain the constraints from phenomena like the muon g-2 experiment [12, 13, 14], kaon decay [15], the hyperfine structure in muon [16], and J/Ψ decay [17]. Most relevant constraints on lepton universality are discussed in [10, 15, 18].

On the experimental side, new hydrogen spectroscopic measurements and ep scattering data were published. Two new hydrogen-spectroscopy measurements [19, 20] agree with the small radius but one [21] finds a larger value. The result reported from PRad [22], agrees with the small radius value but is in tension with the earlier data from MAMI [5]. The initial-state-radiation experiment at MAMI [23] obtained a larger radius but has too large uncertainties to settle the issue. Different techniques have been used by some investigators to reanalyze the ep scattering data. One result is consistent with the muonic hydrogen spectroscopy value using a flavor dependent quark distribution model [24]. The other obtained a similar value as MAMI by rean-

alyzing the data from the A1 Collaboration using a novel method which relates the radius of the proton to its transverse charge density [25].

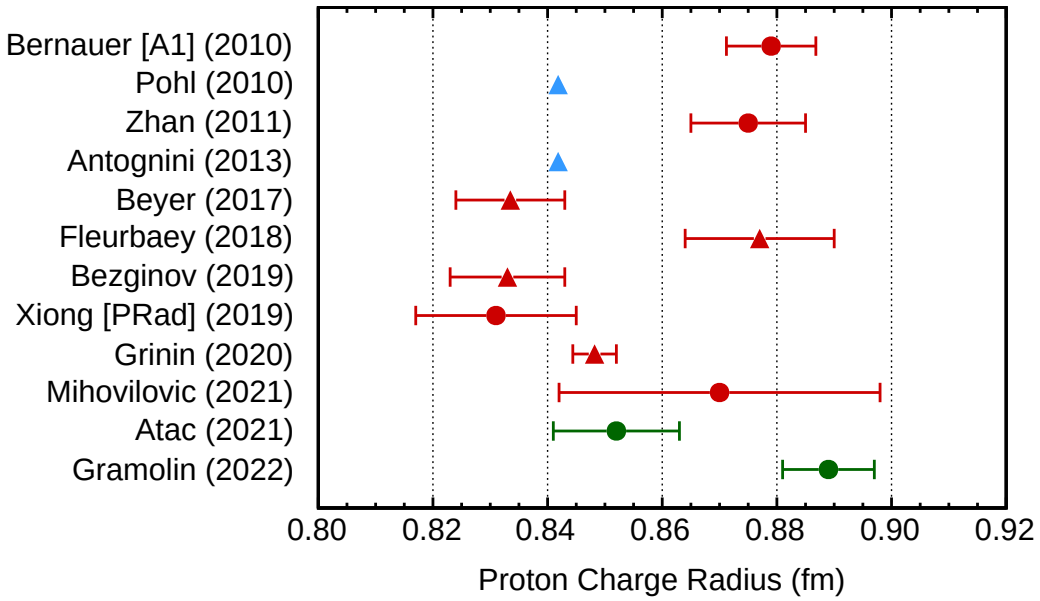

Figure 1.1 Recent proton charge radius results. The red circle results are from electron-proton scattering experiment [5, 26, 22, 23]. The red triangle data is from hydrogen spectroscopy experiment [19, 21, 20, 27]. The blue triangle data is from muonic hydrogen spectroscopy experiment [7, 8]. The green circle results are from reanalyze the *ep* scattering data with different techniques [24, 25].

There are ongoing experiments aiming to extract the proton charge radius. The ULQ2 collaboration [28] at Tohoku University proposed an electron scattering experiment with a 20 to 60 MeV electron beam and scattering angle of 30° to 150°, covering a Q^2 range from 0.0003 to 0.008 GeV^2. The COMPASS collaboration proposed an elastic μp scattering measurement at the high-energy muon beamline at CERN [29]. The experiment uses as a hydrogen target a high-pressure hydrogen-filled time-projection chamber (TPC). The recoil protons will be measured. The Q^2 coverage is from 0.001 to 0.04 GeV^2. An experiment at MAMI will measure *ep* elastic scattering in a Q^2 range from 0.001 to 0.04 GeV^2 [30]. The scattered electron will be measured by a forward tracker and the recoil proton will be measured with a TPC. PRad-II, proposed by the PRad collaboration [31], is an updated experiment

of PRad. It plans to improve the precision in determining the proton charge radius by reducing the statistical and systematic uncertainties. Among these ongoing experiments, a compelling one is the MUon Scattering Experiment (MUSE) which is proposed to run at the Paul Scherrer Institute (PSI) [32].

1.2 MUon Scattering Experiment

The MUon Scattering Experiment (MUSE) at Paul Scherrer Institute (PSI) intends to measure the proton charge radius from elastic electron-proton and muon-proton scattering data with positively and negatively charged beams in a four-momentum-transfer squared range from $Q^2 = 0.002$ to 0.08 GeV^2. First, MUSE is able to extract the proton radius with high precision from both ep and μp scattering measurement, especially it is the first precise μp scattering radius determination. Second, MUSE will test possible differences between the electron and muon interactions even more precisely in the same experiment since some systematic uncertainties cancel when comparing both cases. Finally, MUSE is able to compare cross sections of positive and negative charged particles to test two-photon exchange effects in both ep and μp elastic scattering at the sub-percent level.

Figure 1.2 shows the comparison of the electric form factor among MUSE, PRad [22] and Mainz [5] experiments, along with two selected fits [33]. Mainz used beam energies from 180 to 855 MeV with magnetic spectrometers at relatively large scattering angles, covering Q^2 from 0.004 to 1 GeV^2. PRad used 1.1 and 2.2 GeV electron beams at minimum scattering angles up to 7° to provide the Q^2 region 2×10^{-4} to 6×10^{-2} GeV^2. It can be seen that there is tension between the Mainz and PRad data, and the experiments also report different radii. Furthermore, different fitting methods give different radii for the same data set. MUSE uses beam momenta of 115, 161, and 210 MeV/c with scattering angles covering $20° - 100°$. The proton charge radius will be measured from the μp and ep data simultaneously, so MUSE has the

potential to be sensitive to the differences between the radii extracted from μ and e data with $\sigma(r_e - r_\mu) \approx 0.005$ fm.

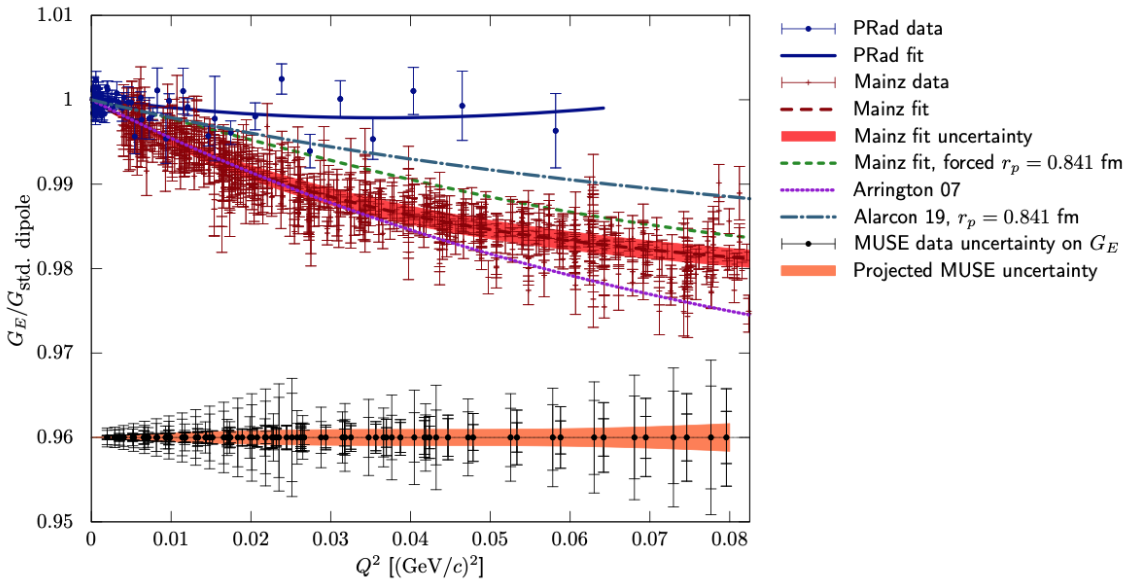

Figure 1.2 Anticipated data for G_E relative to the dipole form factor for MUSE, the PRad [22] and Mainz [5]. The expected values for μ and e are arbitrarily placed at 0.96, and the inner and outer error bars represent the uncertainties for positive and negative lepton charges [33].

MUSE will also compare the cross sections of positive to negative charges to study the two-photon exchange effect. In the ep scattering experiment, two-photon exchange (TPE) is one correction to the cross sections used in the Rosenbluth separation [34]. When calculating the radiative corrections, usually it is convenient to separate the two-photon exchange into "soft" and "hard" parts. The soft approximation means that the interaction of one of the virtual photons has very low momentum transfer, therefore the calculation does not depend on the proton structure, which means it is model-independent. The soft part contains the infrared (IR) divergence, which can be cancelled by adding other radiative correction terms. The remaining "hard" part, which is model-dependent, is hard to calculate from theory. The most direct way to measure the contribution from the hard two-photon exchange is to look for a lepton sign asymmetry in elastic electron-proton scattering. The TPE effect can

be obtained by comparing elastic $\ell^+ p$ and $\ell^- p$ cross sections from experiment. The ratio of positive to negative polarity cross sections [34, 35]

$$\frac{\sigma^{\ell^+ p}}{\sigma^{\ell^- p}} \approx \frac{|\mathcal{M}_\gamma|^2 + 2\mathrm{Re}\Big(\mathcal{M}_\gamma^\dagger \mathcal{M}_{\gamma\gamma}\Big)}{|\mathcal{M}_\gamma|^2 - 2\mathrm{Re}\Big(\mathcal{M}_\gamma^\dagger \mathcal{M}_{\gamma\gamma}\Big)}, \tag{1.5}$$

differs from unity. The fact is that the Born term $\mathcal{M}_\gamma$ changes sign when lepton's charge changes, while the TPE amplitude $\mathcal{M}_{\gamma\gamma}$ does not. Then the interference of the Born and TPE term therefore has the opposite sign for positive and negative lepton. The anticipated systematic uncertainties in the cross-section ratio are 0.2% [32].

1.3 Radiative Corrections

In order to get the Born cross section that includes the information of the proton form factor, higher-order radiative corrections to the Born term need to be applied to correct the measured cross section. At the order of α^2, corresponding to one-photon exchange, the radiative correction is expressed as a factor $1 + \delta$, where δ includes processes from a additional virtual photon or a real bremsstrahlung photons. The standard theoretical calculation of radiative corrections has been well-known for a long time. In 1949, Schwinger first calculated the full first order radiative correction for Coulomb potential scattering [36]. In 1969, Mo and Tsai published their work that summarized the earlier work of Tsai [37], giving a practical and reliable recipe of radiative corrections to elastic and inelastic scattering with soft-photon approximation [38]. In 2000, Maximon and Tjon used no soft-photon approximation in the inelastic cross-section calculation and fewer approximations in two-photon exchange evaluation to improve the calculation. They also included the proton's form factors when calculating the proton vertex correction [39]. The works from Mo and Tsai as well as Maximon and Tjon are considered as the basis of radiative correction and are used widely in elastic scattering experiments. Nowadays, with technique and computation ability increased, higher experimental accuracy is planned to be

achieved. This requires more accurate theory support, for example, including higher order Feynman diagrams, avoiding the soft photon approximation, and not ignoring the lepton mass. Some improved radiative correction theory predictions [40, 41, 42] and event generators [43, 44] will be discussed in the following chapter.

The estimated systematic uncertainties for MUSE are discussed in the MUSE Technical Design Report and given in Table 1.1. It can be seen that the largest con-

Table 1.1 Estimated MUSE relative systematic cross-section uncertainties for the shape of angular distributions, the ratio of muon and electron scattering cross sections, and the ratio of positive- to negative-charge cross sections [32].

Uncertainty	angular distribution (%)	μ/e(%)	+/− (%)
Detector efficiencies	0.1	0.1	0.1
Solid angle	0.1	small	small
Luminosity	small	small	small
Scattering angle offset	0.2	small	small
Multiple scattering correction	0.15	small	small
Beam momentum offset	0.1	0.1	0.1
Radiative correction	0.1 (μ), 0.5 (e)	0.5	small
Magnetic contribution	0.15	small	small
Subtraction of μ decay from μp	0.1	0.1	small
Subtraction of target walls	0.3	small	small
Subtraction of pion-induced events	small	small	small
Beam PID	0.1	0.1	0.1
Subtraction of μ decay from ep	small	small	small
Subtraction of ee from ep	small	small	small
Total	0.5 (μ), 0.7 (e)	0.5	0.2

tributor to the systematic uncertainties is the uncertainty of radiative corrections. A

theory calculation for MUSE estimates that the uncertainty of radiative corrections for μp scattering is 0.1%, and for ep scattering 0.5% [45]. As some systematic uncertainties cancel out when comparing between e and μ scattering or positive and negative polarity, the total anticipated systematic uncertainty for μ/e is 0.5%, which is mainly from radiative corrections. The total anticipated systematic uncertainty for the ratio $+/-$ is 0.2%, where the radiative correction contributions are small. In the MUSE experiment, because there is no magnetic spectrometer, the momenta of the final-state leptons remain unmeasured. For each bin of the scattering angle, MUSE will measure the integrated electron-proton and muon-proton scattering yields that includes all events in the detector acceptance and lepton momenta above the detection threshold p'_{min}

$$\frac{\mathrm{d}\sigma}{\mathrm{d}\Omega_l}(p'_{\text{min}}) = \int_{p'_l}\int_{\Omega_\gamma}\left(\frac{\mathrm{d}\sigma_{\text{brems}}}{\mathrm{d}\Omega_l \mathrm{d}\Omega_\gamma \mathrm{d}p'_l}\right)\mathrm{d}\Omega_\gamma \mathrm{d}p'_l. \tag{1.6}$$

The size of the radiative correction depends on the detector acceptance, its energy resolution, and the kinematic cuts applied to select the scattering events. The uncertainty of the radiative correction results in a relative uncertainty to the cross section. To study the radiative correction, a simulation with an event generator including the detector performance is needed. This dissertation focuses on the understanding of the radiative corrections and their uncertainties based on the knowledge of the detectors in MUSE. The event generator ESEPP [43] has been included in simulations. Chapter 2 provides an introduction to the experimental set up of MUSE in PSI. Chapter 3 introduces the general physics background, and the event generator used to calculate the radiative correction in MUSE. Details of the Monte Carlo simulation, the kinematics, and the properties of detectors related to the radiative correction will be presented in Chapter 4. Chapter 5 discusses the results for the radiative corrections and their uncertainties. Chapter 6 will talk about conclusion and possible future improvements based on the radiative correction results.

Chapter 2

MUSE Setup

2.1 PSI πM1 Beamline

MUSE uses a secondary πM1 beamline provided by the High-Intensity Proton Accelerator (HIPA) at PSI [46]. The πM1 beam channel was designed for high precision pion scattering experiments and the pion beam properties have been well-studied. The beamline elements are shown in Fig. 2.1. The secondary beams are generated by interactions of the primary proton beam at the M1 production target with an angle of 22° relative to the proton beam. The charged muons are from charged pion decay in flight. The production of positrons and electrons is mainly from the electron positron pair production from the decay of neutral pions. The properties of the electron and muon beams were studied and presented in [47, 48]. In order to create clear e, μ and π separation in a 20 ns accelerator Radio Frequency (RF) time interval, MUSE uses beam momenta of around 115, 161 and 210 MeV/c at both positive and negative polarity. These can be achieved by setting the dipole magnets in the channel.

Based on their different masses, the mixed beam particles of e, μ, and π are identified with time-of-flight (TOF) measurements using MUSE timing detectors [49]. The low beam flux requires large angle detectors for the scattered particles. The experiment covers a horizontal angular range from 20° to 100°. Tracking detectors are required to determine the scattering angle. Figure 2.2 shows a Geant4 [50] sketch of the experimental setup for the MUSE experiment. Details about each detector are discussed as follows.

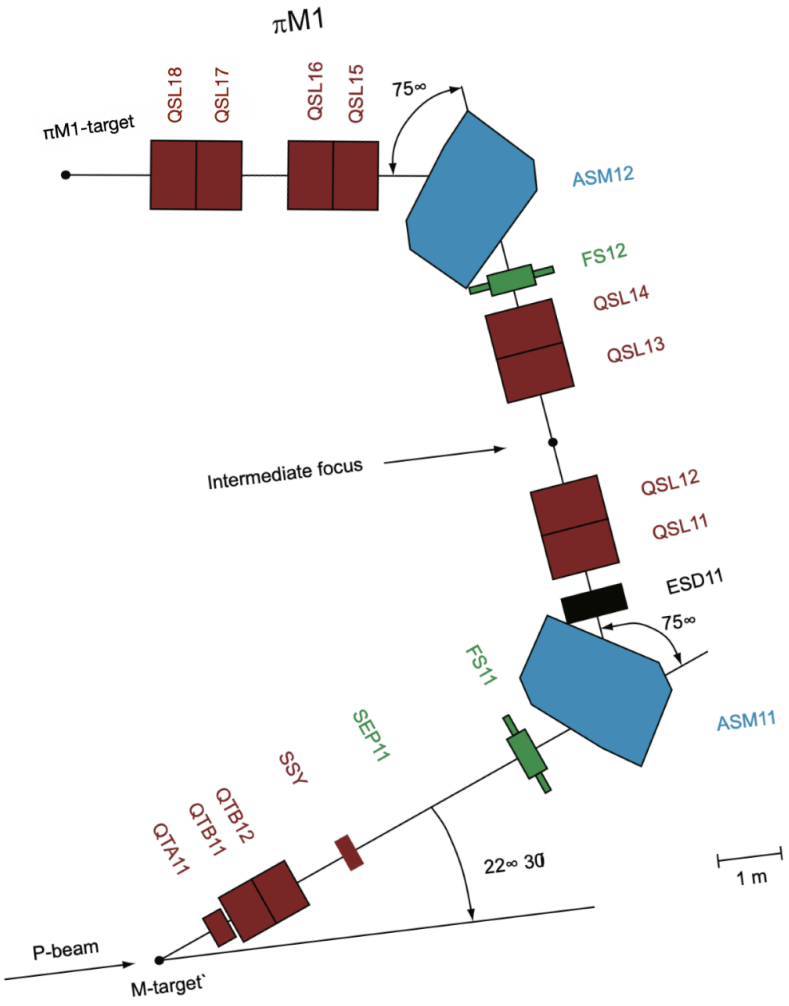

Figure 2.1 πM1 channel elements. The magnets in blue are bending dipoles. The magnets in red are focusing quadrupoles. The jaws in green are used to control the beam flux. The beam dispersion at the Intermediate Focal Point (IFP) is 7 cm/% [47].

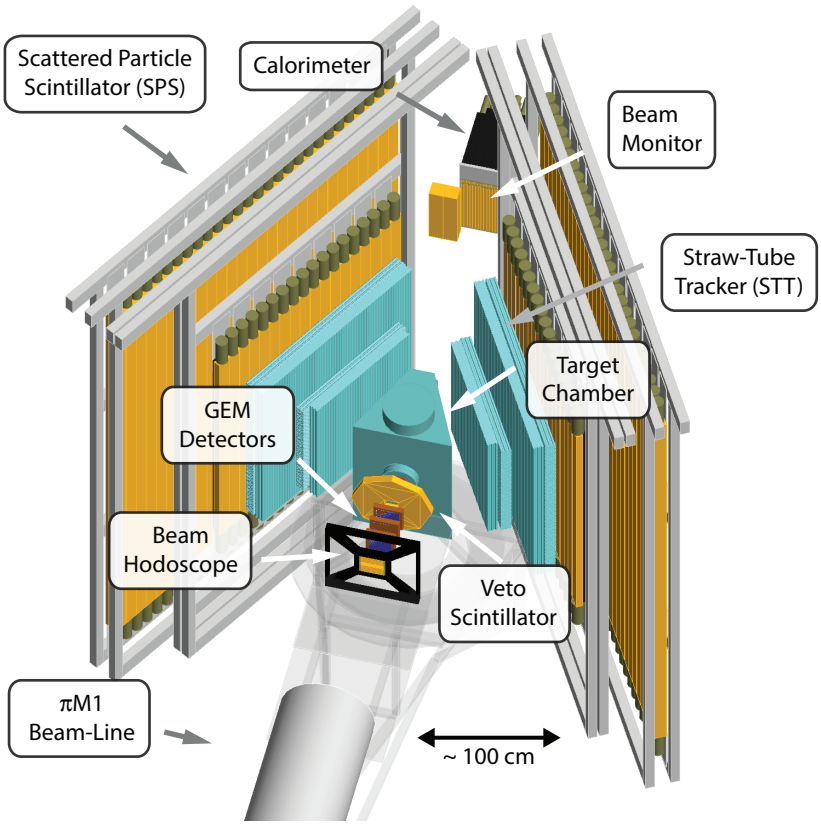

Figure 2.2 Sketch of the MUSE experimental setup at the πM1 beamline at PSI as implemented in the MUSE Geant4 simulation.

2.2 Beamline Detectors

2.2.1 Beam Hodoscope (BH)

The beam hodoscope is the first detector along the upstream beamline. Figure 2.3 left shows a photograph of a BH plane under construction. One type of BH plane comprises sixteen BC-404 plastic scintillator paddles, each 100 mm long $\times$ 2 mm thick, and two ends readout with SiPMs. The six central paddles that are against the more intense central of the beam, are narrower with a width of 4 mm. They are flanked on each side by five 8 mm wide paddles. The other type of plane was

built with thirteen 8-mm wide paddles [49]. The planes are placed in the horizontal and vertical directions to better localize particle hit positions, as shown in Fig. 2.3 right. The beam hodoscope detector is used for timing and particle identification in conjunction with other detectors. The TOF from beam hodoscope to scattered-particle scintillators determines the reaction type (muon scattering vs. muon decay in flight). TOF from the beam hodoscope to the beam monitor identifies backgrounds and determines μ and π beam momenta. The BH also measures the beam-particle flux.

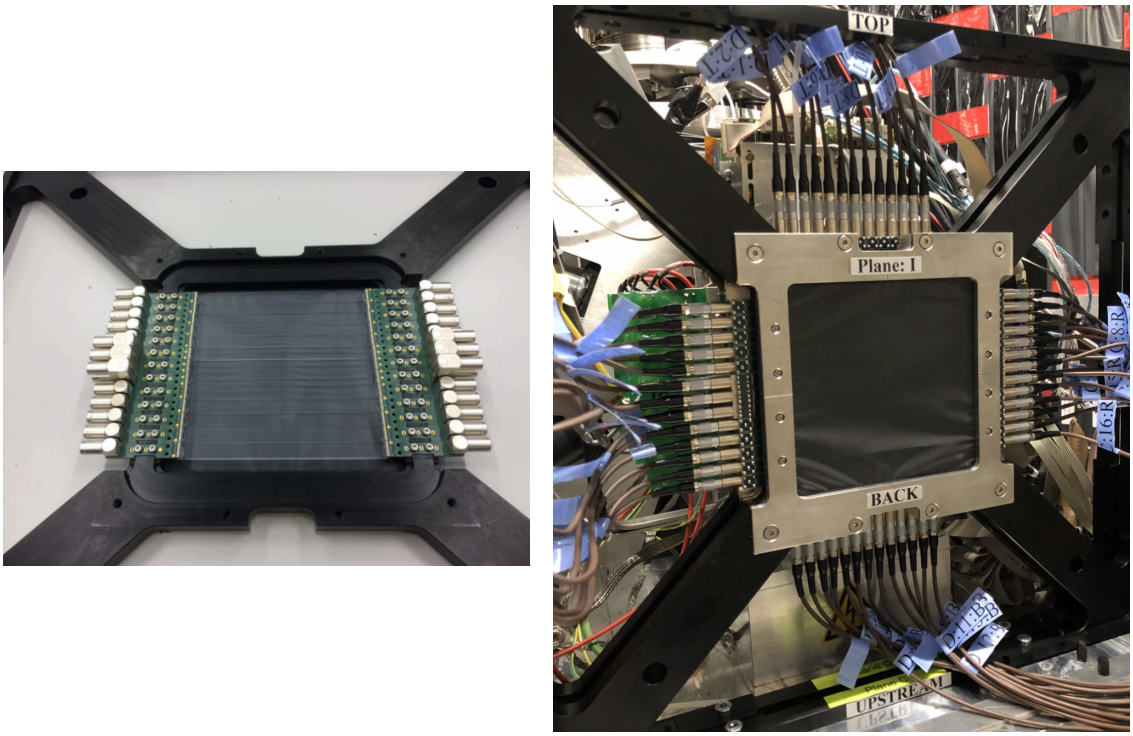

Figure 2.3 Left: One BH plane with thin scintillators and SiPM readout; Right: Two BH planes, one vertical with 13 paddles and one horizontal, with 16 paddles are mounted at PSI to take data [49].

The time resolution of one BH plane was determined with measurements with a centered and collimated ^{90}Sr source [49]. The results are shown in Figure 2.4, and are below the 100 ps requirement.

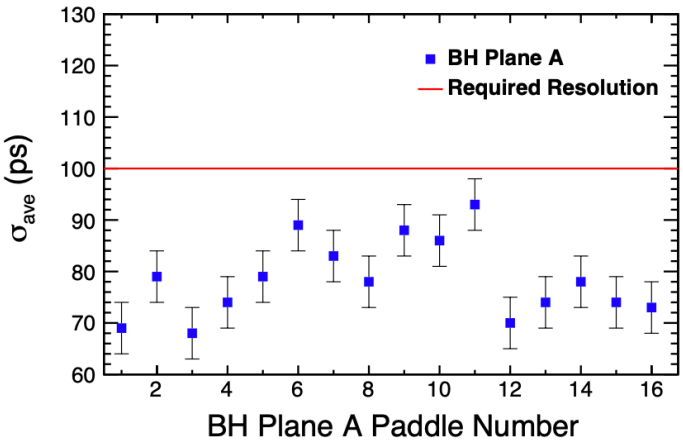

Figure 2.4 Average time resolution of one BH plane from measurements with a centered and collimated ^{90}Sr source [49].

2.2.2 Gas Electron Multiplier (GEM)

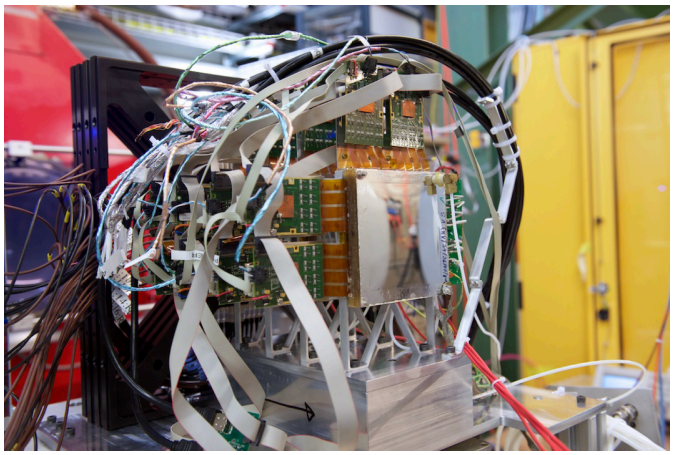

Figure 2.5 GEM detectors as incident-particle tracker at PSI.

Following the BH detector is the Gas Electron Multiplier (GEM) which is a high-resolution tracking detector. A GEM detector measures hit positions, and from the hit positions in multiple GEM detectors, one can infer particle trajectories into the target to reconstruct the scattering kinematics on an event-by-event basis. The GEM

detectors in MUSE have previously been used in the OLYMPUS experiment [51]. Each GEM's active area is 10 cm $\times$ 10 cm. A set of three GEM planes with electronics readout are shown in Fig. 2.5. The position resolution of the GEMs for beam-particle tracking was demonstrated to be 70 μm with the higher momentum and less multiple scattering at OLYMPUS, and this value meets the MUSE requirements.

2.2.3 Beamline Veto

In front of the target is a veto detector. The beam veto detector is used to reduce trigger rate, by vetoing scattering or beam particle decay events upstream of the scattering chamber. It consists of four scintillator segments with Hamamatsu R13435 PMT readout, see Fig. 2.6. The center of the veto is a 6 cm $\times$ 6 cm opening to allow the πM1 beam to pass through the target vacuum chamber's thin entrance window that has a radius of about 38 mm. The time resolution of the veto detector is required to be less than 1 ns per segment and the efficiency to be >99%. The performance of the veto detector satisfies this requirement.

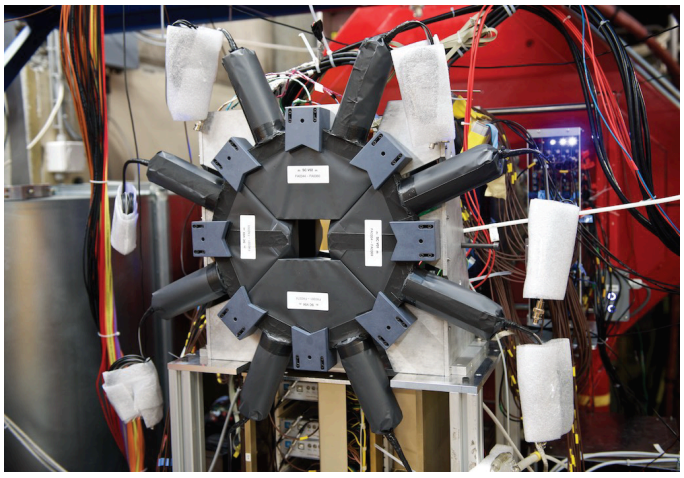

Figure 2.6 VETO detector at PSI.

2.2.4 Beamline Monitor (BM)

The Beam Monitor (BM) is installed in the beamline downstream of the MUSE target system. A picture of the BM is shown in Fig. 2.7. The BM is composed of a central scintillator hodoscope and four outer detectors. The central hodoscope of the BM comprises two planes of 16 paddles, each with 300 mm long $\times$ 12 mm wide $\times$ 3 mm thick BC-404 paddles. The outer four detectors are built of 30 cm long $\times$ 6 cm wide $\times$ 6 cm thick EJ-204 scintillators, read out at both ends with Hamamatsu R13435 PMTs. The time resolution is about 35 ps for the thick scintillators and near 100 ps for the thin paddles [49]. The BM provides a high-precision particle time measurement for beam-momentum determinations, and helps to suppress background. One background is Møller or Bhabha scattering, leading to a high-energy forward electron or positron in conjunction with a low energy scattered particle, which might trigger the detector system. This background can be reduced with a veto on forward-going particles with a signal in the BM.

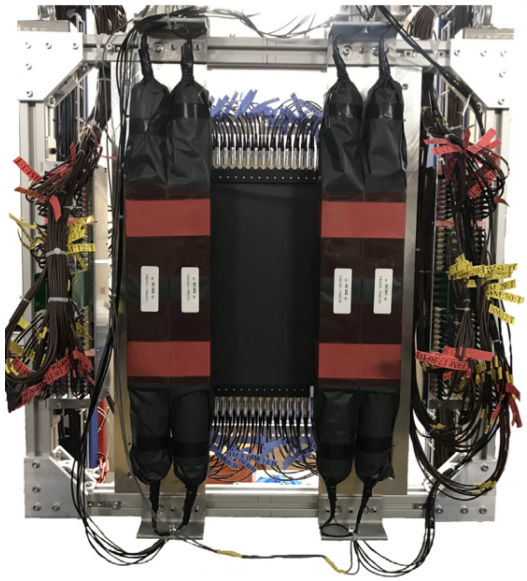

Figure 2.7 Beam Monitor at PSI with two fast scintillators at each side and a stack of two planes of 16 scintillator paddles in the center [49].

2.2.5 Photon Calorimeter

Downstream of the BM is the photon calorimeter. It consists of 8 × 8 lead-glass blocks, each with a dimension of 4 cm × 4 cm × 30 cm, as shown in Fig. 2.8. Each block is attached to a Hamamatsu R1355 PMT. The light output from each block is recorded separately. The calorimeter is used to veto photons radiated from the initial-state Bremsstrahlung effect, thus helping to control radiative corrections uncertainties for the elastic scattering in the MUSE experiment. In the MUSE experiment, $e^{\pm}$ and γ going forward lose energy in the form of electromagnetic cascades in the calorimeter and $e^{\pm}$ emit Cherenkov radiation in the lead-glass. The $\mu^{\pm}$ lose energy mainly by ionization which creates a smaller light output in the detector [52]. Incident charged particles can be identified upstream of the photon calorimeter by the BM detector. The original design of the calorimeter included 6 × 6 blocks without the four outer corners. The present 8 × 8 block design has a larger angular coverage of the initial-state Bremsstrahlung photons. The inclusion of a photon calorimeter, and the upgrade from 6 × 6 to 8 × 8 blocks were motivated by this work.

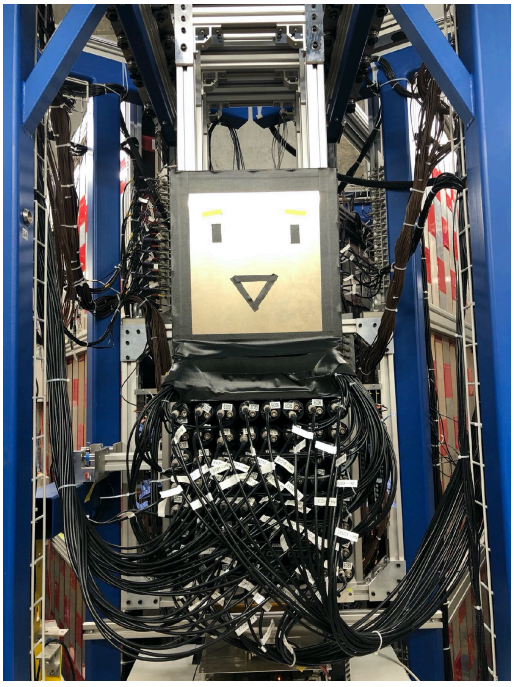

Figure 2.8 Photon calorimeter with 8 × 8 lead-glass blocks at PSI.

2.3 Target

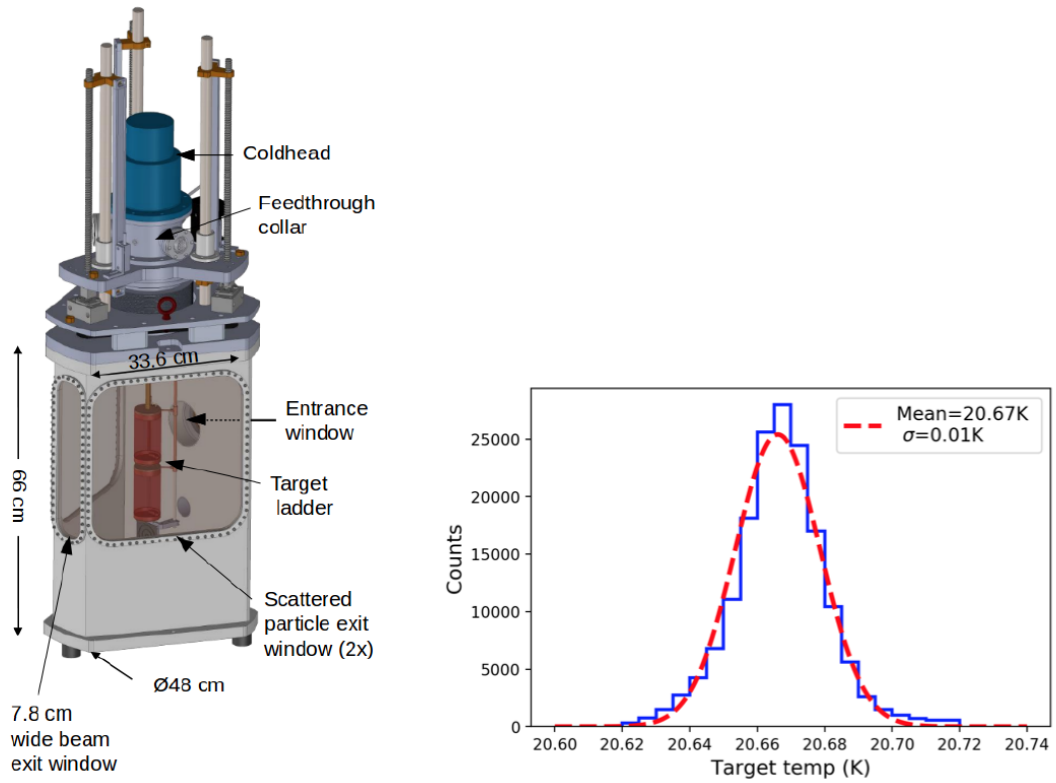

Figure 2.9 Left: A full view of the vacuum chamber with the lift system. Right: Liquid-hydrogen target temperature measured during a 72 hour period. The shape of the distribution is a Gaussian distribution with a mean of 20.67 K and a standard deviation of 0.01 K [53].

The MUSE experiment uses a liquid hydrogen target. Figure 2.9 left shows the MUSE target system. It consists of a target ladder with various targets, a cryocooler, and a copper condenser assembly that liquefies the hydrogen gas, a vacuum chamber that houses the target ladder and the condenser, a lifting system, a gas handling and vacuum system, and a slow control system to control hydrogen flow [53]. The target ladder includes a LH_2 cell for scattering, an empty cell for studying background generated from the target walls, and a 1 mm-thick solid solid targets for precision vertex reconstruction and detector alignment. The two vacuum exit windows on each side of the beamline oriented at 65° cover the azimuth range [20°, 100°] and

polar-angle range $[-45°, 45°]$ from the target center.

To control systematic uncertainties at the sub-percent level, it requires a very stable density, and a sufficient cooling power in the target length. The hydrogen cool down performance is shown in Fig. 2.9 right. The target cell operating temperature was 20.67 K and constant at the 0.01 K level over the entire period. More details about the structure and performance of the target can be found in [53].

2.4 Scattered Particle Spectrometer

2.4.1 Straw Tube Tracker (STT)

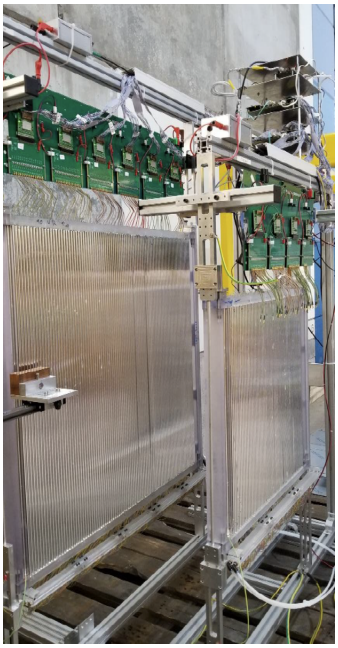

Figure 2.10 Straw Tube Tracker at PSI. Two chambers with 5 vertical and 5 horizontal planes each based on PANDA design [54].

The Straw Tube Tracker locates on the left and right side of the beam symmetrically. It's design is based on work of the PANDA collaboration [54]. It provides high resolution and high efficiency tracking of the scattered particles from the target. On each side there are chambers (front 60 cm and rear 90 cm long straw tubes), each chamber with 5 vertical planes and 5 horizontal planes. Figure 2.10 shows the front

STT chamber and back STT chamber on one side for testing. The chamber position resolution is expected to be less than 120 μm which is below the requirement.

2.4.2 Scattered Particle Scintillator (SPS)

The scattered-particle scintillators (SPS) provide event trigger and particle separation through time-of-flight. The SPS detectors were built and tested by the Experimental Nuclear Physics Group at USC. The design and construction procedures of the MUSE detectors follow that of the FToF12 for CLAS12 at Jefferson Lab [55]. Each counter consists of a plastic scintillator bar (Eljen EJ-204) with Photomultiplier tubes (PMT, Hamamatsu R13435) glued on each end. The bar is wrapped first with precision-cut aluminized mylar foil, then with Tedlar. The Tedlar film extends beyond each PMT onto the anode, dynode, and high-voltage cables, to provide a light-tight casing for the entire counter. Pairs of scintillator bars are mounted on a backing structure. The backing structure for the front wall is a ROHACELL board sandwiched between two carbon-fiber sheets and aluminum sheets for the rear wall. These units are mounted in a frame in PSI.

Figure 2.11 SPS front and rear walls in test stand at PSI.

There are two walls on each side. Figure 2.11 shows the front and rear wall on one side mounted in a test stand at PSI. Each front wall consists of 18 bars, each bar is 6 cm × 3 cm × 120 cm, and each rear wall consists of 28 bars with each bar 6 cm × 6 cm × 220 cm. Table 2.1 shows the design parameters for the front and back scintillator walls. The front wall is approximately square and covers at least a horizontal angular range from 20° to 100° from the target, and azimuth −45° to 45° from the target center at 60°. The back wall has an increased angular acceptance to account for particles which scatter in the front wall material.

Table 2.1 Design parameters for the scintillator walls.

	Front wall	Back wall
Number of scintillator bars	18	28
Scintillator cross section	6 cm × 3 cm	6 cm × 6 cm
Scintillator length	120 cm	220 cm
Target to front-face distance	57 cm	79 cm
Scintillator material	EJ-204	EJ-204
Photomultiplier	Hamamatsu R13435	Hamamatsu R13435

Using the six-bar cosmic-ray method, which is discussed in detail in Appendix A, the time resolution of the short front bars are better than 50 ps, and better than 60 ps for the long rear bars, as shown in Fig. 2.12. The SPS detectors are energy calibrated close to the detection threshold with ^{22}Na, ^{88}Y, and ^{208}Ti gamma sources to precisely determine that threshold. Detailed work on this part is available in [56].

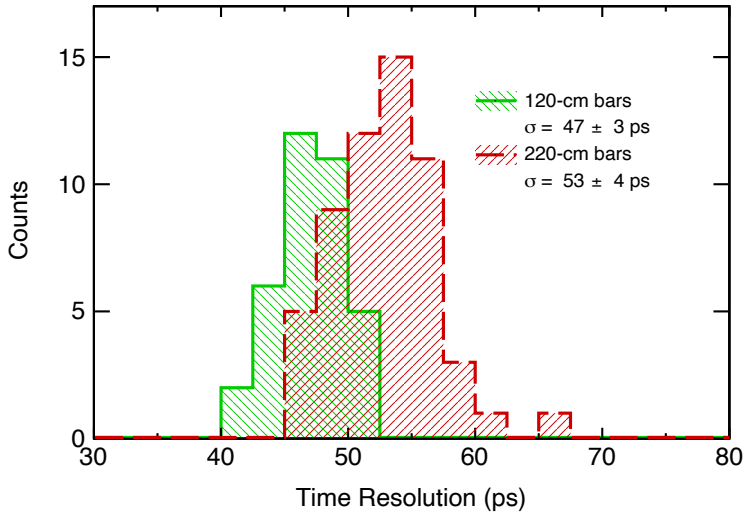

Figure 2.12 Results of time-resolution measurements at USC for the SPS front-wall (solid) and rear-wall (dashed) detectors.

Chapter 3

Radiative Corrections

3.1 General Theory of Elastic Lepton-Proton Scattering

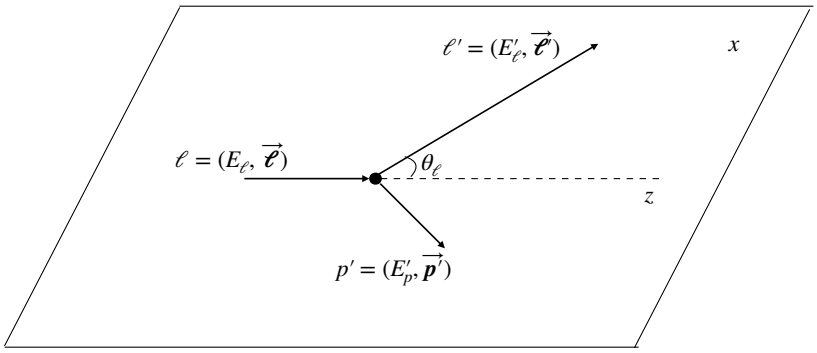

Figure 3.1 Kinematic diagram for elastic lepton-proton scattering in the lab frame.

The kinematics of the elastic scattering of a lepton off a target at rest is shown in Fig. 3.1. An incident lepton ℓ (with mass m and energy E_ℓ) scatters on a stationary proton p (with mass M). Quantum electrodynamics (QED) describes the interaction using the exchange of a virtual photon. The coordinate system is chosen such that the z-axis is directed along the momentum direction of the incident lepton, and the x-z plane is defined by the momenta of the incident and scattered leptons. The kinematics of the final state is constrained by the direction of the outgoing lepton (polar angle θ_ℓ, azimuth $\phi_\ell = 0$). The four-momenta of the particles can be expressed in the lab frame as

$$\ell = (E_\ell, 0, 0, |\vec{\boldsymbol{\ell}}|),$$
$$p = (M, 0, 0, 0),$$
$$\ell' = (E'_\ell, |\vec{\boldsymbol{\ell}}'| \sin\theta_\ell, 0, |\vec{\boldsymbol{\ell}}'| \cos\theta_\ell), \text{ and}$$
$$p' = \ell + p - \ell'. \tag{3.1}$$

The final energy of the lepton E'_ℓ can be calculated for elastic scattering from the beam energy and scattering angle as [43]

$$E'_\ell = \frac{(E_\ell + M)(ME_\ell + m^2) + \sqrt{M^2 - m^2 \sin^2\theta_\ell}|\vec{\boldsymbol{\ell}}|^2 \cos\theta_\ell}{(E_\ell + M)^2 - |\vec{\boldsymbol{\ell}}|^2 \cos^2\theta_\ell}. \tag{3.2}$$

The four-momentum transfer, $q = \ell - \ell'$, is in one-photon exchange equal to the four-momentum of the virtual photon. The invariant mass of the photon q^2 is always negative in lepton scattering (space-like by definition). It is common to use the positive quantity $Q^2 = -q^2$ to describe form factors and structure functions. In elastic scattering,

$$Q^2 = -q^2 = 2(E_\ell E'_\ell - \vec{\boldsymbol{\ell}} \cdot \vec{\boldsymbol{\ell}}') - 2m^2 = 2M(E_\ell - E'_\ell). \tag{3.3}$$

In QED, the Feynman diagram at leading order (Born term) of lepton-proton scattering is illustrated in Fig. 3.2, where a single photon is exchanged in the interaction. The lepton-photon vertex is represented by γ^μ and the proton vertex by Γ^μ which encodes the proton structure. The amplitude corresponding to the one-photon exchange Feynman diagram can be written as the product of the leptonic and hadronic current, ℓ_μ and J^μ [57],

$$-i\mathcal{M}_{\text{Born}} = \frac{-ig_{\mu\nu}}{q^2}[ie\bar{u}(\ell')\gamma^\mu u(\ell)][ie\bar{u}(p')\Gamma_\mu u(p)] = \frac{i}{q^2}\ell_\mu J^\mu, \tag{3.4}$$

where γ^μ are the Dirac 4×4 matrices,

$$\gamma_0 = \begin{pmatrix} 1 & 0 \\ 0 & -1 \end{pmatrix}, \vec{\gamma} = \begin{pmatrix} 0 & \vec{\sigma} \\ -\vec{\sigma} & 0 \end{pmatrix}, \tag{3.5}$$

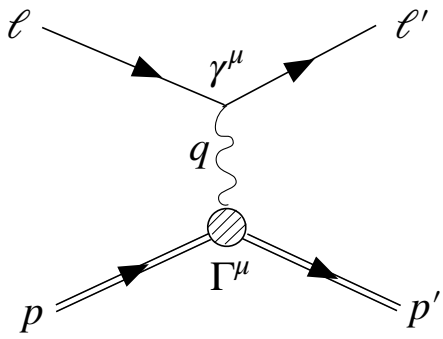

Figure 3.2 The one-photon exchange (Born term) Feynman diagram for elastic lepton-proton scattering.

where $\vec{\sigma}$ is a three-vector with the standard Pauli matrices, and $u(\ell)$ and $u(p)$ are the lepton and proton Dirac spinors. The proton Dirac spinor has the form

$$u(p) = \sqrt{E_p + M} \begin{pmatrix} \chi \\ \frac{\vec{\sigma}\cdot\vec{p}}{E_p+M}\chi \end{pmatrix}, \tag{3.6}$$

where χ is a two-component spinor and E_p the energy of the proton. The relativistic invariant normalization for the Dirac spinor is $u^\dagger u = 2E_p$. The quantity Γ^μ contains the information about the electromagnetic structure of the proton. As the proton is a composite object, J^μ is generally written in terms of Dirac and Pauli form factors $F_1(Q^2)$ and $F_2(Q^2)$ [57],

$$J^\mu = e\bar{u}(p') \left[F_1(Q^2)\gamma^\mu + \frac{\kappa}{2M} F_2(Q^2) i\sigma^{\mu\nu} q_\nu \right] u(p), \tag{3.7}$$

with $\sigma^{\mu\nu} = \frac{i}{2}[\gamma^\mu, \gamma^\nu]$, and κ is the anomalous magnetic moment of the proton.

Usually, it is more useful to introduce the so-called Sachs electric and magnetic

form factors [58],

$$G_E(Q^2) \equiv F_1(Q^2) + \frac{\kappa q^2}{4M^2} F_2(Q^2),$$
$$G_M(Q^2) \equiv F_1(Q^2) + \kappa F_2(Q^2). \tag{3.8}$$

The form factors specify how the complex charge and current distributions of the proton respond to an electromagnetic field. To understand this, one may consider the Breit frame since the proton is not static but has a recoil effect in the elastic scattering process. In the Breit frame, the initial and final states of the proton have momenta with the same magnitude but opposite directions, and there is no energy transferred to the proton. It has been proven that the time component of current J^μ is simplified in the Breit frame as [57]

$$J^0 = e2M\chi'^{\dagger}\chi(F_1 - \tau\kappa F_2) = e2M\chi'^{\dagger}\chi G_E(Q^2), \tag{3.9}$$

and the vector component of current J^μ can also be expressed as

$$\vec{J} = e\chi'^{\dagger}(\vec{\sigma} \times \vec{q_B})\chi(F_1 + \kappa F_2) = e\chi'^{\dagger}(\vec{\sigma} \times \vec{q_B})\chi G_M(Q^2). \tag{3.10}$$

In the Breit frame, the electric form factor $G_E(Q^2)$ is directly related to J^0, which describes the interaction of the nucleon electric charge in the Coulomb potential. The magnetic form factor $G_M(Q^2)$ is related to $\vec{J}$, which describes the interaction of the nucleon spin with the magnetic field. The form factors are interpreted as the Fourier transformation of the charge distribution and the magnetic moment distribution of protons respectively in this frame under the non-relativistic limit,

$$G_E(Q^2) = \int e^{i\vec{q}\cdot\vec{r}/\hbar}\rho(\vec{r})\mathrm{d}^3 r, \tag{3.11}$$

where $\rho(\vec{r})$ is the nonrelativistic (NR) charge density within a proton as a function of the radius vector from the center of the proton. A Taylor expansion of $G_E(Q^2)$ at

small Q^2 gives

$$\begin{aligned} G_E(Q^2) &= \int \left(1 + i\vec{q}\cdot\vec{r}/\hbar - \frac{(\vec{q}\cdot\vec{r}/\hbar)^2}{2} + \ldots\right)\rho(\vec{r})\mathrm{d}^3r \\ &= 1 - \frac{1}{6\hbar^2}q^2\int r^2\rho(\vec{r})\mathrm{d}^3r + \ldots \\ &= 1 - \frac{1}{6\hbar^2}Q^2\langle r^2\rangle + \ldots. \end{aligned} \tag{3.12}$$

The well-known mean square proton charge radius is

$$\langle r^2\rangle = -6\hbar^2\left.\frac{\mathrm{d}G_E(Q^2)}{\mathrm{d}Q^2}\right|_{Q^2=0}. \tag{3.13}$$

In Ref. [9], Miller points out that the relation between the form factors and the three-dimensional charge density is not correct. A two-dimensional charge density, which describes the matrix element of the density operator between identical initial and final states, is defined in the infinite-momentum-frame (IMF). This two-dimensional charge density is determined by the Dirac form factor F_1. Although there is a difference between the IMF value and the non-relativistic value on the proton radius, it is clarified that $-6\hbar^2\left.\frac{\mathrm{d}G_E(Q^2)}{\mathrm{d}Q^2}\right|_{Q^2=0}$ is the quantity the hydrogen spectroscopy measurements determine and is related to the proton charge radius. Therefore, in elastic scattering experiments and hydrogen spectroscopy experiments, the same quantity is measured, and Eq. (3.13) is used as the *definition* of the proton's charge radius.

The differential cross section in elastic scattering reads [57]

$$\mathrm{d}\sigma_{\mathrm{Born}} = \frac{1}{4\sqrt{(\ell\cdot p)^2 - m^2M^2}}\frac{|\mathcal{M}_{\mathrm{Born}}|^2}{4\pi^2}\frac{\mathrm{d}^3\vec{\boldsymbol{\ell}'}}{2E'_\ell}\frac{\mathrm{d}^3\vec{\boldsymbol{p}'}}{2E'_p}\delta^{(4)}(\ell + p - \ell' - p'). \tag{3.14}$$

This matrix element squared is written as [57],

$$|\mathcal{M}_{\mathrm{Born}}|^2 = \frac{e^4}{q^4}L^{\mu\nu}W_{\mu\nu}. \tag{3.15}$$

The product of the tensors $L^{\mu\nu}$ and $W_{\mu\nu}$ is a relativistic invariant and can be calculated in any reference system. For unpolarized scattering, the lepton tensor $L^{\mu\nu}$ is averaged over the initial spin states, and summed over the final spin states [57],

$$L^{\mu\nu} = 2(\ell'^\mu\ell^\nu + \ell'^\nu\ell^\mu - (\ell'\cdot\ell - m^2)g^{\mu\nu}). \tag{3.16}$$

The hadron tensor $W_{\mu\nu}$ is more complicated. For unpolarized initial and final protons, it is related to the form factors. The differential cross section for the scattering of massive leptons from proton is [59]

$$\frac{\mathrm{d}\sigma_{\mathrm{Born}}}{\mathrm{d}\Omega} = \left[\frac{\mathrm{d}\sigma}{\mathrm{d}\Omega}\right]_{ns} \left[\frac{G_E^2(Q^2) + \tau G_M^2(Q^2)}{1+\tau} + \left(2\tau - \frac{m^2}{M^2}\right) G_M^2(Q^2) \frac{\eta}{1-\eta}\right], \tag{3.17}$$

where

$$\left[\frac{\mathrm{d}\sigma}{\mathrm{d}\Omega}\right]_{ns} = \frac{\alpha^2}{4E_\ell^2} \frac{1-\eta}{\eta^2} \frac{1/d}{[1 + \frac{2E_\ell d}{M}\sin^2\frac{\theta_\ell}{2} + \frac{E_\ell}{M}(1-d)]} \tag{3.18}$$

is the no-structure cross section, with $\tau = \frac{Q^2}{4M^2}$, $\eta = Q^2/4EE'_\ell$, and $d = \frac{[1-\frac{m^2}{E_\ell^2}]^{1/2}}{[1-\frac{m^2}{E_\ell'^2}]^{1/2}}$. With $m = 0$, it follows that $d = 1$, $\eta = \sin^2\frac{\theta_\ell}{2}$, and Eq. (3.17) turns into the well-known Rosenbluth formula in the so-called extreme relativistic limit (ERL).

3.2 Radiative Corrections to Elastic Lepton-Proton Scattering

Considering the first-order QED radiative corrections, including the virtual (Fig. 3.3) and bremsstrahlung (inelastic) contributions (Fig. 3.4), the squared amplitude, which is related to the cross section for elastic and inelastic scattering can be written as [43]

$$|\mathcal{M}_{\mathrm{elast}}|^2 = |\mathcal{M}_{\mathrm{Born}}|^2 + 2\sum_i \mathrm{Re}(\mathcal{M}^\dagger_{\mathrm{Born}}\mathcal{M}_i), \tag{3.19}$$

where the summation is over the matrix elements $\mathcal{M}_{\mathrm{vac}}$, $\mathcal{M}^\ell_{\mathrm{vert}}$, $\mathcal{M}^p_{\mathrm{vert}}$, $\mathcal{M}_{\mathrm{box}}$, and $\mathcal{M}_{\mathrm{xbox}}$ in Eq. (3.19).

As mentioned in Chapter 1, many calculations of radiative corrections use the soft-photon and ultrarelativistic approximations. To separate the regions of the validity of these approximations, a cut-off energy of bremsstrahlung photons E_γ^{cut} is introduced. When the photon energy is below E_γ^{cut}, the analytical integration of the cross section is simplified. The matrix elements above contain infrared-divergent (IR) terms except for $\mathcal{M}_{\mathrm{Born}}$ and $\mathcal{M}_{\mathrm{vac}}$. The infrared divergent terms are canceled in the

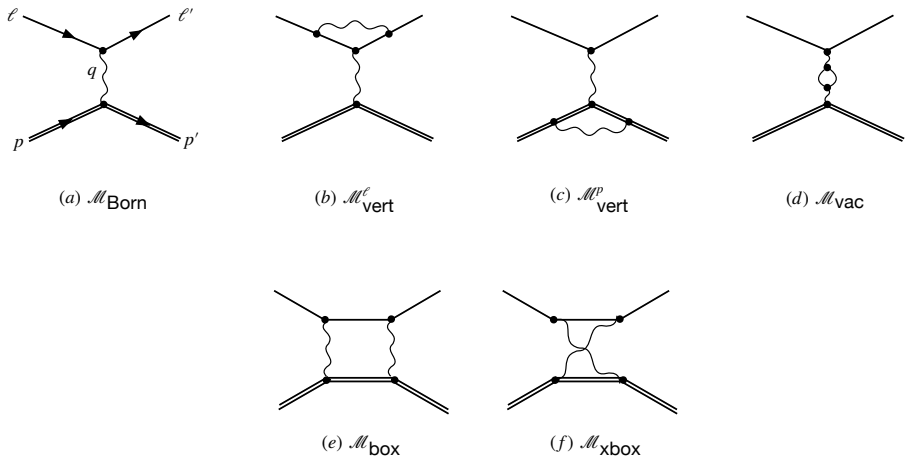

Figure 3.3 The Feynman diagrams representing the elastic scattering of charged leptons on protons in the leading order (a), and the virtual photon contributions to order α^2 (b) – (f), including vertex corrections, the vacuum polarization correction, and the TPE corrections.

summation. Following the formalism of Ref. [43], all the virtual photon amplitudes can be expressed through the Born term under the approximations mentioned above,

$$\mathcal{M}^{e}_{\text{vac}} = \frac{\alpha}{3\pi}\left[-\frac{5}{3} + \ln\frac{-q^2}{m^2}\right]\mathcal{M}_{\text{Born}}, \tag{3.20}$$

$$\mathcal{M}^{\ell}_{\text{vert}} = -\frac{\alpha}{2\pi}\left[K(\ell,\ell') - K(\ell,\ell) - \frac{3}{2}\ln\frac{-q^2}{m^2} + 2\right]\mathcal{M}_{\text{Born}}, \tag{3.21}$$

$$\mathcal{M}^{p}_{\text{vert}} = -\frac{\alpha}{2\pi}\left[K(p,p') - K(p,p)\right]\mathcal{M}_{\text{Born}}, \tag{3.22}$$

$$\mathcal{M}^{\text{MTs}}_{\text{box}} = z\frac{\alpha}{2\pi}\left[K(\ell,-p) - K(\ell',-p')\right]\mathcal{M}_{\text{Born}}, \tag{3.23}$$

$$\mathcal{M}^{\text{MTs}}_{\text{xbox}} = -z\frac{\alpha}{2\pi}\left[K(\ell',p) - K(\ell,p')\right]\mathcal{M}_{\text{Born}}, \tag{3.24}$$

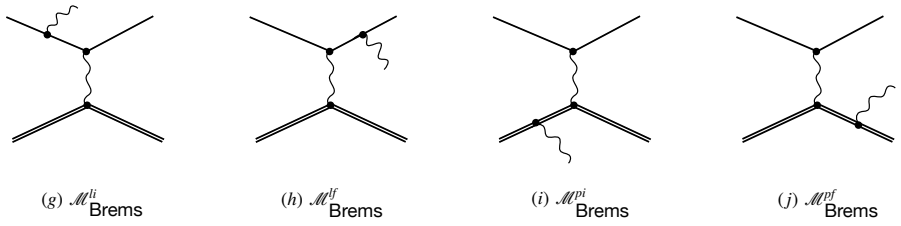

Figure 3.4 The Feynman diagrams representing the first-order bremsstrahlung processes. The photon is emitted from the initial-state lepton (g), final-state lepton (h), initial-state proton (i), or final-state proton (j).

where the infrared divergent term $K(p_i, p_j)$ is included,

$$K(p_i, p_j) = (p_i \cdot p_j) \int_0^1 \frac{\mathrm{d}x}{p_x^2} \ln \frac{p_x^2}{\lambda^2}. \tag{3.25}$$

Here λ is the fictitious photon mass and it is the standard method of regularization of the infrared divergences, and the four-momentum p_x is defined as $p_x = xp_i + (1-x)p_j$. In particular,

$$K(p_i, p_i) = \ln \frac{m_i^2}{\lambda^2}. \tag{3.26}$$

The differential cross section of internal bremsstrahlung with soft photon emission is expressed as [43]

$$\left.\frac{\mathrm{d}\sigma_{\mathrm{brems}}}{\mathrm{d}\Omega_\ell}\right|_{E_\gamma<E_\gamma^{\mathrm{cut}}} = -2\alpha\Big[\tilde{B}(\ell,\ell,E_\gamma^{\mathrm{cut}})-2\tilde{B}(\ell,\ell',E_\gamma^{\mathrm{cut}})+\tilde{B}(\ell',\ell',E_\gamma^{\mathrm{cut}})+2z\tilde{B}(\ell,p,E_\gamma^{\mathrm{cut}})$$
$$-2z\tilde{B}(\ell,p',E_\gamma^{\mathrm{cut}})-2z\tilde{B}(\ell',p,E_\gamma^{\mathrm{cut}})+2z\tilde{B}(\ell',p',E_\gamma^{\mathrm{cut}})+\tilde{B}(p,p,E_\gamma^{\mathrm{cut}})-2\tilde{B}(p,p',E_\gamma^{\mathrm{cut}})$$
$$+\tilde{B}(p',p',E_\gamma^{\mathrm{cut}})+\frac{1}{2\pi}\ln\frac{m^2}{\lambda^2}+\frac{1}{2\pi}\ln\frac{M^2}{\lambda^2}-\frac{1}{2\pi}K(\ell,\ell')+\frac{z}{2\pi}K(\ell,p)$$
$$-\frac{z}{2\pi}K(\ell,p')-\frac{z}{2\pi}K(\ell',p)+\frac{z}{2\pi}K(\ell',p')-\frac{1}{2\pi}K(p,p')\Big]\frac{\mathrm{d}\sigma_{\mathrm{Born}}}{\mathrm{d}\Omega_\ell}, \quad (3.27)$$

here, z is the sign of the charged leptons, and the value of $\tilde{B}(p_i,p_j,E_\gamma^{\mathrm{cut}})$ is finite. Combining the virtual photon amplitudes into Eq. (3.19), it can be seen that the TPE term and the bremsstrahlung term in Eq. (3.27) depend on the sign of the lepton charge while other terms do not. So they are relevant in negatively and positively charged lepton comparisons.

The analytical expression of the total cross section for emitting a photon with energy less than E_γ^{cut} is obtained by adding all these terms and the summation is finite. Therefore the Born matrix element can be factored out, leaving the final radiative correction result with a factor δ [43],

$$\frac{\mathrm{d}\sigma_{\mathrm{elast}}}{\mathrm{d}\Omega_\ell}+\left.\frac{\mathrm{d}\sigma_{\mathrm{brems}}}{\mathrm{d}\Omega_\ell}\right|_{E_\gamma<E_\gamma^{\mathrm{cut}}} = (1+\delta)\frac{\mathrm{d}\sigma_{\mathrm{Born}}}{\mathrm{d}\Omega_\ell}, \quad (3.28)$$

$$\begin{aligned}\delta = {}& \frac{2\alpha}{3\pi}[-\frac{5}{3}+\ln\frac{-q^2}{m^2}]+\frac{\alpha}{\pi}[\frac{3}{2}+\ln\frac{-q^2}{m^2}-2]\\ & -2\alpha\Big[\tilde{B}(\ell,\ell,E_\gamma^{\mathrm{cut}})-2\tilde{B}(\ell,\ell',E_\gamma^{\mathrm{cut}})+\tilde{B}(\ell',\ell',E_\gamma^{\mathrm{cut}})\Big]\\ & -2\alpha\Big[\tilde{B}(p,p,E_\gamma^{\mathrm{cut}})-2\tilde{B}(p,p',E_\gamma^{\mathrm{cut}})+\tilde{B}(p',p',E_\gamma^{\mathrm{cut}})\Big]\\ & -4z\alpha\Big[\tilde{B}(\ell,p,E_\gamma^{\mathrm{cut}})-\tilde{B}(\ell,p',E_\gamma^{\mathrm{cut}})-\tilde{B}(\ell'p,E_\gamma^{\mathrm{cut}})+\tilde{B}(\ell',p',E_\gamma^{\mathrm{cut}})\Big].\end{aligned} \quad (3.29)$$

3.3 ESEPP Event Generator

The Elastic Scattering of Electrons and Positrons on Protons (ESEPP) event generator [43] takes into account the first-order radiative corrections of elastic scattering of

charged leptons ($e^{\pm}$ and $\mu^{\pm}$) off protons. One advantage of ESEPP is that it includes the exact bremsstrahlung calculation without the soft-photon approximation. The differential cross section of the bremsstrahlung process when the photon energy is above $E_{\gamma}^{\rm cut}$ is expressed as

$$\frac{\mathrm{d}\sigma_{\rm brems}}{\mathrm{d}E_{\gamma}d\Omega_{\gamma}d\Omega_{\ell}} = \frac{1}{(4\pi)^5}\frac{1}{M|\vec{\boldsymbol{\ell}}|}\sum_{E'_{\ell}}\frac{E_{\gamma}|\vec{\boldsymbol{\ell}}'|^2|\mathcal{M}_{\rm brems}|^2}{|AE'_{\ell}-B|\vec{\boldsymbol{\ell}}'||}, \tag{3.30}$$

where the squared amplitude $|\mathcal{M}_{\rm brems}|^2$ is

$$|\mathcal{M}_{\rm brems}|^2 = |\mathcal{M}^{\ell}_{\rm brems}|^2 + |\mathcal{M}^{p}_{\rm brems}|^2 + 2{\rm Re}(\mathcal{M}^{\ell\dagger}_{\rm brems}\mathcal{M}^{p}_{\rm brems}). \tag{3.31}$$

Another advantage of ESEPP is that it implements an accurate calculation of the event kinematics for both electrons and muons. Considering the kinematics of the process $\ell^{\pm}p \to \ell^{\pm}p\gamma$, the conservation of the four-momentum gives

$$\ell + p = \ell' + p' + k, \tag{3.32}$$

where k is the four-momentum of the radiated photon. In the frame of Fig. 3.1, the four-momentum of the scattered proton and the real photon can be written in terms of proton angles (θ_p, φ_p) and photon angles (θ_{γ}, φ_{γ}),

$$p' = (E_p, \vec{\boldsymbol{p}'}) = (E_p, |\vec{\boldsymbol{p}'}|\sin\theta_p\cos\varphi_p, |\vec{\boldsymbol{p}'}|\sin\theta_p\sin\varphi_p, |\vec{\boldsymbol{p}'}|\cos\theta_p), \tag{3.33}$$

$$k = (E_{\gamma}, \vec{\boldsymbol{k}}) = (E_{\gamma}, E_{\gamma}\sin\theta_{\gamma}\cos\varphi_{\gamma}, E_{\gamma}\sin\theta_{\gamma}\sin\varphi_{\gamma}, E_{\gamma}\cos\theta_{\gamma}). \tag{3.34}$$

The scattered lepton's erengy is

$$E'_{\ell} = \frac{BC \pm A\sqrt{m^2(A^2-B^2)+C^2}}{A^2-B^2}, \tag{3.35}$$

where the coefficients A, B, and C are

$$\begin{aligned} A &= |\vec{\boldsymbol{\ell}}|\cos\theta_{\ell} - E_{\gamma}\cos\psi, \\ \cos\psi &= \cos\theta_{\ell}\cos\theta_{\gamma} + \sin\theta_{\ell}\sin\theta_{\gamma}\cos\varphi_{\gamma}, \\ B &= E_{\ell} + M - E_{\gamma}, \\ C &= E_{\gamma}(E_{\ell} + M - |\vec{\boldsymbol{\ell}}|\cos\theta_{\gamma}) - ME_{\ell} - m^2. \end{aligned} \tag{3.36}$$

Based on the theory mentioned above, ESEPP is written in the C++ programming language using some ROOT classes. As an unweighted event generator, ESEPP randomly generates events of two types: elastic ($\ell^{\pm}p \to \ell^{\pm}p$) and inelastic ($\ell^{\pm}p \to \ell^{\pm}p\gamma$). The first-order bremsstrahlung is taken into account in both cases, and the separation between these two types of events is based on the energy of the emitted photon. If this energy does not exceed the cut off value E_{γ}^{cut}, then the scattering process can be considered elastic. In this case, the analytical expression of the cross section can be used, and there is only one kinematic variable - the lepton scattering angle θ_{ℓ}. Inelastic events can be generated using the accurate bremsstrahlung cross section and there are four basic kinematic variables: the lepton scattering angle θ_{ℓ}, the energy of real photon E_{γ}, the polar and azimuthal angle of real photon θ_{γ}, φ_{γ}. Table 3.1 gives one example of the input parameters of ESEPP for electrons in MUSE kinematics with a beam momentum of 161 MeV/c, and scattering-angle range 55° to 65°.

Table 3.1 Example of the input parameters of ESEPP in MUSE Kinematic.

Type of scattering events to generate	e^{-}
Proton form factors	Kelly
First-order bremsstrahlung model	accurate QED calculation
Vacuum polarization	full vacuum polarization correction
TPE model	Mo and Tsai
Full energy of incident leptons	161 MeV
Energy of bremsstrahlung photon	1-160 MeV
Polar angle of scattered leptons θ	$55^{\circ} - 65^{\circ}$
Azimuthal angle of scattered leptons ϕ	$(-180^{\circ}) - (+180^{\circ})$

3.4 $\ell^{\pm}p \to \ell'^{\pm}p'\gamma$ Distribution in MUSE Kinematics

3.4.1 Lepton Distribution

The differential cross sections as a function of the scattered lepton energy with the elastic peak and the radiative tail using the ESEPP event generator are shown in

Figs. 3.5 and 3.6, respectively. The beam momenta for the plots are 115 MeV/c (top), 161 MeV/c (middle) and 210 MeV/c (bottom). For each momentum, the scattering-angle ranges are 20°-30°, 55°-65°, and 90°-100°. To get the differential cross section, the number of the electrons at each scattering momentum bin are normalized with the corresponding integrated luminosity. As an unweighted event generator, events are generated following the differential cross section. The cross sections are higher at smaller scattering angles. The maximum on the high momentum side of each histogram is the elastic peak. In the histogram for 115 MeV/c beam momentum, there are dips close to the elastic peak. The dips are caused by the $E_{\gamma}^{\mathrm{cut}}$ value (1 MeV in this case) which separates the elastic and inelastic events. The dips are in 161 MeV/c and 210 MeV/c plots as well. They are invisible because the width of the gap is smaller than the width of the bin on the x-axis. Towards lower momenta, for the electron tail, the differential cross section falls down first and starts rising. This rising phenomenon is because of initial-state radiation. In the initial-state bremsstrahlung effect, the bremsstrahlung photon is emitted from the initial lepton leg and in the incoming lepton direction. The photons which carry energy away from the lepton will reduce the beam energy, and then increase the cross section. The radiative tail for muons drops over more orders of magnitude than that for electrons. At vanishing final lepton momenta, the differential cross sections tend to zero for both the electron and muon cases. However, for electrons, the cross section reaches a local maximum before going down to zero. This phenomenon is explained in Ref. [60] as the result of the non-zero lepton mass coupled with the small q^2 behavior at small p' values. The fluctuations at low momenta in the muon histograms of Fig. 3.6 are caused by poor sampling statistics, especially at forward angles.

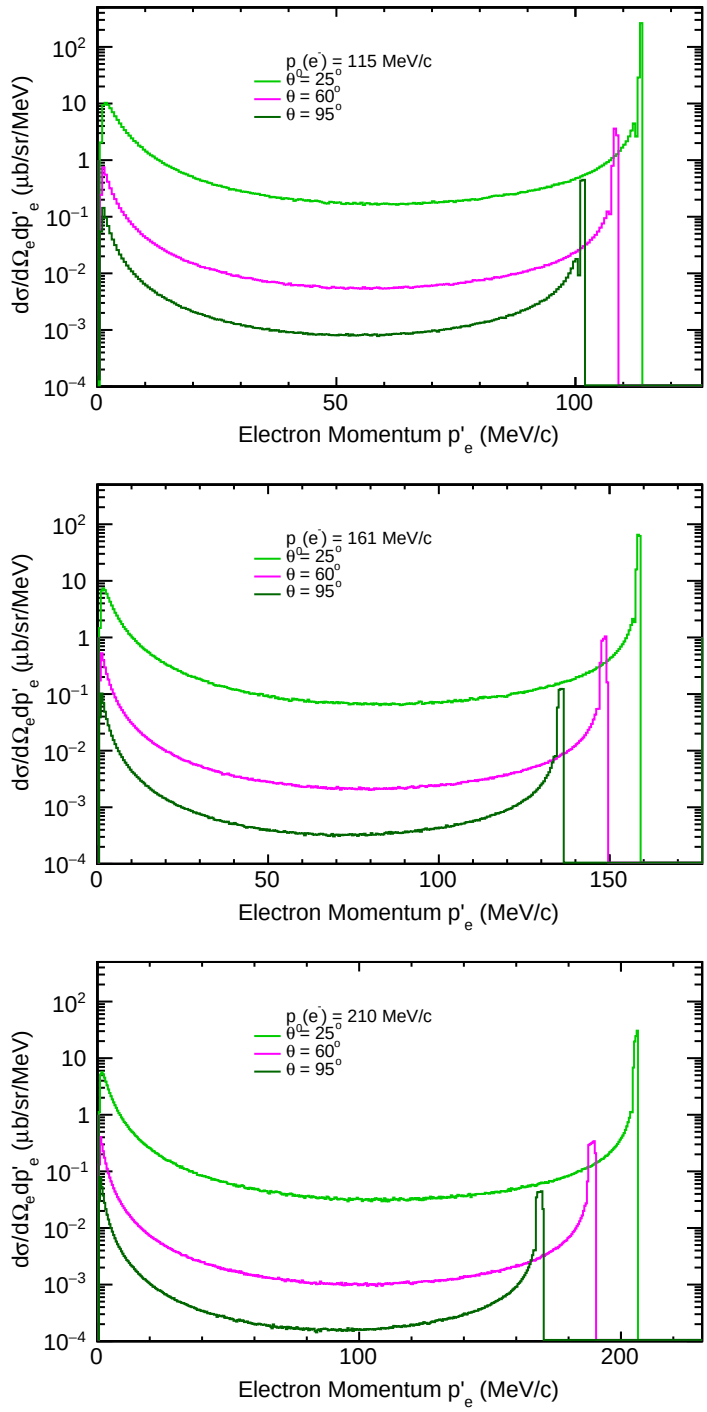

Figure 3.5 The *ep* cross section with elastic peak and radiative tail from the ESEPP event generator for three different scattering angles 25° (light green), 60° (magenta) and 95° (dark green) and electron beam energies of 115 MeV/c (top panel), 161 MeV/c (middle panel) and 210 MeV/c (bottom panel).

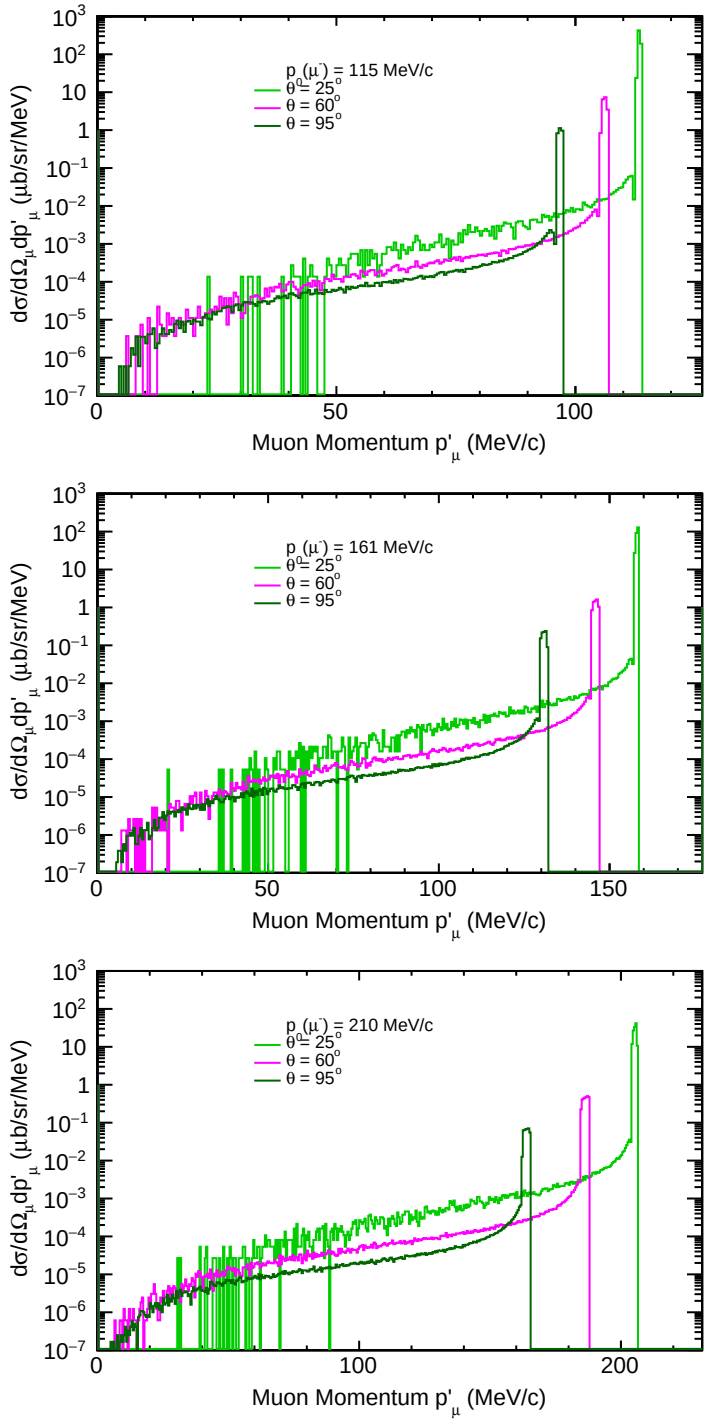

Figure 3.6 The μp cross section with elastic peak and radiative tail from the ESEPP event generator for three different scattering angles 25° (light green), 60° (magenta) and 95° (dark green) and muon beam energies of 115 MeV/c (top panel), 161 MeV/c (middle panel) and 210 MeV/c (bottom panel).

3.4.2 Photon Distribution

One example of a photon distribution from the ESEPP event generator is shown in Fig. 3.7, which illustrates the photon polar angle versus photon energy distribution at 161 MeV/c lepton beam momentum and 60° scattering angle. The $E_\gamma \approx 0$ region in the plots corresponds to the elastic peak of the cross section. For electrons, the photons have a higher probability of being radiated either along the initial or final electron directions. It is important to see that a large number of high energy photons go forward, which means that the incident lepton loses energy due to the emission of a hard photon. This phenomenon will cause the probability for the lepton to be scattered by the proton to increase. For muons, the photons are spread over a broader angular range, and most of the photons carry small energy.

3.5 Physics Models Comparison

Besides the ESEPP event generator, there are many other event generators and theoretical predictions for the lepton proton scattering experiment in MUSE kinematics. This makes them comparable at some points. The comparisons between ESEPP and other physics models are discussed below.

3.5.1 Monte Carlo generator ELRADGEN

The Monte Carlo generator ELRADGEN was developed by Afanasev et al. [61] for elastic unpolarized *ep* scattering which takes into account QED radiative effects. It follows the technique proposed by Bardin and Shumeiko [62] and calculates the non-radiated (Born term, vacuum polarization term and lepton vertex correction term), and radiated (initial-state and final-state bremsstrahlung effect from lepton leg) contributions. Based on that, they updated the theory model to include the lepton mass, two-photon effect, hard bremsstrahlung effect [63] and extended to polarized

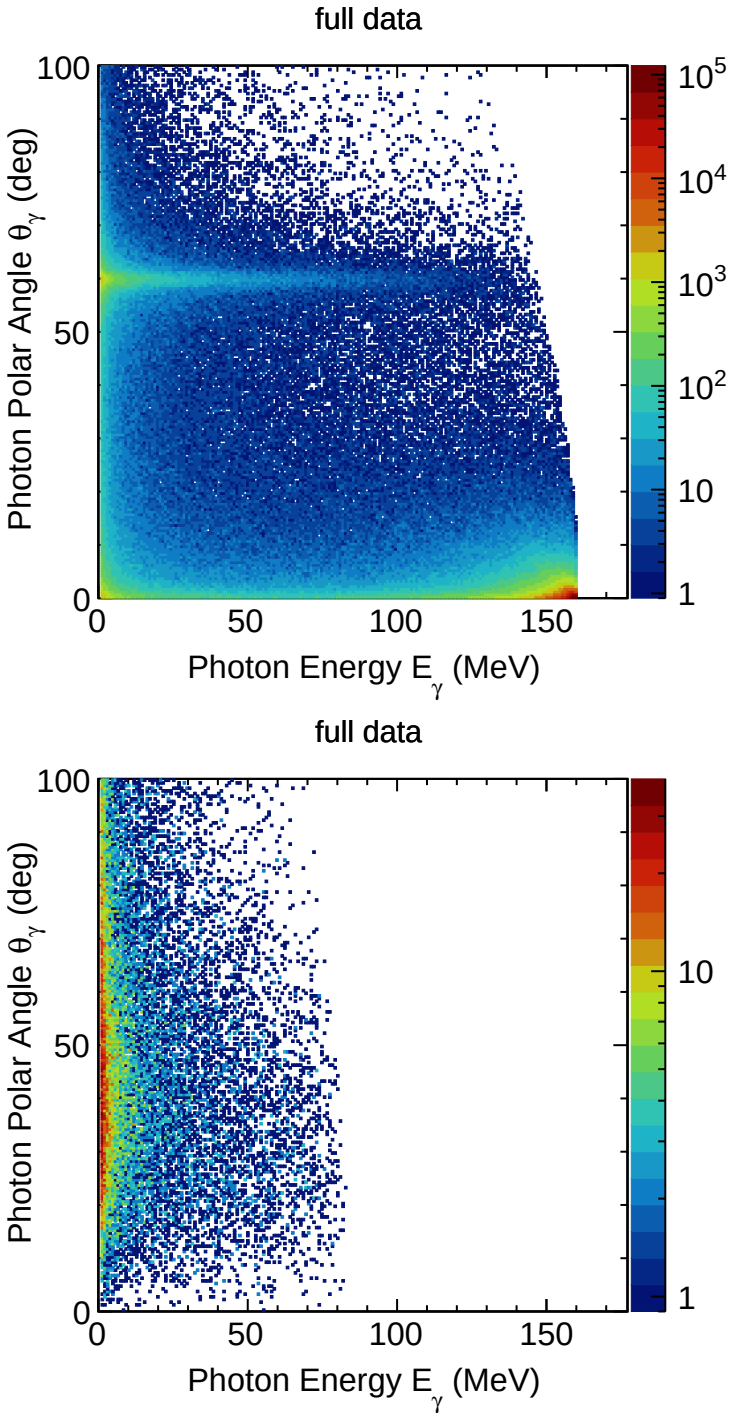

Figure 3.7 Photon distribution of photon polar angle versus photon energy from the ESEPP event generator and a beam momentum of 161 MeV/c and scattering angle of 60° for electron (top panel) and muon (bottom panel) scattering.

particles-ELRADGEN 2.0 [64]. These improvements make it suitable to calculate the radiative corrections for electron and muon scattering for MUSE.

In their recent publication [65], they discuss the calculation of radiative corrections in unpolarized elastic ℓp scattering for fixed Q^2 versus fixed scattering angle θ. The numerical analysis in MUSE kinematic conditions is shown in Fig. 3.8. It can be seen that the radiative correction values are different at lower scattered lepton momentum (hard photon emission) for those two cases. The group also calculated the charge asymmetry in a generalized soft-photon approximation approach [66] and including hard-photon emission [67]. The numerical results in MUSE kinematic conditions show that the magnitude of the asymmetry is reduced with decreasing of Q^2 and the value of the asymmetry is higher for the lighter lepton.

3.5.2 OLYMPUS/Darklight Radiative Event Generator

Another alternative radiative event generator that has been used in an elastic electron scattering experiment is the OLYMPUS/Darklight radiative event generator [68, 44, 69]. The advantages of the OLYMPUS event generator are: first of all, it uses exact first-order bremsstrahlung calculation following theory in [40] without using the soft-photon approximation. So the hard photons from the bremsstrahlung effect can propagate in the entire Monte Carlo simulation; second, this event generator is a weighted generator, which produces multiple weights for each event. The disadvantage of the OLYMPUS/Darklight event generator is that it ignores the mass of the lepton in some calculations which may be not suitable for muons. There are two methods in OLYMPUS/Darklight event generator, one is called the exponentiating method, and the other one is non-exponentiating method. In the exponentiating method, e^{δ} instead of $1+\delta$ is used to include higher order of the radiative corrections [44, 69],

$$\frac{\mathrm{d}^5\sigma}{\mathrm{d}\Omega_\ell \mathrm{d}\Omega_\gamma \mathrm{d}\Delta E} = e^{\delta} \times \frac{\mathrm{d}^5\sigma}{\mathrm{d}\Omega_\ell \mathrm{d}\Omega_\gamma \mathrm{d}\Delta E}_{\text{brems}}, \tag{3.37}$$

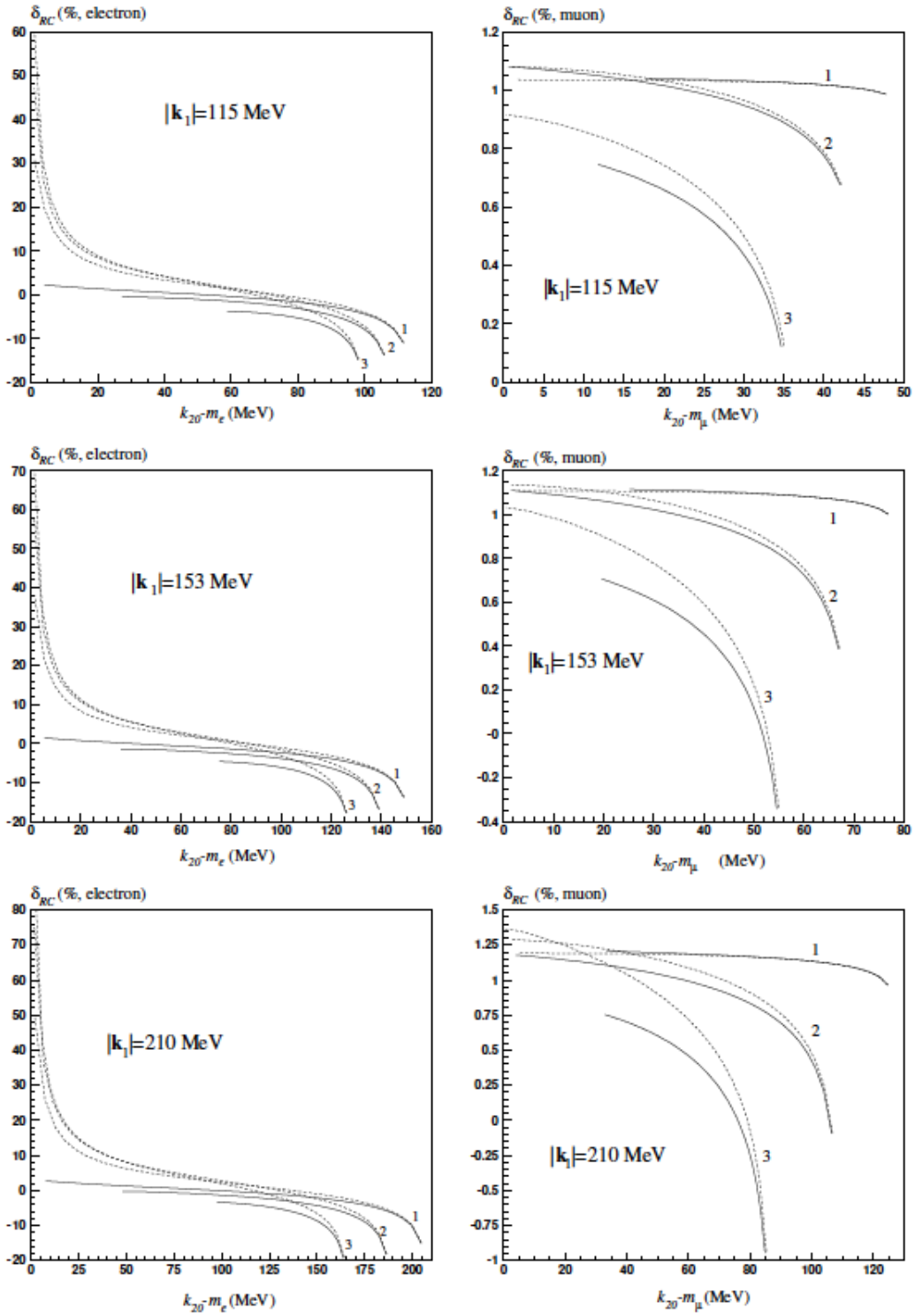

Figure 3.8 Relative radiative corrections vs the value of the scattering lepton kinetic energy for elastic ep and μp scattering, beam momenta are equal to 115 MeV/c, 153 MeV/c and 210 MeV/c for $\theta = 20^\circ$ (1), 60° (2), 100° (3). Solid (dashed) curves correspond to fixed Q^2 ($\cos\theta$) conditions [65].

where $\delta(\Delta E_\ell)$ is the factorizable correction following Mo and Tsai [38] or Maximon and Tjon [39] under some assumptions. The quantity $\frac{d^5\sigma}{d\Omega_\ell d\Omega_\gamma d\Delta E}_{\text{brems}}$ is the tree-level bremsstrahlung cross section. The independent variables for this event generator are [44, 69]: lepton solid angle $\Omega_\ell(\theta_\ell, \phi_\ell)$; photon solid angle $\Omega_\gamma(\theta_\gamma, \phi_\gamma)$ and the energy loss of lepton $\Delta E_\ell = E_\ell^{\text{el}} - E'_\ell$, with the energy of the lepton in purely elastic scattering, E_ℓ^{el}, and the lepton energy E'_ℓ. The weight for each event in this method is

$$\omega = e^\delta \times \frac{\mathrm{d}^5\sigma}{\mathrm{d}\Omega_\ell d\Omega_\gamma \mathrm{d}\Delta E}_{\text{brems}} \times \frac{1}{P(\Omega_\ell)P(\Delta E_\ell|\Omega_\ell)P(\Omega_\gamma|\Omega_\ell \Delta E_\ell)}. \tag{3.38}$$

This method has some limitations. For example, this exponential method only works in the near-elastic limit; the expression of the factorizable correction factor δ is calculated under the assumption of the elastic kinematics, so it is not accurate in the highly inelastic tail. To calculate a more accurate correction instead of effectively accounting for the higher-order contribution, method 2, which is the non-exponentiating method is used. This method uses the same strategy as the ESEPP event generator, separating the events into elastic and inelastic parts with a photon energy cut k_{cut}, but with weight. When the photon energy is less than k_{cut}, the event is considered elastic, and the weight is

$$\omega_{\text{el}} = \frac{\mathrm{d}\sigma_{\text{Born}}}{\mathrm{d}\Omega} \times (1+\delta) \times \frac{1}{P(\Omega_\ell, \Omega_\gamma, \Delta E_\ell)}. \tag{3.39}$$

When the photon energy is larger than k_{cut}, the event is considered inelastic, and the weight is

$$\omega_{\text{inel}} = \frac{\mathrm{d}^5\sigma}{\mathrm{d}\Omega_\ell \mathrm{d}\Omega_\gamma \mathrm{d}\Delta E}_{\text{brems}} \times \frac{1}{P(\Omega_\ell, \Omega_\gamma, \Delta E_\ell)}. \tag{3.40}$$

Figure 3.9 shows in the top panel a comparison of the differential cross section as a function of outgoing electron momentum between the ESEPP and OLYMPUS/Darklight event generators. The electron beam momentum in this example is 210 MeV/c and the scattering angle is 30°. Both event generators use the Dipole proton form factor. Both methods 1 and 2 are included. The cross section can be

obtained by integrating the radiative tail from a cut value $p'_{\min}$ on the outgoing lepton momentum. The bottom panel shows the radiative correction factor difference as a function of $p'_{\min}$ between the two event generators. It can be seen that they have a big difference in the elastic peak range and deep inelastic range. In this case, the radiative correction factors are different between ESEPP and OLYMPUS/Darklight at starting point $p'_{\min} = 0$. With the increasing detection threshold, the difference becomes smaller and can be neglected.

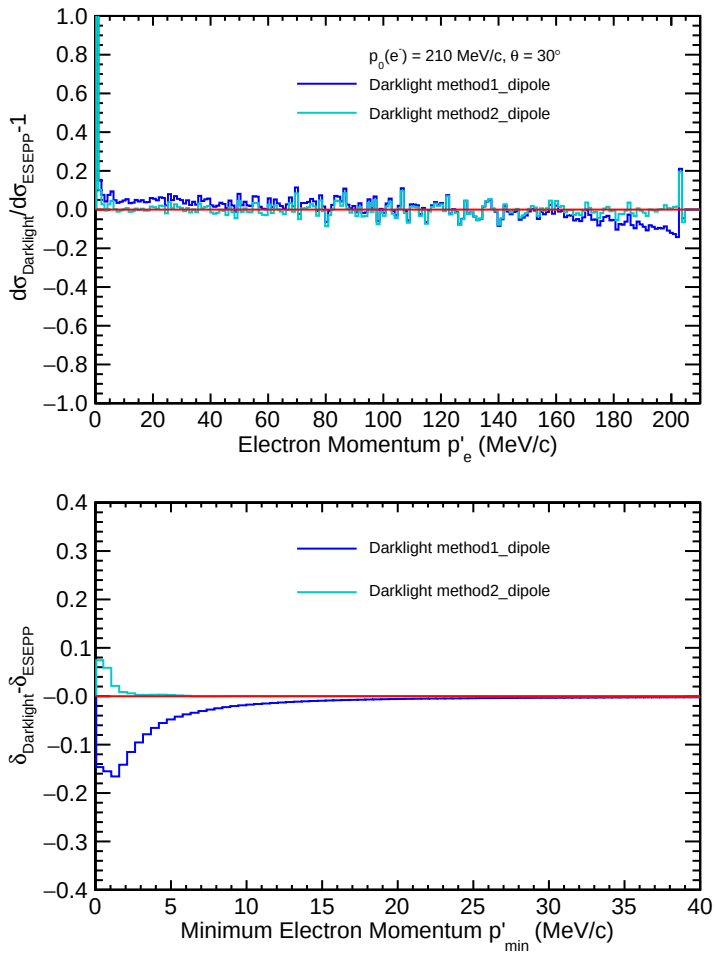

Figure 3.9 The ratio of the differential cross section with elastic peak and radiative tail from ESEPP and Darklight event generators (top) and the radiative correction factor difference (bottom) at electron beam momentum 210 MeV/c and scattering angle 30°.

3.5.3 Radiative Corrections in Chiral Perturbation Theory

The proton mass is large compared to the lepton momenta in MUSE, so the radiative correction process can be evaluated using the effective low-energy field theory of QCD. The theory group at USC has developed a perturbative procedure - the Heavy Baryon Chiral Perturbation Theory (HBχPT) [70, 71, 72] at low momentum range. In χPT, a well-defined momentum expansion scheme is used to study the contributions of the leading order (LO) as well as the higher order correction terms in a systematic way. The LO contributions in χPT are $\mathcal{O}(e^2)$, $\mathcal{O}(e^3)$..., while the NLO contributions are $\mathcal{O}(e^2, \frac{1}{M})$, $\mathcal{O}(e^3, \frac{1}{M})$... due to the proton's dynamical recoil effects [60, 73, 74, 41]. The lepton mass terms are kept, so this radiative correction prediction can be used for both electrons and muons. The comparison of the differential cross section with the radiative tail as a function of outgoing lepton momentum among ESEPP event generator, χPT (Pulak) bremsstrahlung calculation [75] and MoT bremsstrahlung calculation is shown in Fig. 3.10. The lepton beam momentum is 210 MeV/c and the scattering angle is 30°. The bremsstrahlung calculation in ESEPP and MoT includes photons that are emitted from the lepton and proton sides, while χPT (Pulak) only considers photons emitted from the lepton side, which is form factor model independent. In [60, 73], the author also demonstrated that the peaking approximations [38], which is viable for electron scattering at the low-momentum MUSE kinematics, can not be applicable for muon scattering at MUSE energies. In their later published paper [41], they include all the LO and NLO radiative correction to elastic lepton proton scattering in the low energy effective field theory of HBχPT, and the work predicts that the total radiative correction including NLO is 0.25 for electrons and no more than 0.02 for muons in MUSE kinematic range.

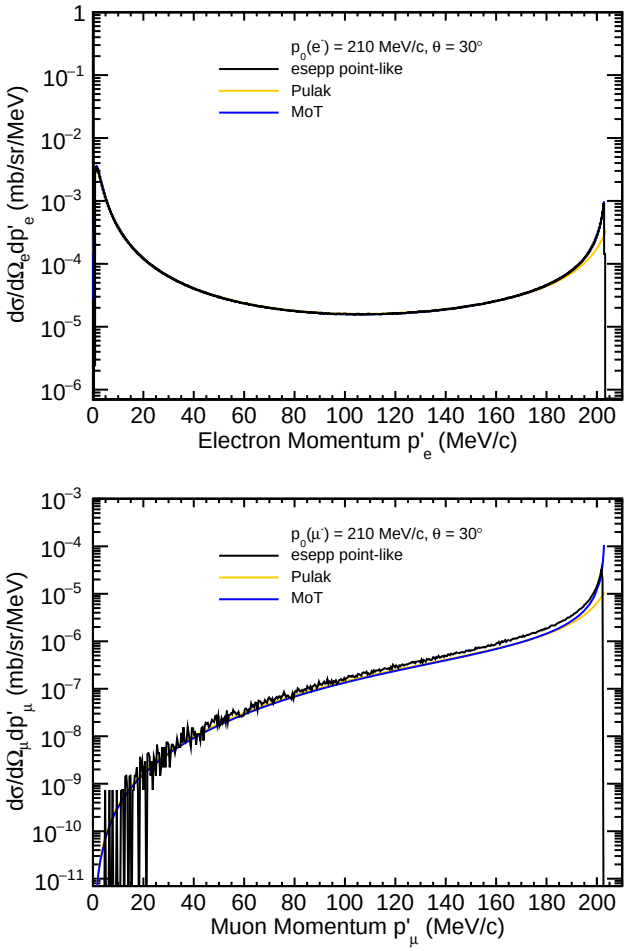

Figure 3.10 The differential cross section radiative tail from ESEPP, HBχPT (Pulak) bremsstrahlung calculation (LO with recoil) and MoT bremsstrahlung calculaton for electrons (top) and muons (bottom) for a beam momentum of 210 MeV/c and scattering angle 30°.

3.5.4 Monte Carlo for MUons and other LEptons

Another theory that is discussed during this work is "Monte Carlo for MUons and other LEptons" (McMule) developed by PSI theory group [42, 76]. McMule aims to calculate the theoretical predictions of radiative corrections precisely for a wide range of low-energy processes dominated by QED effects. It includes high-order QED calculations and the code is encapsulated in a Fortran 95 framework. It can be applied to the MUSE experiment including the dominant NNLO corrections. The computation of radiative corrections in the lepton-proton scattering includes the LO (Born

term), the NLO (the first-order bremsstrahlung effect when a photon is emitted by the initial-state and final-state lepton, the vacuum polarization, and lepton vertex corrections) and dominant NNLO (two-loop amplitudes, two-photon bremsstrahlung effect) [77]. At NLO, the infrared-divergent (IR) terms are cancelled between the lepton vertex correction and the lepton bremsstrahlung correction; the vacuum polarization (VP) term does not contain any IR term so it can be factorized in the soft photon approximation. There is no difference between positive and negative charged leptons due to the absence of two-photon exchange. At NNLO, the situation becomes more complicated, for example, the vacuum polarization (VP) is not factorizable any longer [78]. Some other calculations considering the effects beyond the soft approximation [79] and the NNLO effects [80, 81, 82] are presented to improve the radiative corrections in lepton proton scattering. One result of the integrated cross section from McMule for *ep* elastic scattering is listed in Table 3.2 [42]. In this case, the incoming electron energy is 155 MeV, the scattering angle is in the range 25° - 45°, and the outgoing electron beam cut is 45 MeV. The quantities $\sigma^{(0)}$, $\sigma^{(1)}$, and $\sigma^{(2)}$ are the cross sections for LO, NLO, and NNLO, respectively. The terms $\sigma^{(1)}_{VP}$ and $\sigma^{(2)}_{VP}$ are the vacuum polarization contributions at NLO and NNLO. The total cross section is $\sigma_2 = \sigma^{(0)} + \sigma^{(1)} + \sigma^{(2)}$. The value $\delta K^{(i)} = \sigma^{(i)}/\sigma^{(i-1)}$ quantifies the effect of higher-order contributions. The result shows that the NLO correction is about 5%, while the NNLO is below 0.1% [42]. Under the same condition, the integrated cross section from the ESEPP event generator is 36.3002 μb.

The integrated cross section from McMule for μp elastic scattering is listed in Table 3.3. The incoming muon momentum is at MUSE kinematic 210 MeV/c, and the scattering angle in the MUSE acceptance 20° - 100°. The result shows that the corrections for muon scattering are smaller than for electrons, and the NLO correction is about 1.3%, while the NNLO is below 0.02% [42]. The integrated cross section in this case from the ESEPP event generator is 49.912 μb. Although the McMule does

Table 3.2 The integrated cross section from McMule for E_e = 155 MeV, $25^\circ < \theta < 45^\circ$, $E'_e > 45$ MeV at LO, NLO, and NNLO [42].

	σ (μb)	$\delta K^{(i)}$ (%)
$\sigma^{(0)}$	34.5392	
$\sigma^{(1)}$	1.7763	5.1430
$\sigma^{(1)}_{VP}$	0.04663	1.3501
$\sigma^{(2)}$	-0.0237	-0.0653
$\sigma^{(2)}_{VP}$	0.0132	0.0364
$\sigma_2 = \sigma^{(0)} + \sigma^{(1)} + \sigma^{(2)}$	36.2919	

Table 3.3 The integrated cross section from McMule for p_μ = 210 MeV/c, $20^\circ < \theta < 100^\circ$ at LO, NLO, and NNLO [42].

	σ (μb)	$\delta K^{(i)}$ (%)
$\sigma^{(0)}$	49.6677	
$\sigma^{(1)}$	0.6541	1.3170
$\sigma^{(1)}_{VP}$	0.7172	1.4440
$\sigma^{(2)}$	0.0075	0.0150
$\sigma^{(2)}_{VP}$	0.0076	0.0151
$\sigma_2 = \sigma^{(0)} + \sigma^{(1)} + \sigma^{(2)}$	50.3294	

not include full LO corrections, it gives a prediction of NNLO effects on the cross section. More Feynman diagrams are being developed to improve the code.

3.6 Discussion

The theoretical calculations for the radiative corrections are well established and used widely in scattering experiments. The physics models mentioned above are good candidates to predict the radiative corrections for the MUSE experiment. As can be seen from the comparison of the results above, the radiative corrections values are different between different models (e.g., OLYMPUS and ESEPP, McMule and ESEPP). One reason is that they include different Feynman diagrams. The other reason is they use calculations with different assumptions even for the same diagram. Also the higher-order radiative correction (NLO, NNLO) prediction values are different (USC group

and McMule). The MUSE experiment will measure the scattered lepton over a large angular range, and there are several requirements to estimate the radiative correction. First, the mass of μ is not negligible compared to the beam momentum in MUSE, so the calculation should avoid using the $Q^2 \gg m^2$ approximation. Second, besides the internal processes where a photon is emitted during the lepton-proton scattering, the external processes, that coincide with the passage of incident and scattered particles through the upstream detector and target materials have to be considered, the calculation should include the emission of a hard radiated photon, which is beyond the soft-photon approximation. In addition, to study the full effect propagated by the hard photon, a Monte Carlo simulation with an event generator should be implemented for MUSE. Finally, because radiative corrections depend on the experimental setup, the knowledge of the acceptance, efficiency, and energy resolution impacts the uncertainties of radiative corrections. The uncertainty of radiative corrections from the knowledge of the detectors is the largest contributor to the systematic uncertainties in MUSE. For these purposes, the ESEPP event generator is used to study the radiative correction and its uncertainties in the MUSE experiment.

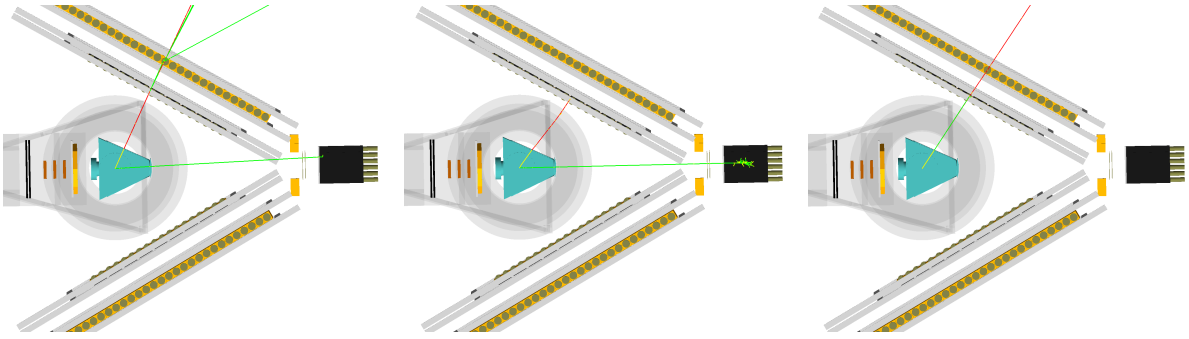

(a) (b) (c)

Figure 3.11 Three cases of $\ell^{\pm}p \to \ell'^{\pm}p'\gamma$ from ESEPP in Geant4 simulation starting at the reaction vertex. Red lines represent electron trajectories and green lines photons. (a) Initial-state radiation and electron momentum $p'_e > p'_{\text{min}}$. (b) Initial-state radiation and electron momentum $p'_e < p'_{\text{min}}$. The final-state electron does not reach the SPS rear wall. (c) Final-state radiation and electron momentum $p'_e > p'_{\text{min}}$.

During the bremsstrahlung effect in the scattering process, photons are coming

from either the initial state or finial state of the lepton. When including the ESEPP event generator within the MUSE target in the Geant4 simulation, three simulated event types with a scattering angle of 60° (STT not shown) are shown in Fig. 3.11:

- Initial-state photon production with a hit in the calorimeter. The scattered electron momentum p'_e is above the SPS momentum-threshold, p'_{min}, and the electron is detected in the SPS walls.
- Very hard initial-state radiation and not enough energy left for the electron to punch through the front wall. Such an event would not trigger the event readout.
- Final-state radiation. The bremsstrahlung photon is along the direction of the scattered electrons.

In the MUSE experiment, the SPS detectors detect the angle of the scattered particles but not the momentum. Therefore, a photon detector is needed downstream to detect and subsequently suppress the lepton initial-state radiation.

Chapter 4

Experimental Parameters that affect Radiative Corrections

4.1 Minimalistic Simulation with ESEPP Event Generator

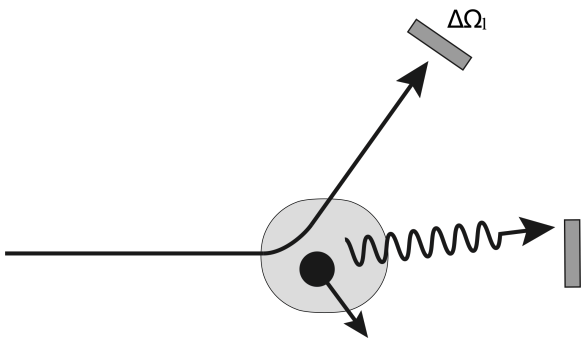

Figure 4.1 A sketch of a minimalistic simulation in MUSE shows the first-order bremsstrahlung process $\ell^{\pm}p \to \ell'^{\pm}p'\gamma$.

In order to understand the radiative correction in the MUSE experiment, a simple simulation with the ESEPP event generator was performed to obtain the Bremsstrahlung cross section σ_{brems}. Figure 4.1 shows a sketch of an electron scattered off a proton while emitting an initial-state Bremsstrahlung photon in the forward direction. The internal radiative correction, δ, can be obtained by comparison with the Born term,

$$\int_{p'_l}\int_{\Omega_\gamma} \frac{d\sigma_{\text{brems}}}{d\Omega_l d\Omega_\gamma dp'_l} d\Omega_l dp'_l = \frac{d\sigma}{d\Omega_l} = \frac{\mathrm{d}\sigma_{\text{Born}}}{\mathrm{d}\Omega_l}\left[1+\delta\right], \tag{4.1}$$

$$\delta = \left(\frac{\mathrm{d}\sigma}{\mathrm{d}\Omega_l}\right) \Big/ \left(\frac{\mathrm{d}\sigma_{\mathrm{Born}}}{\mathrm{d}\Omega_l}\right) - 1. \tag{4.2}$$

The size of the radiative corrections depends on the

- beam momentum p_0,
- lepton scattering angle θ,
- momentum threshold p'_{min} for the detection of the scattered lepton,
- energy threshold for the identification of hard photons in the calorimeter E_γ.

4.2 Beam Momentum

In order to determine precise cross sections, it is required to know the momentum of the beam particles and its uncertainty. To control the relative cross section uncertainty to 0.1%, the relative error in the πM1 channel momentum is desired to be no larger than 0.2% - 0.3% [47]. The beam momentum can be verified with time-of-flight measurements from the beam hodoscope to the beam monitor using various settings for the detector distance and modifying the lengths of the flight-path. Since electrons have a small mass of 0.511 MeV/c^2, the speed of electrons is close to the speed of light for MUSE beam momenta. They confirm the path length in time-of-flight measurements. Measured particle speeds of muons and pions, with masses of 105.67 MeV/c^2 and 139.57 MeV/c^2, respectively, allow for the determination of their momenta. The beam hodoscope timing information along with the accelerator RF signal allows monitoring the particle-momentum stability, and provides an additional means to determine particle momenta.

4.3 Detector Properties

4.3.1 Scattering Angle

The cross section is sensitive to the scattering angle. The scattering angle of the particle is determined by the reconstructed trajectories at the vertex inside the target determined by the tracking detectors (GEM and STT). The uncertainty of the scattering angle is mainly from the multiple scattering in the target and detector. These effects were simulated in Geant4 assuming a realistic scattering target geometry, while accounting for detector resolution. The results are plotted in Fig. 4.2, the red dots show the differences between the generated and reconstructed scattering angles in the ep and μp reactions, respectively. The gray curves show results of Gaussian fits to the data, with the mean and width values indicated. The mean value is close to 0 and the standard deviation is smaller than 20 mrad. Since MUSE data will be summed over a certain angular range to determine the cross section, the average uncertainty of the scattering angle is reduced. The averaged scattering angle is determined to 0.2 mrad, to keep the cross section uncertainty under control.

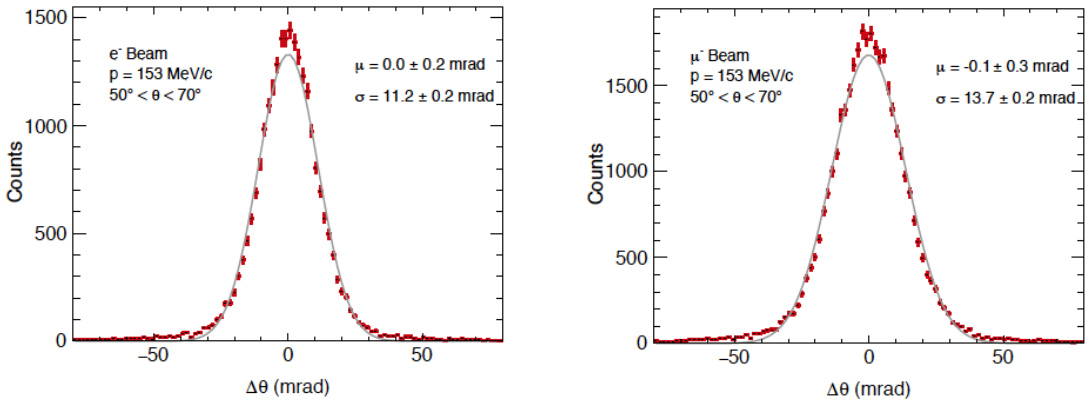

Figure 4.2 Examples of differences between reconstructed and actual reaction scattering angles from simulations for electrons (left panel) and muons (right panel) with a beam momentum of 153 MeV/c and an average scattering angle of 60° [32].

4.3.2 Lepton-Momentum Threshold of the SPS

Nominal Acceptance

There are two SPS walls on each side of the MUSE beamline. MUSE covers a horizontal angular range θ from 20° to 100° from all points within the target, and an azimuth ϕ from $-45°$ to $+45°$ at $\theta = 60°$, which is the nominal acceptance of the experiment. The SPS walls are perpendicular to $\theta = 60°$. The original detector design specified a distance of 52 cm from the center of the target to the front face of the SPS front-wall. This gave 104 cm as the minimum length of a vertical scintillator bar of the front-wall and it was rounded up to 120 cm to allow for a tolerance. The rear wall face to target distance was 74 cm and gave 148 cm as the minimum detector length and a final choice of 220 cm. The physical size of the two planes is larger than the detection area because multiple scattering will diverge the trajectories, especially for low momentum muons. Figure 4.3 shows a sketch of the detection area on the front wall. Within the angular range, the defined detection area is colored green. However, the final setup has the front-wall surface shifted by 5 cm because the STT needed more clearance. With a distance of 57 cm, the minimum front-wall detector length to cover ϕ from $-45°$ to $+45°$ at $\theta = 60°$ is 114 cm, reducing the tolerance. Particles in the nominal acceptance are closer to the ends of the scintillation bars, especially if taking various vertex positions within the target volume into account. Some particles, for example, striking close to one end of the scintillator bar, can be detected by one PMT, but do not have enough energy deposition to be detected by the farther PMT. Therefore, the detection efficiency of the particles is important in the analysis and it is related to the threshold of detecting the particles in both PMTs, which is position dependent. Issues like multiple scattering (which affects the angular direction of the particle tracks), energy deposition, attenuation, discriminator threshold, and coincidence requirements, as well as the inactive parts of the SPS detector (gaps, wrapping material) affect the overall detection efficiency. To maintain high efficiency, the same

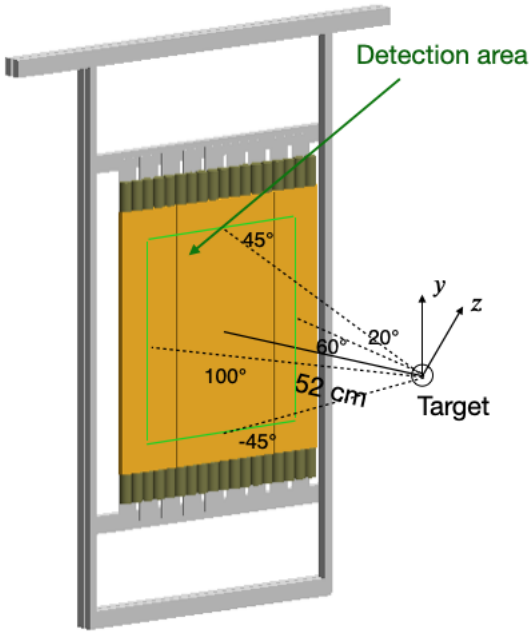

Figure 4.3 Cartoon of the SPS front wall. The "detection area", marked in green, specifies the nominal SPS detector acceptance that is based on a wall distance of 52 cm and is used in this study.

detection area, which is the inner part of the front wall, is used to study the detection threshold.

Light Output

In a scintillator, when a particle interacts with the scintillation material, it loses energy through ionization [83]. Then it causes the emission of light and the light travels through the material by total internal reflection. The light created in the scintillator strikes the photocathode of a photomultiplier tube (PMT) and releases photoelectrons. These electrons are accelerated using a voltage to strike the first dynode and release additional electrons. These secondary electrons go to a second dynode and release more electrons. Further electrons are released at each subsequent dynode stage that has a higher electric potential than the previous one. Finally, the electron signal is multiplied and is able to produce an electrical pulse at the anode

stage. The anode PMT pulses are discriminated, giving the signal's time of arrival, which is digitized with a time-to-digital converter (TDC); the corresponding dynode PMT pulse is integrated by a charge-to-digital converter (QDC). The scintillator light output is energy calibrated with gamma-ray sources following the method of Refs. [84, 56]. The attenuation length λ, defined as the length that the signal travels through in the scintillator when it is reduced to $1/e$, is an important property and is used to describe how rapidly the signal is attenuated in the scintillator. The attenuation length of EJ-204 is 160 cm [85]. This value can be verified from the light outputs at the up and the down PMTs. Figure. 4.4 illustrates the method to measure the attenuation length.

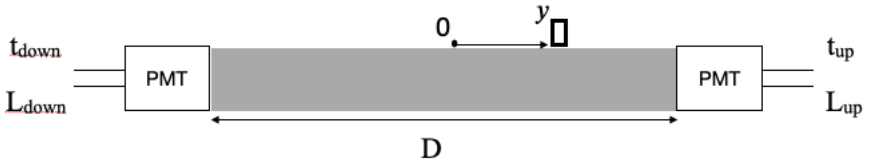

Figure 4.4 A schematic view of the measurement of the attenuation length with a source or hit position at y and light output signals at the up and down PMTs.

In the Lab frame, assuming that the y-axis is along the length of the scintillator bar and positive direction is pointing up, y is the position where a charged particle interacts with the scintillation material and $y = 0$ is at the center of the bar with length D. The values L_{down}, L_{up} are the light output signals (QDC) at the down and up PMTs. They depend on the energy deposition of the paticle in the scintillator Q and the calibration constants c_1 and c_2. The light outputs can be expressed as,

$$L_{\text{down}} = c_1 Q e^{-(y+D/2)/\lambda}, \tag{4.3}$$

$$L_{\text{up}} = c_2 Q e^{-(D/2-y)/\lambda}. \tag{4.4}$$

If the gains of the two PMTs are matched and the detector is symmetric, the calibra-

tion constants $c_1 = c_2$. The expressions above can be rewritten as,

$$L_{\text{down}} = Qe^{-y/\lambda}, \tag{4.5}$$

$$L_{\text{up}} = Qe^{+y/\lambda}, \tag{4.6}$$

assuming a detector calibration such that the geometric mean $\sqrt{L_{\text{up}}L_{\text{down}}} = Q$. The attenuation length λ can be obtained from $\ln \frac{L_{\text{down}}}{L_{\text{up}}}$. The position where a charged particle interacts with the scintillator material can be obtained from the time difference $t_{\text{up}} - t_{\text{down}}$.

Detection Threshold

The detection threshold and the acceptance of the SPS were studied with Geant4 Monte Carlo simulations. In those simulations, 10^7 leptons with MUSE momenta and initial positions within the target volume were uniformly thrown into the full solid angle. Figure 4.5 shows one example of ten electrons with momenta of 210 MeV/c in the Geant4 simulation. The momenta of the outgoing particles are chosen according to elastic-scattering kinematics with fixed beam momentum. Hit positions and energy depositions of charged particles in the SPS detectors were recorded in the simulation for each event.

Whether or not a particle is detectable in the SPS depends on the light output it generates and the SPS discrimination threshold. For scattered particles, the trigger requires at least one above-threshold signal in a PMT on the up side of an SPS wall and at least one such signal in the down side. Both the front and rear walls, must have recorded a hit for an event to be read out. To study the detection efficiency, the largest light output on the up side of any detector was determined, and likewise for the down side. The smaller of these two maximal output values determines if a hit is above threshold on both sides.

Simulated energy depositions for scattered particles traversing the 6 cm $\times$ 3 cm bars of the front and 6 cm $\times$ 6 cm bars of the back wall at different scattering angles

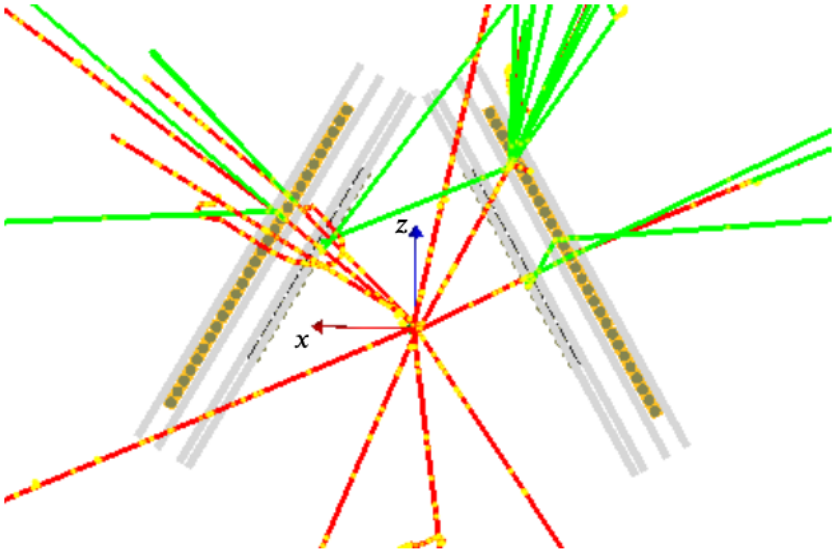

Figure 4.5 Example of Geant4 simulation to study energy deposition in the SPS. In this case, ten electrons with momenta of 210 MeV/c were thrown in the target volume and spherically uniform directed into the full solid angle. Red trajectories show electron trajectories and green ones are for secondary photons.

are shown in Fig. 4.6. The set of solid curves is for 210 MeV/c beam particles, and the set of dashed curves is for 115 MeV/c beam particles. In the study range, the energy depositions for e^- are mostly independent of the beam momentum since they deposit energy through minimum ionization [83]. For μ^-, particles with the lower beam momentum deposit more energy than those with higher beam momentum. Mostly all events have energy depositions above 1 MeV. The energy deposition of e^+ (μ^+) is similar to e^- (μ^-).

By restricting the analysis to events that have original trajectories into the detection area, the efficiency for the scattered-particle scintillator walls at 210 MeV/c beam energy is shown in Fig. 4.7 for electrons and muons as a function of the particle scattering angle at various discriminator threshold. The plots give the ratio of events with an above discriminator threshold hit in the detection area of the scintillator plane per incident particle. The efficiency varies with scattering angle and decreases with an increasing threshold. The average efficiency is higher for lower momenta $\mu^{\pm}$ but about the same value for $e^{\pm}$ (not shown). Considering the energy calibration of

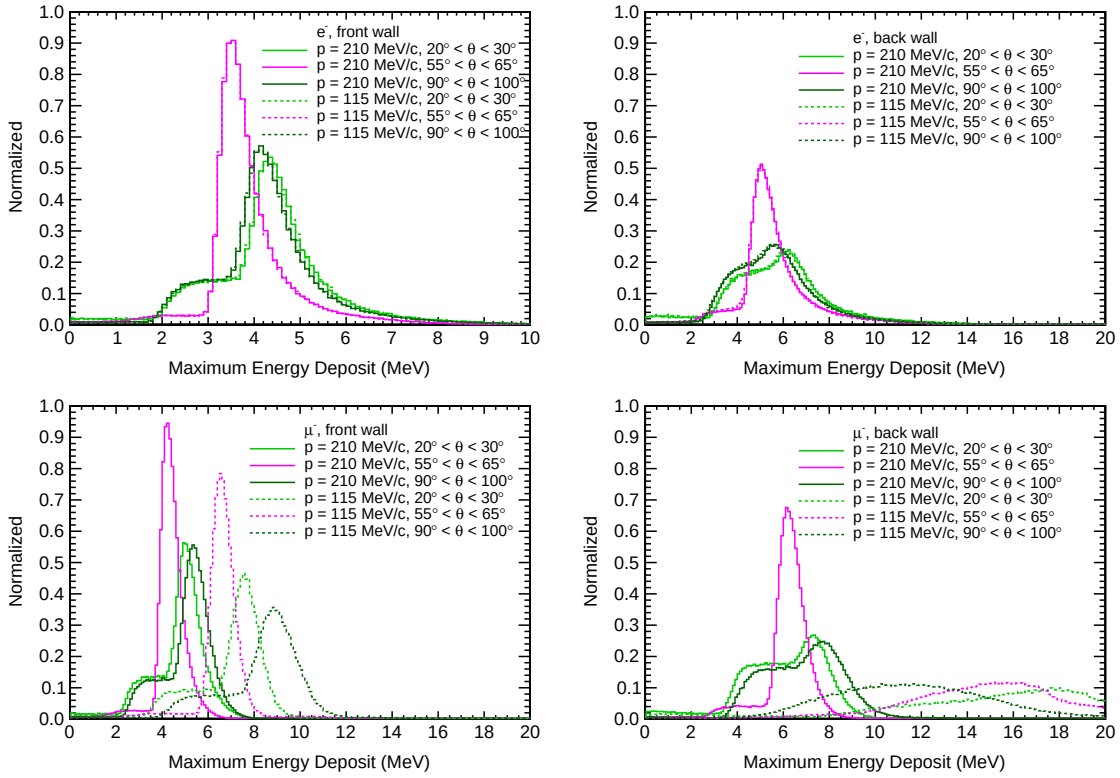

Figure 4.6 Simulated energy deposition for scattered electrons traversing the 6 cm × 3 cm bars of the front (top left) and 6 cm × 6 cm bars of the back wall (top right); scattered muons traversing the front (bottom left) and rear wall (bottom right). The simulation recorded for each event (primary particle) the maximum energy deposition in the scintillator bars.

SPS detectors, $E_{th} = 2.0$ MeV can be selected, resulting in an efficiency >99%.

Looking at the front wall and back wall on one side of the beamline, Fig. 4.8 shows the estimated acceptance in dependence of the scattering angle for the front wall (left panel) and the back wall (right panel). It is defined as the ratio of electrons with a hit in an angular bin and electrons thrown in that angular bin. The angular cut in the spherical coordinate has a cone-shape on the scintillator walls. The black curve is the acceptance of the scintillator wall as a function of the scattering angle, and the green curve is the acceptance within the detection area. To maintain a high efficiency of the SPS, the acceptance needs to be restricted.

At the threshold $E_{th} = 2.0$ MeV for both front and rear walls, the detection efficiency as a function of scattered lepton momentum at different scattering angles

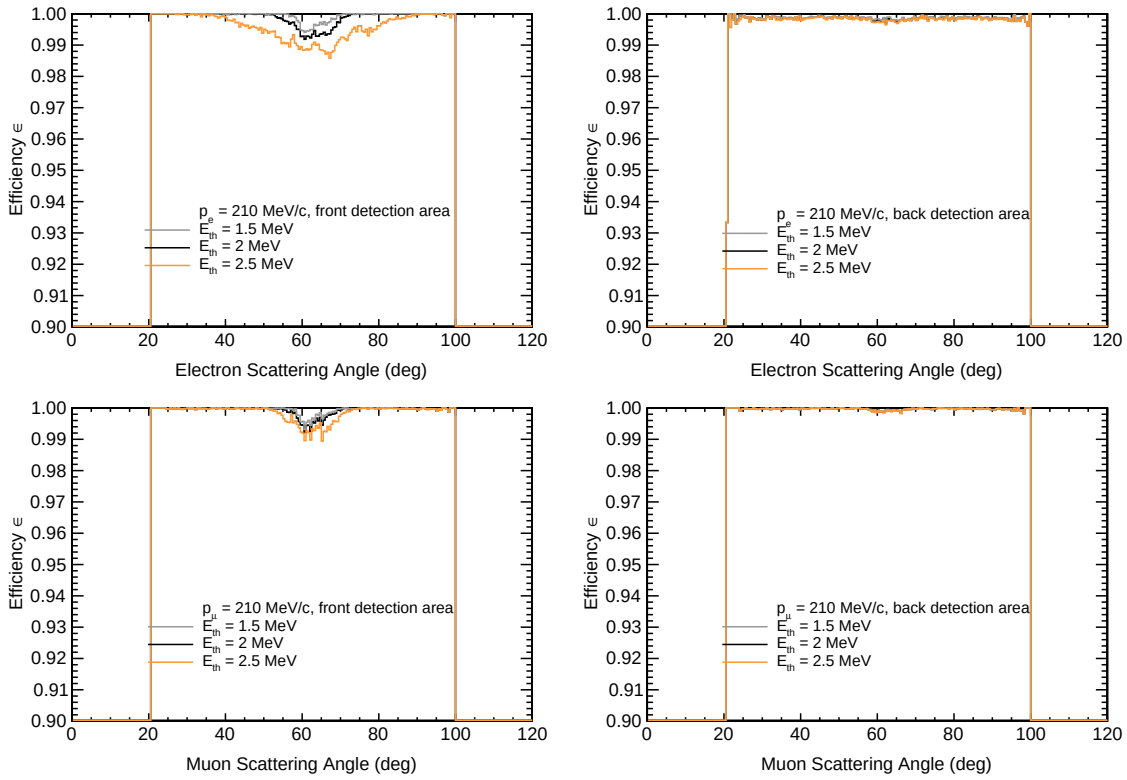

Figure 4.7 The SPS efficiency as a function of scattering angle at various discriminator thresholds considering events that hit the detection area. Top left: front area for electrons. Top right: back area for electrons. Bottom left: front area for muons. Bottom right: back area for muons.

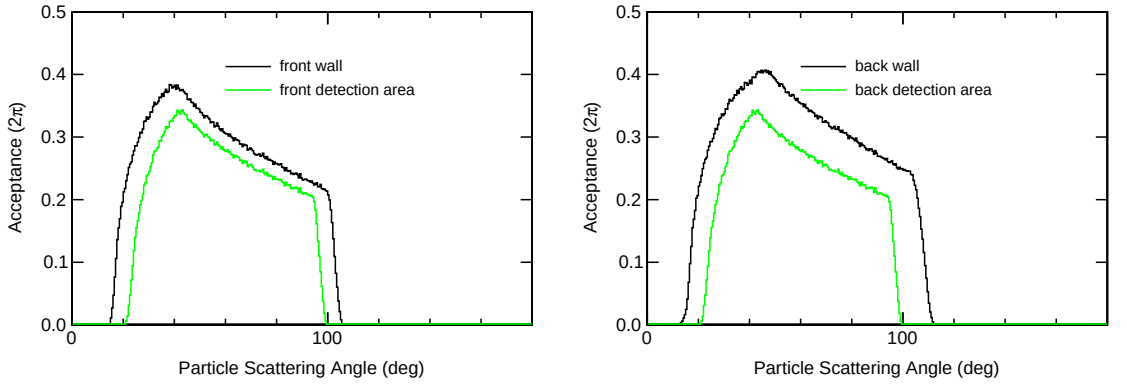

Figure 4.8 Geant4 simulation estimates the acceptance of front scintillator wall (left panel) and back wall (right panel).

is shown in Fig. 4.9. The data points from the simulation show the fraction of events detected by both front and rear walls at different scattering angles. It can be seen that the events can be detected nearly 100% for electrons with momenta

above 45 MeV/c and muons with momenta above 85 MeV/c. In the following we define as lepton detection threshold $p'_{\rm min}$ the momentum for which the efficiency is 50%, $\epsilon(p'_{\rm min}) = 0.5$. This value can be obtained by fitting the simulated data with a three-parameter fit function

$$\epsilon(p) = \epsilon_0 \left(1 - \frac{1}{e^{\frac{p-p'_{\rm min}}{\Delta p}} + 1} \right), \tag{4.7}$$

where the first fit parameter is the detection threshold $p'_{\rm min}$, the second fit parameter is Δp and controls the width of the function along the momentum-axis, and the third fit parameter ϵ_0 determines the scale of the function along the ϵ-axis. The fits are shown as gray curves in Fig. 4.9.

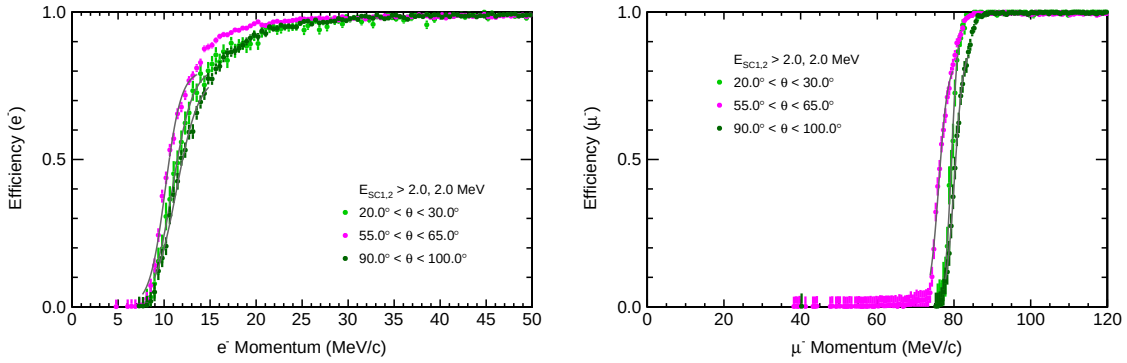

Figure 4.9 Estimated SPS momentum-detection efficiency as a function of scattered lepton momenta at different scattering angles.

The values of the momentum detection threshold $p'_{\rm min}$ for e^- are shown in Table 4.1 and for μ^- in Table 4.2. Here, $E_{SC1,2}$ are the assumed thresholds of the SPS discriminators for the front and rear planes, respectively. The $p'_{\rm min}$ values vary with the lepton polar angle as the particles traverse scintillation material with different path lengths. The detection threshold also varies with the threshold values of the SPS discriminators for the front and rear planes, $E_{SC1,2}$. MUSE production data will allow for moderate changes of the SPS lepton momentum detection threshold in the data analysis and thus study systematic effects.

Table 4.1 SPS detection threshold $p'_{\min}$ for e^-.

e^-	$20° - 30°$	$55° - 65°$	$90° - 100°$
$E_{SC1,2} = 1.5$ MeV	10.5±0.2 MeV/c	9.6±0.1 MeV/c	10.6±0.1 MeV/c
$E_{SC1,2} = 2.0$ MeV	10.9±0.1 MeV/c	10.1±0.1 MeV/c	11.3±0.1 MeV/c
$E_{SC1,2} = 2.5$ MeV	11.4±0.1 MeV/c	10.8±0.1 MeV/c	12.1±0.1 MeV/c

Table 4.2 SPS detection threshold $p'_{\min}$ for μ^-.

μ^-	$20° - 30°$	$55° - 65°$	$90° - 100°$
$E_{SC1,2} = 1.5$ MeV	79.3±0.1 MeV/c	76.0±0.1 MeV/c	80.1±0.1 MeV/c
$E_{SC1,2} = 2.0$ MeV	79.3±0.1 MeV/c	76.0±0.1 MeV/c	80.2±0.1 MeV/c
$E_{SC1,2} = 2.5$ MeV	79.4±0.1 MeV/c	76.1±0.1 MeV/c	80.2±0.1 MeV/c

4.3.3 Calorimeter Performance

The performance of the calorimeter has been studied through simulation and experimental data. During the 2020 beam time, a momentum scan with electron beams from 230 MeV/c down to 20 MeV/c was performed. The experimental data were obtained with a 6 × 6 calorimeter without the four outer corners design. In the runs, the electron identification was done with the BH, and a hit in the BM was required to ensure a charged-particle signal in the calorimeter. For each momentum setting, the light-output signals from the nine calorimeter blocks that surround the one with the largest light output were summed up. If the block with the largest light output was not one of the central ones, the event was ignored in the analysis. Figure 4.10 shows a comparison between the simulation result (red curve) and experimental data (black curve) at 150 MeV/c. The simulation result agrees well with the data in the peak region.

The light-output signals for each beam momentum were used to determine the total energy signal and its resolution as shown in Fig. 4.10. The light output is a very nearly linear function of the electron momentum. The resolution varies with

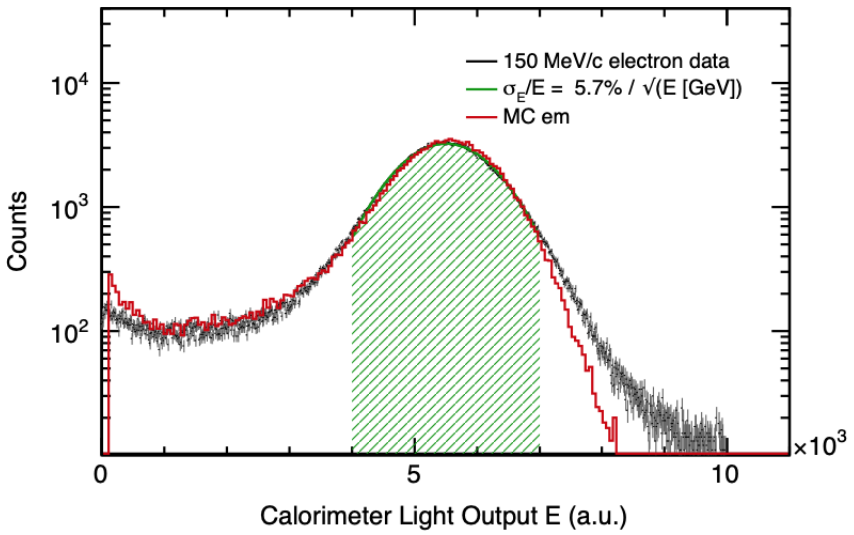

Figure 4.10 Example of the light-output signal from sum of nine calorimeter blocks with electron beam momentum at 150 MeV/c [86]. The analysis is for the 6 × 6 calorimeter without the four outer corners design.

momentum and can be fit as

$$\frac{\sigma}{E} = \sqrt{\frac{a^2}{E} + b^2 + \frac{c^2}{E^2}}. \tag{4.8}$$

Here $a = (5.37 \pm 0.08) \times 10^{-2}$ GeV$^{1/2}$ is the statistics term, $b = (3.34 \pm 0.75) \times 10^{-2}$ is the locus dependent light transmission term, and $c = (0.59 \pm 0.02) \times 10^{-2}$ GeV is the electronic noise term [86].

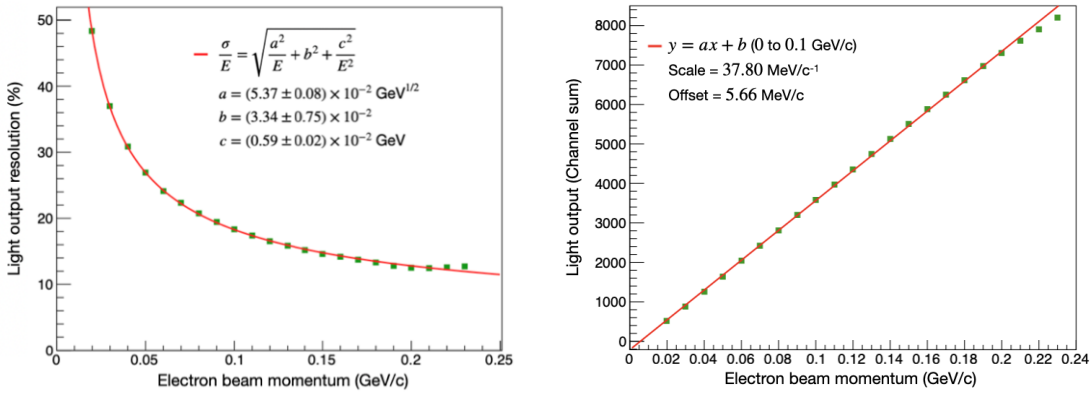

Figure 4.11 Calorimeter light-output signal resolution as a function of electron beam momentum (left) and light-output signal as a function of electron beam momentum (right) [86].

4.4 Uncertainties of Experiment Parameters

The uncertainties of p_0, θ, $p'_{\min}$, and E_γ can be obtained from the knowledge of experiment, see Table 4.3. The uncertainty of the beam momentum p_0 in the πM1 channel is 0.2% times the beam momentum. The averaged scattering angle uncertainty is expected to be smaller than 0.2 mrad. The uncertainties of the SPS detection threshold $p'_{\min}$ and the calorimeter threshold E_γ are related to how well the SPS detector and calorimeter can be calibrated. Here the relatively larger values based on the knowledge of the detectors, 2 MeV/c for $p'_{\min}$ and 5 MeV for E_γ, are chosen to calculate the uncertainty of the radiative correction in the next chapter.

Table 4.3 The uncertainties for p_0, θ, $p'_{\min}$, and E_γ.

X_i	σ_{X_i}
$p'_{\min}$	2 MeV/c
p_0	0.2% p_0
θ	0.2 mrad
E_γ	5 MeV

Chapter 5

Analysis and Results

5.1 ESEPP Simulation

With the calorimeter downstream, the initial-state-radiation contributions to the cross section are suppressed by detecting and rejecting high-energy photons. Using the minimalistic simulation with the ESEPP event generator and the detector properties mentioned in Chapter 4, the radiative correction for electrons and muons in the MUSE kinematics and their uncertainties will be discussed in detail in this Chapter. The 8×8 calorimeter sits at 140 cm downstream of the target. It covers a 32×32 cm^2 area without considering the material and gap between the blocks. 10^7 events with MUSE momenta generated by the ESEPP event generator were thrown into the forward (20° - 30°), the central (55° - 65°) and backward (90° - 100°) angular ranges. The lepton and photon momenta were recorded for each event. In the subsequent analysis the photon momentum was smeared following a Gaussian distribution according to the known calorimeter resolution, Eq. (4.8). The resulting photon-momentum distribution for photons within the geometrical acceptance of the calorimeter is an estimate of the reconstructed experimental data. Figure 5.1 shows the reconstructed photon momentum distribution (top panel) and cross section (bottom panel) at an electron beam momentum 161 MeV/c and scattering angle of 60°. The red curve on the top panel shows the reconstructed photon momentum in the calorimeter for the full event sample. A cut ($E_\gamma > 0.4\ p_0 c$ in this case) was applied on the *reconstructed photon energy* to veto events with photon energies larger than

0.4 p_0c, leaving the events shown by the green histograms.[1] After rejecting the events with high-energy photons, the radiative tail of the cross section is lowered by two orders of magnitude, which means that the dependence of the integrated cross section on the electron momentum detection threshold is largely reduced.

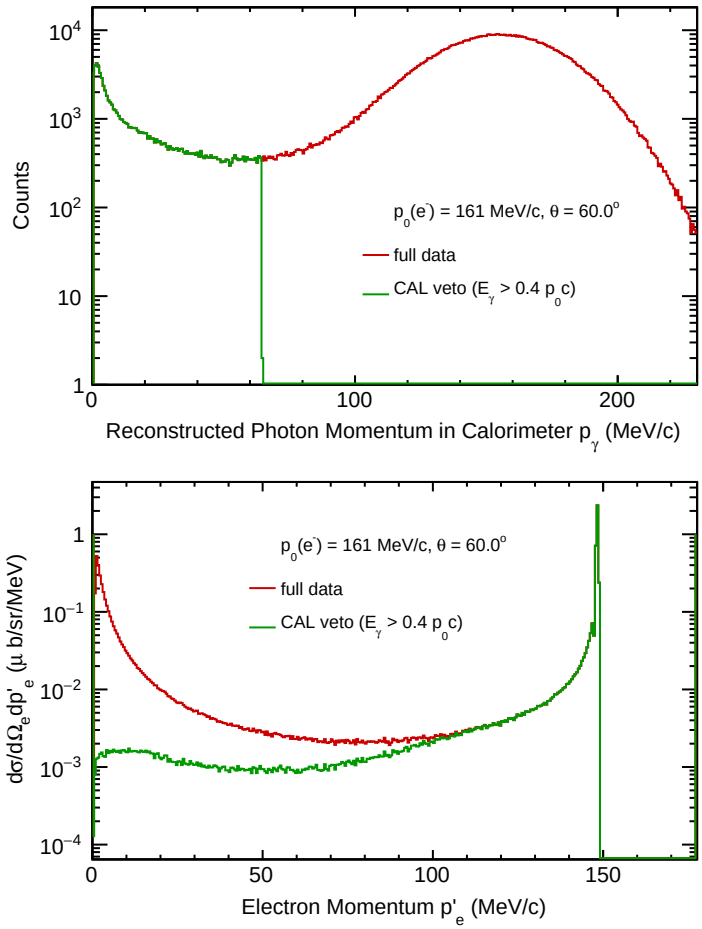

Figure 5.1 ESEPP simulation results for an electron beam momentum of 161 MeV/c and scattering angle of $\theta = 60°$. Top: Simulated bremsstrahlung spectrum within the 8 × 8 calorimeter acceptance and folded with the detector resolution, Eq. (4.8). Bottom: Cross-section distribution before (full) and after initial-state suppression (CAL veto).

Figure 5.2 shows the photon distribution from the ESEPP simulation at the front face of the calorimeter for electrons with 161 MeV/c beam momentum and 60° scat-

[1]Various levels of the photon-energy cut were tested. The choice of 0.4 p_0c results in the overall smallest uncertainty in the radiative corrections of the scattering cross section; see Sec. 5.3.

tering angle. The left panel is the full distribution of photons going forward at the face of the calorimeter. Looking into the beam direction a strongly peaked distribution of photons is seen. After applying the photon energy cut the major part of the distribution is suppressed and only low momentum photons remain in the forward direction. For muons, with the same total number of beam particles, the photons emitted by bremsstrahlung toward the calorimeter acceptance are quite small, there is a negligible difference after applying the cut, as shown in Fig. 5.3.

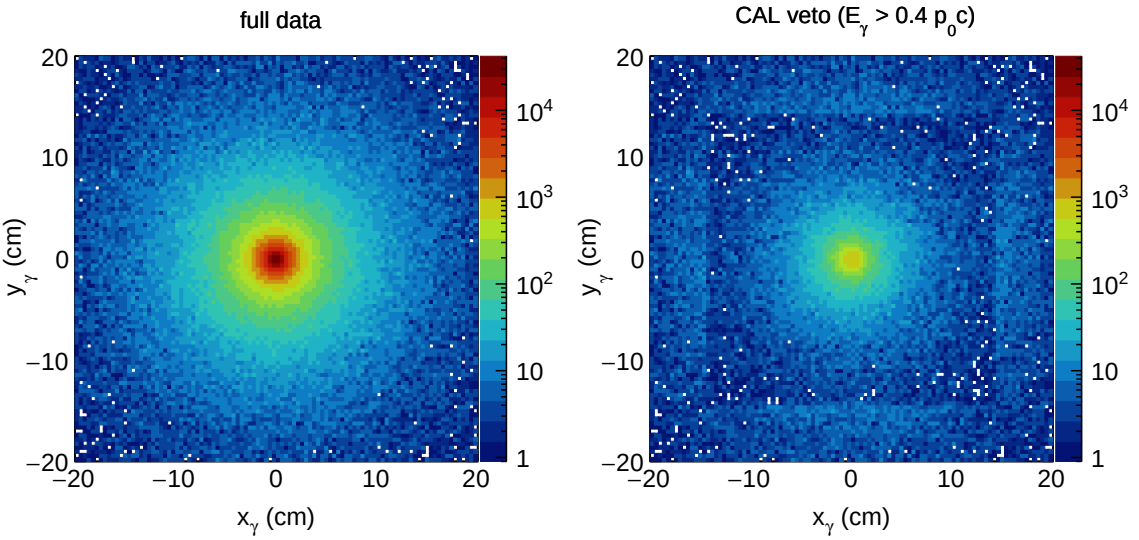

Figure 5.2 Simulated $ep \to ep\gamma$ photon distribution at the front face of the calorimeter with electron beam momentum 161 MeV/c and scattering angle of 60° before (left panel) and after (right panel) 8 × 8 CAL veto.

5.2 Radiative Corrections for $\ell^- p$ scattering data in MUSE Kinematics

The radiative correction δ as a function of the SPS momentum-detection threshold is shown in Fig. 5.4. The red curve shows the results for all scattering events, regardless of the emission of photons at electron beam momentum 161 MeV/c and scattering angle of 60°. It shows a strong dependence on p'_{min} with a steep slope ($> 1\%$ change per MeV/c) close to the SPS detection threshold of 10 MeV/c. If uncontrolled, the

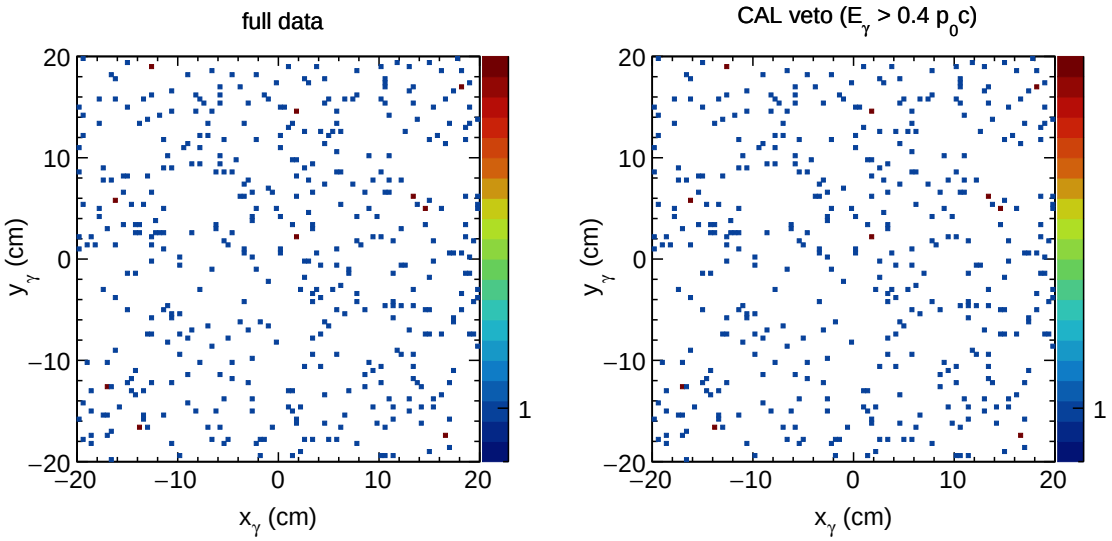

Figure 5.3 Simulated $\mu p \to \mu p \gamma$ photon distribution at the front face of the calorimeter with muon beam momentum 161 MeV/c and scattering angle of 60° before (left panel) and after (right panel) 8 × 8 CAL veto.

uncertainty in $p'_{\min}$ would generate a considerable uncertainty in δ. The simulations reveal that the increase in δ with a decrease in $p'_{\min}$ is linked to the increase of the ep cross-section with reduced beam momentum after the emission of high-energy initial-state radiation. With the calorimeter-veto applied, the green curve in Fig. 5.4 shows the radiative-correction result after suppression of initial-state radiation. By vetoing events with a hit in the calorimeter that have a photon energies above 0.4 p_0c, the radiative correction is smaller and the dependence of the radiative corrections on $p'_{\min}$ is reduced. Radiative corrections for muons are much smaller than for electrons and nearly independent of $p'_{\min}$, as shown in Fig. 5.5. The red curve, which shows the full result, is covered by the green curve. Because there are not many photons emitted from muons in the forward direction, the calorimeter cut does not affect the value of the radiative corrections.

Tables 5.1 and 5.2 give the radiative corrections at three MUSE momenta and three scattering angles. The momentum-thresholds $p'_{\min}$ from Tables 4.1 and 4.2 for SPS discriminator thresholds of $E_{SC1,2} = 2.0$ MeV are used. The calorimeter threshold is at 0.4 p_0c. The radiative corrections increase with increasing scattering angle

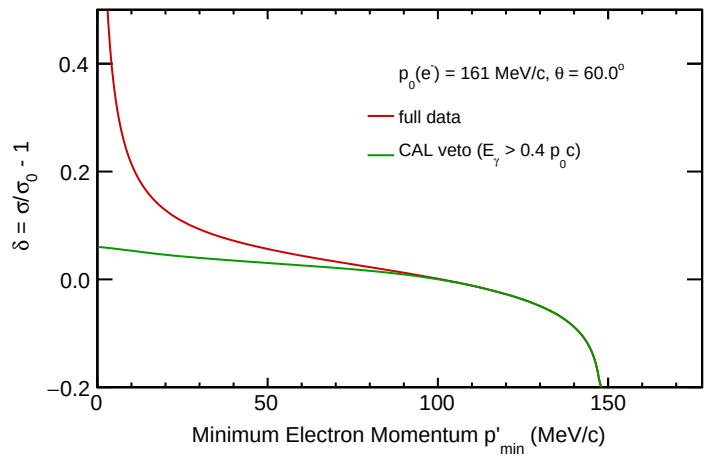

Figure 5.4 The radiative corrections as a function of $p'_{\min}$ for ep scattering at electron beam momentum 161 MeV/c and scattering angle of 60°. The red curve shows the full result without a photon veto. The green curve shows the result after vetoing events with a hit in the calorimeter and photon energy above 0.4 p_0c.

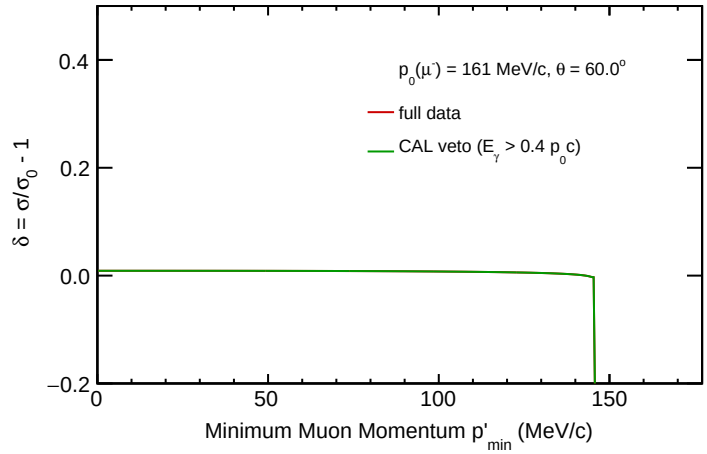

Figure 5.5 The radiative corrections as a function of $p'_{\min}$ for μp scattering at muon beam momentum 161 MeV/c and scattering angle of 60°. The red curve, covered up by the green curve, shows the full result without a photon veto. The green curve shows the result after vetoing events with a hit in the calorimeter and photon energy above 0.4 p_0.

at the same beam momentum and increasing beam momentum at the same scattering angle. A comparison under these conditions is made in the tables: without the calorimeter, with the old calorimeter design (6×6 blocks without the four corners), and with the new calorimeter design (8×8). The values in parentheses are statistical uncertainties. It can be seen that for electrons, the radiative corrections are relatively

larger without the calorimeter. By vetoing the events with a photon energy above the calorimeter threshold, the 6 × 6 design already reduces the values a lot, but the 8 × 8 design reduces the values further. For muons, the radiative corrections are much smaller than for electrons, and vetoing photons does not affect the values. In reality, the energy resolution and efficiency of the calorimeter for photon hits at the outer part of the detector is not as good as for the inner one, so the expected values of the radiative corrections are between those given for the idealized 6 × 6 and 8 × 8 designs.

Table 5.1 Radiative corrections for ep scattering with $E_\gamma > 0.4\ p_0c$.

$\delta(e^-)$		full data	6 × 6	8 × 8
115 MeV/c	25°	0.114(0.0006)	0.032(0.0005)	0.026(0.0005)
	60°	0.143(0.0006)	0.053(0.0006)	0.044(0.0006)
	95°	0.144(0.0006)	0.063(0.0006)	0.055(0.0006)
161 MeV/c	25°	0.163(0.0006)	0.035(0.0006)	0.028(0.0006)
	60°	0.208(0.0007)	0.063(0.0006)	0.052(0.0006)
	95°	0.206(0.0007)	0.076(0.0007)	0.064(0.0007)
210 MeV/c	25°	0.214(0.0007)	0.037(0.0006)	0.030(0.0006)
	60°	0.286(0.0007)	0.072(0.0007)	0.058(0.0007)
	95°	0.283(0.0008)	0.090(0.0007)	0.075(0.0007)

Table 5.2 Radiative corrections for μp scattering with $E_\gamma > 0.4\ p_0c$.

$\delta(\mu^-)$		full data	6 × 6	8 × 8
115 MeV/c	25°	0.001(0.0005)	0.001(0.0005)	0.001(0.0005)
	60°	0.006(0.0005)	0.006(0.0005)	0.006(0.0005)
	95°	0.005(0.0005)	0.005(0.0005)	0.005(0.0005)
161 MeV/c	25°	0.003(0.0005)	0.003(0.0005)	0.003(0.0005)
	60°	0.009(0.0005)	0.009(0.0005)	0.009(0.0005)
	95°	0.008(0.0005)	0.008(0.0005)	0.008(0.0005)
210 MeV/c	25°	0.006(0.0005)	0.006(0.0005)	0.006(0.0005)
	60°	0.011(0.0005)	0.011(0.0005)	0.011(0.0005)
	95°	0.011(0.0005)	0.011(0.0005)	0.011(0.0005)

5.3 Uncertainties of Radiative Corrections from ESEPP Simulation

The uncertainties in the knowledge of the reaction kinematic and detector properties propagate into uncertainties in the radiative corrections. δ is considered to be a function of four independent variables: the minimum lepton momentum $p'_{\min}$, beam momentum p_0, scattering angle θ, and photon energy cut E_γ,

$$\delta = f(X_i) \quad \text{with} \quad X_i = p'_{\min}, p_0, \theta, E_\gamma. \tag{5.1}$$

Assuming that all the variables are uncorrelated and independent of each other, the variance σ_δ is expressed as,

$$\sigma_\delta = \sqrt{\sum_{i=1}^{4} \left(\frac{\partial \delta}{\partial X_i} \right)^2 \sigma_{X_i}^2}, \tag{5.2}$$

where $\frac{\partial \delta}{\partial X_i}$ is the partial derivative of δ at a point x_i of each variable. This can be estimated by a two-point formula, which is known as the symmetric difference quotient,

$$\frac{f(x_i + h) - f(x_i - h)}{2h}. \tag{5.3}$$

It is to compute the slope of a nearby secant line through the points $(x_i - h, f(x_i - h))$ and $(x_i + h, f(x_i + h))$. σ_{X_i} in Eq. (5.2) is the uncertainties of each variable in Table 4.3. The uncertainties of radiative corrections from $p'_{\min}$ for electron scattering at three MUSE momenta and three scattering angles are given in Table 5.3. The SPS momentum-detection thresholds $p'_{\min}$ from Table 4.1 are used for discriminator thresholds of $E_{SC1,2} = 2.0$ MeV, and a photon-energy cut of $E_\gamma > 0.4\ p_0 c$. A comparison is made in Table 5.3 under the conditions: without the calorimeter, with the old calorimeter design (6×6 blocks without the four corners), and with the new calorimeter design (8×8). The values in parentheses are statistical uncertainties. For the full data, without the calorimeter as veto, the uncertainties caused by the uncertainty of $p'_{\min}$ are larger, especially at backward angles (95°) and at higher beam

momenta. By vetoing events with photon energies above the calorimeter threshold, the uncertainties reduce a lot, especially when a larger size of calorimeter (8×8 blocks) is used.

Table 5.3 Contribution to the uncertainties of radiative corrections from $p'_{\min}$ for ep scattering and various photon-calorimeter sizes. Assumed are SPS discriminator thresholds of $E_{SC1,2} = 2.0$ MeV and, for the 6×6 and 8×8 columns, a photon-energy cut of $E_\gamma > 0.4\ p_0 c$.

$\sigma_\delta(e^-)$ (%)		full data	6×6	8×8
115 MeV/c	25°	1.55(0.00)	0.07(0.00)	0.04(0.00)
	60°	2.07(0.01)	0.33(0.00)	0.20(0.00)
	95°	1.97(0.01)	0.50(0.00)	0.38(0.00)
161 MeV/c	25°	2.17(0.00)	0.05(0.00)	0.03(0.00)
	60°	3.01(0.01)	0.29(0.00)	0.16(0.00)
	95°	2.83(0.01)	0.54(0.00)	0.38(0.00)
210 MeV/c	25°	2.86(0.01)	0.04(0.00)	0.02(0.00)
	60°	4.16(0.01)	0.24(0.00)	0.13(0.00)
	95°	3.86(0.01)	0.56(0.00)	0.35(0.00)

Considering all the variables, the total uncertainties of radiative correction can be quantified. Table 5.4 shows the uncertainties of radiative corrections for electrons at three MUSE momenta and three scattering angles. The SPS detection threshold $p'_{\min}$ values are from $E_{SC1,2} = 2.0$ MeV in Tables 4.1 and 4.2. The calorimeter threshold E_γ is determined at $0.4\ p_0 c$ to minimize the uncertainties of the radiative corrections. First, the major contributors to the uncertainty are the uncertainties in the electron detection threshold $p'_{\min}$ and the energy threshold for the identification of hard photons in the calorimeter E_γ. The uncertainties from the scattering angle θ and the beam momentum p_0 are much smaller compared to other variables. Second, $p'_{\min}$ contributions are angular dependent, which means they are relevant for the proton-radius extraction. The uncertainty in E_γ has a large contribution to the total uncertainty of the radiative corrections, but its effect is angular independent.

The uncertainties of radiative corrections for muons are much smaller than for electrons, as shown in Table 5.5. It has been found that the uncertainties for e^+ (μ^+)

Table 5.4 Uncertainties of radiative corrections for electron-proton scattering and using the 8 × 8 calorimeter.

$\sigma_\delta(e^-)$ (%)		$p'_{\min}$	p_0	θ	E_γ	Total
115 MeV/c	25°	0.04(0.00)	0.01(0.02)	0.00(0.00)	0.32(0.00)	0.32(0.00)
	60°	0.20(0.00)	0.00(0.02)	0.00(0.00)	0.33(0.00)	0.39(0.00)
	95°	0.38(0.00)	0.02(0.02)	0.00(0.00)	0.33(0.00)	0.51(0.00)
161 MeV/c	25°	0.03(0.00)	0.00(0.03)	0.00(0.00)	0.24(0.00)	0.24(0.00)
	60°	0.16(0.00)	0.04(0.03)	0.00(0.00)	0.26(0.00)	0.31(0.00)
	95°	0.38(0.00)	0.00(0.03)	0.00(0.00)	0.26(0.00)	0.46(0.00)
210 MeV/c	25°	0.02(0.00)	0.04(0.04)	0.00(0.00)	0.20(0.00)	0.21(0.01)
	60°	0.13(0.00)	0.03(0.04)	0.00(0.00)	0.22(0.00)	0.25(0.00)
	95°	0.35(0.00)	0.01(0.04)	0.00(0.00)	0.22(0.00)	0.41(0.00)

are similar to e^- (μ^-).

Table 5.5 Uncertainties of radiative corrections for muon-proton scattering and using the 8 × 8 calorimeter.

$\sigma_\delta(\mu^-)$ (%)		$p'_{\min}$	p_0	θ	E_γ	Total
115 MeV/c	25°	0.00(0.00)	0.00(0.02)	0.00(0.02)	0.00(0.00)	0.00(0.00)
	60°	0.01(0.00)	0.01(0.01)	0.00(0.00)	0.00(0.00)	0.01(0.01)
	95°	0.04(0.00)	0.00(0.01)	0.00(0.00)	0.00(0.00)	0.04(0.01)
161 MeV/c	25°	0.00(0.00)	0.00(0.02)	0.00(0.00)	0.00(0.00)	0.00(0.02)
	60°	0.00(0.00)	0.02(0.02)	0.00(0.00)	0.00(0.00)	0.02(0.02)
	95°	0.02(0.00)	0.04(0.02)	0.00(0.00)	0.00(0.00)	0.04(0.02)
210 MeV/c	25°	0.00(0.00)	0.01(0.03)	0.00(0.00)	0.00(0.00)	0.01(0.03)
	60°	0.00(0.00)	0.01(0.03)	0.00(0.00)	0.00(0.00)	0.01(0.03)
	95°	0.01(0.00)	0.02(0.03)	0.00(0.00)	0.00(0.00)	0.02(0.02)

5.4 Cross Section Asymmetries

The cross section asymmetry is defined as,

$$A = \frac{\sigma_{\ell^+} - \sigma_{\ell^-}}{\sigma_{\ell^+} + \sigma_{\ell^-}}. \tag{5.4}$$

Figure 5.6 shows the cross section asymmetries as a function of the lepton energy loss ΔE for electrons and muons from the ESEPP event generator at a beam momentum of 161 MeV/c using the 8 × 8 calorimeter. In this simulation, the Mo and Tsai definition

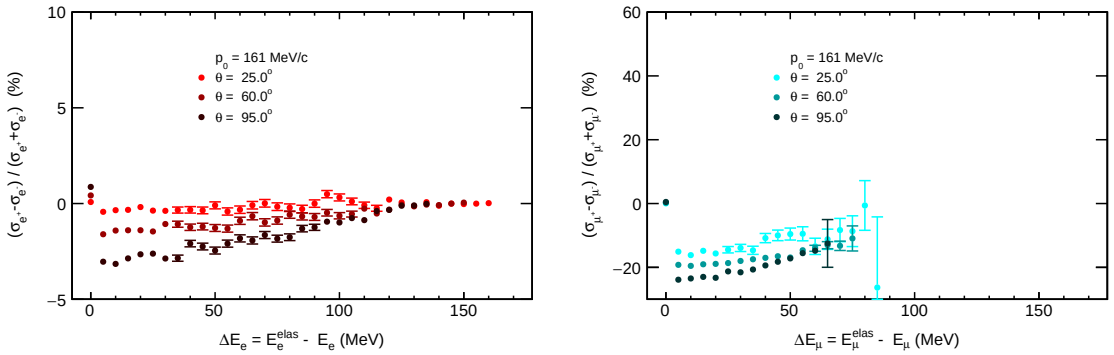

Figure 5.6 Cross-section asymmetries as a function of ΔE for electrons (left panel) and muons (right panel) at beam momentum 161 MeV/c for 8×8 calorimeter.

of soft TPE was used. The statistical uncertainties are shown as error bars. The data points show an asymmetry that varies over the scattered lepton energy at various scattering angles. For electrons, the cross-section asymmetry is positive in the elastic peak, negative in the radiative tail, and the magnitude is decreasing with increasing energy loss, which means the photon is harder. The TPE effect is larger at backward angles than at forward angles. For muons, it shows a similar pattern with significantly larger asymmetries. MUSE does not measure the momentum of the outgoing lepton, therefore cannot determine the ΔE as the plot shows. MUSE measures the integrated cross section from detection threshold p'_{min} to the endpoint. The asymmetries A for the integrated cross sections as a function of p'_{min} with beam momentum 161 MeV/c and various scattering angles are shown in Fig. 5.7. The asymmetries decrease with decreasing p'_{min} and with decreasing Q^2. They are higher for the lighter lepton. These results are consistent with the findings in Ref. [67].

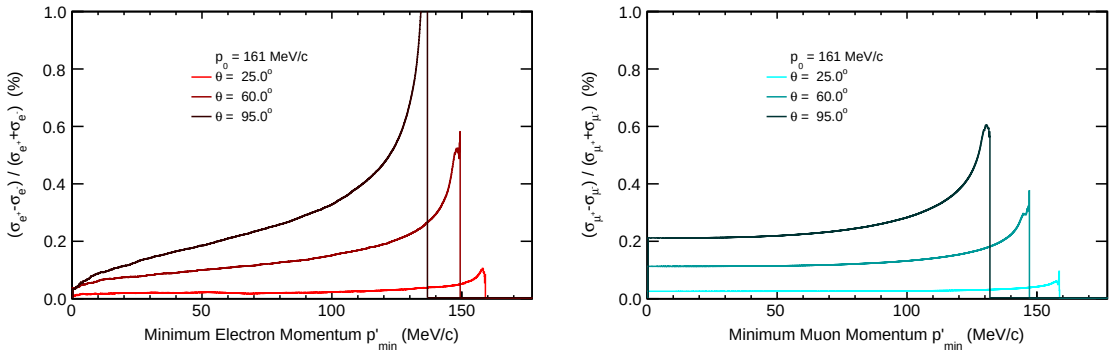

Figure 5.7 Cross-section asymmetries of the integrated cross section as a function of p'_{min} for electrons (left panel) and muons (right panel) at beam momentum 161 MeV/c for 8×8 calorimeter.

Chapter 6

Summary and Outlook

The MUSE experiment intends to extract the proton charge radius from both elastic electron-proton and muon-proton scattering data with high precision. The experiment will also directly compare electron and muon scattering in the same experiment, and test two-photon exchange effects with positively and negatively charged beams. MUSE uses the scattered-particle-scintillators detector as trigger detector that covers a large angular range. Without knowing the final-state lepton momentum precisely, the cross section for each scattering angle is obtained from the integration from the SPS detection threshold to the momentum endpoint in the experiment. Radiative corrections, especially the initial-state Bremsstrahlung effect with the emission of a hard photon, plays an important role in the proton radius extraction. The uncertainties of the radiative corrections caused by the uncertainties in the experimental inputs are a large part in the systematic uncertainties of MUSE. This work demonstrates the need of using a photon detector downstream of the target to suppress initial-state radiation effects.

As the trigger detector, the particle detection efficiency of the SPS detector needs to be as high as possible. From Geant4 simulation, the discrimination threshold of 2 MeV for the light output at the PMTs will achieve a high SPS efficiency. This discrimination threshold determines the momentum threshold $p'_{\min}$ of detecting electrons and muons. This threshold varies with the particle scattering angle.

Furthermore, different physics models and event generators of radiative correction are compared. The differences between different models are caused by including

different Feynman diagrams and calculation methods. These model uncertainties are much more significant than the error caused by the higher-order radiative correction effects. The ESEPP event generator which meets the requirement for the MUSE experiment was used to study the radiative correction.

Finally, with the knowledge of the SPS detection threshold, the beam momentum, the scattering angle, and the photon calorimeter, the ESEPP simulations show the radiative corrections to the Born cross section are below 0.1 for electron and 0.01 for muon in an 8×8 crystal calorimeter design. The uncertainties of the radiative corrections from the uncertainties in the experimental inputs for electron scattering are lower than 0.5%, while uncertainties related to the proton radius extraction for electrons are lower than 0.38%. The total uncertainties of the radiative corrections from the uncertainties in the experimental input for muons are less than 0.05%. The uncertainties for e^+ (μ^+) is similar to e^- (μ^-) within statistical uncertainties.

This work is based on the ESEPP event generator starting at the target. The situation is much more complicated when considering the processes where the incident and scattered particles pass through the upstream detectors, the vacuum chamber and the air gaps. In further study, first, a full Geant4 simulation of the experiment with an event generator needs to be implemented to study the full radiative correction effect. In the experiment, the total beam particles are 10^{14} over 12 months of data collection at a beam flux of 3 MHz. To control the statistical uncertainty, there are even more particles that need to be simulated in the Geant4 simulation, which is a big challenge. It is necessary to improve the event sampling to more efficiently cover the full angular acceptance of the MUSE setup. Second, MUSE simulations with input from other event generators are also planned to test model uncertainty. Third, the uncertainties of radiative corrections are heavily dependent on the detector properties and their variances. A better understanding of these from simulation and experimental data will improve the systematic uncertainties in the MUSE experiment.

The commissioning of MUSE has been almost completed. In the Fall of 2021, initial production data were taken at 115 MeV/c beam momentum. As for additional beam time, it is expected to be taken in the second half of 2022 and beyond. With the systematic uncertainties under control, MUSE is capable to measure the proton charge radius with high precision, study possible 2γ mechanisms, and have a direct μ/e comparison of the elastic cross sections.

Bibliography

[1] E. Rutherford. "The scattering of alpha and beta particles by matter and the structure of the atom". In: *Phil. Mag. Ser. 6* 21 (1911), pp. 669–688. DOI: 10.1080/14786440508637080.

[2] M. N. Rosenbluth. "High Energy Elastic Scattering of Electrons on Protons". In: *Phys. Rev.* 79 (1950), pp. 615–619. DOI: 10.1103/PhysRev.79.615.

[3] Michael I. Eides, Howard Grotch, and Valery A. Shelyuto. "Theory of light hydrogen - like atoms". In: *Phys. Rept.* 342 (2001), pp. 63–261. DOI: 10.1016/S0370-1573(00)00077-6. arXiv: hep-ph/0002158.

[4] Robert Karplus, Abraham Klein, and Julian Schwinger. "Electrodynamic Displacement of Atomic Energy Levels. 2. Lamb Shift". In: *Phys. Rev.* 86 (1952), pp. 288–301. DOI: 10.1103/PhysRev.86.288.

[5] J. C. Bernauer et al. "High-precision determination of the electric and magnetic form factors of the proton". In: *Phys. Rev. Lett.* 105 (2010), p. 242001. DOI: 10.1103/PhysRevLett.105.242001. arXiv: 1007.5076 [nucl-ex].

[6] Peter J. Mohr, Barry N. Taylor, and David B. Newell. "CODATA Recommended Values of the Fundamental Physical Constants: 2010". In: *Rev. Mod. Phys.* 84 (2012), pp. 1527–1605. DOI: 10.1103/RevModPhys.84.1527. arXiv: 1203.5425 [physics.atom-ph].

[7] Randolf Pohl et al. "The size of the proton". In: *Nature* 466 (2010), pp. 213–216. DOI: 10.1038/nature09250.

[8] Aldo Antognini et al. “Proton Structure from the Measurement of $2S - 2P$ Transition Frequencies of Muonic Hydrogen”. In: *Science* 339 (2013), pp. 417–420. DOI: 10.1126/science.1230016.

[9] Gerald A. Miller. “Defining the proton radius: A unified treatment”. In: *Phys. Rev. C* 99.3 (2019), p. 035202. DOI: 10.1103/PhysRevC.99.035202. arXiv: 1812.02714 [nucl-th].

[10] Randolf Pohl et al. “Muonic hydrogen and the proton radius puzzle”. In: *Ann. Rev. Nucl. Part. Sci.* 63 (2013), pp. 175–204. DOI: 10.1146/annurev-nucl-102212-170627. arXiv: 1301.0905 [physics.atom-ph].

[11] Carl E. Carlson. “The Proton Radius Puzzle”. In: *Prog. Part. Nucl. Phys.* 82 (2015), pp. 59–77. DOI: 10.1016/j.ppnp.2015.01.002. arXiv: 1502.05314 [hep-ph].

[12] David W Hertzog and William M Morse. “The Brookhaven muon anomalous magnetic moment experiment”. In: *Annu. Rev. Nucl. Part. Sci.* 54 (2004), pp. 141–174.

[13] G. W. Bennett et al. “Final Report of the Muon E821 Anomalous Magnetic Moment Measurement at BNL”. In: *Phys. Rev. D* 73 (2006), p. 072003. DOI: 10.1103/PhysRevD.73.072003. arXiv: hep-ex/0602035.

[14] Fred Jegerlehner and Andreas Nyffeler. “The Muon g-2”. In: *Phys. Rept.* 477 (2009), pp. 1–110. DOI: 10.1016/j.physrep.2009.04.003. arXiv: 0902.3360 [hep-ph].

[15] Vernon Barger et al. “Constraint on parity-violating muonic forces”. In: *Phys. Rev. Lett.* 108 (2012), p. 081802. DOI: 10.1103/PhysRevLett.108.081802. arXiv: 1109.6652 [hep-ph].

[16] Savely G. Karshenboim, David McKeen, and Maxim Pospelov. "Constraints on muon-specific dark forces". In: *Phys. Rev. D* 90.7 (2014). [Addendum: Phys.Rev.D 90, 079905 (2014)], p. 073004. DOI: 10.1103/PhysRevD.90.073004. arXiv: 1401.6154 [hep-ph].

[17] J. Insler et al. "Search for the Decay $J/\psi \to \gamma$ + invisible". In: *Phys. Rev. D* 81 (2010), p. 091101. DOI: 10.1103/PhysRevD.81.091101. arXiv: 1003.0417 [hep-ex].

[18] Vernon Barger et al. "Proton size anomaly". In: *Phys. Rev. Lett.* 106 (2011), p. 153001. DOI: 10.1103/PhysRevLett.106.153001. arXiv: 1011.3519 [hep-ph].

[19] Axel Beyer et al. "The Rydberg constant and proton size from atomic hydrogen". In: *Science* 358.6359 (2017), pp. 79–85.

[20] N. Bezginov et al. "A measurement of the atomic hydrogen Lamb shift and the proton charge radius". In: *Science* 365.6457 (2019), pp. 1007–1012. DOI: 10.1126/science.aau7807.

[21] Hélène Fleurbaey et al. "New Measurement of the $1S-3S$ Transition Frequency of Hydrogen: Contribution to the Proton Charge Radius Puzzle". In: *Phys. Rev. Lett.* 120.18 (2018), p. 183001. DOI: 10.1103/PhysRevLett.120.183001. arXiv: 1801.08816 [physics.atom-ph].

[22] W. Xiong et al. "A small proton charge radius from an electron–proton scattering experiment". In: *Nature* 575.7781 (2019), pp. 147–150. DOI: 10.1038/s41586-019-1721-2.

[23] M. Mihovilovič et al. "The proton charge radius extracted from the initial-state radiation experiment at MAMI". In: *Eur. Phys. J. A* 57.3 (2021), p. 107. DOI: 10.1140/epja/s10050-021-00414-x. arXiv: 1905.11182 [nucl-ex].

[24] H. Atac et al. "Charge radii of the nucleon from its flavor dependent Dirac form factors". In: *Eur. Phys. J. A* 57.2 (2021), p. 65. DOI: 10.1140/epja/s10050-021-00389-9. arXiv: 2009.04357 [nucl-ex].

[25] Alexander V. Gramolin and Rebecca L. Russell. "Transverse charge density and the radius of the proton". In: *Phys. Rev. D* 105.5 (2022), p. 054004. DOI: 10.1103/PhysRevD.105.054004. arXiv: 2102.13022 [nucl-ex].

[26] X. Zhan et al. "High-Precision Measurement of the Proton Elastic Form Factor Ratio $\mu_p G_E/G_M$ at low Q^2". In: *Phys. Lett. B* 705 (2011), pp. 59–64. DOI: 10.1016/j.physletb.2011.10.002. arXiv: 1102.0318 [nucl-ex].

[27] Alexey Grinin et al. "Two-photon frequency comb spectroscopy of atomic hydrogen". In: *Science* 370.6520 (2020), pp. 1061–1066.

[28] T. Suda et al. "Measurement of Proton Charge Radius by Low-Energy Electron Scattering". In: *J. Particle Accelerator Society of Japan* 15 (2018), pp. 52–59.

[29] Christian Dreisbach et al. "Measuring the Proton Radius in High-Energy Muon-Proton Scattering". In: *PoS* DIS2019 (2019), p. 222. DOI: 10.22323/1.352.0222.

[30] A. Vorobyev. "Precision measurement of the proton charge radius in electron proton scattering". In: *Phys. Part. Nucl. Lett.* 16.5 (2019), pp. 524–529. DOI: 10.1134/S1547477119050303. arXiv: 1905.03181 [nucl-ex].

[31] A. Gasparian et al. "PRad-II: A New Upgraded High Precision Measurement of the Proton Charge Radius". In: (Sept. 2020). arXiv: 2009.10510 [nucl-ex].

[32] R. Gilman et al. "Technical Design Report for the Paul Scherrer Institute Experiment R-12-01.1: Studying the Proton "Radius" Puzzle with μp Elastic Scattering". In: (Sept. 2017). arXiv: 1709.09753 [physics.ins-det].

[33] Ethan Cline et al. "MUSE: The MUon Scattering Experiment". In: *SciPost Phys. Proc.* 5 (2021), p. 023. DOI: 10.21468/SciPostPhysProc.5.023.

[34] J. Arrington, P. G. Blunden, and W. Melnitchouk. "Review of two-photon exchange in electron scattering". In: *Prog. Part. Nucl. Phys.* 66 (2011), pp. 782–833. DOI: 10.1016/j.ppnp.2011.07.003. arXiv: 1105.0951 [nucl-th].

[35] A. Afanasev et al. "Two-photon exchange in elastic electron–proton scattering". In: *Prog. Part. Nucl. Phys.* 95 (2017), pp. 245–278. DOI: 10.1016/j.ppnp.2017.03.004. arXiv: 1703.03874 [nucl-ex].

[36] Julian S. Schwinger. "Quantum electrodynamics. III: The electromagnetic properties of the electron: Radiative corrections to scattering". In: *Phys. Rev.* 76 (1949). Ed. by K. A. Milton, pp. 790–817. DOI: 10.1103/PhysRev.76.790.

[37] Yung-Su Tsai. "Radiative Corrections to Electron-Proton Scattering". In: *Phys. Rev.* 122 (1961), pp. 1898–1907. DOI: 10.1103/PhysRev.122.1898.

[38] Luke W. Mo and Yung-Su Tsai. "Radiative Corrections to Elastic and Inelastic e p and mu p Scattering". In: *Rev. Mod. Phys.* 41 (1969), pp. 205–235. DOI: 10.1103/RevModPhys.41.205.

[39] L. C. Maximon and J. A. Tjon. "Radiative corrections to electron proton scattering". In: *Phys. Rev. C* 62 (2000), p. 054320. DOI: 10.1103/PhysRevC.62.054320. arXiv: nucl-th/0002058.

[40] M. Vanderhaeghen et al. "QED radiative corrections to virtual Compton scattering". In: *Phys. Rev. C* 62 (2000), p. 025501. DOI: 10.1103/PhysRevC.62.025501. arXiv: hep-ph/0001100.

[41] Pulak Talukdar et al. "Radiative and chiral corrections to elastic lepton-proton scattering in chiral perturbation theory". In: *Phys. Rev. D* 104.5 (2021), p. 053001. DOI: 10.1103/PhysRevD.104.053001. arXiv: 2010.09380 [nucl-th].

[42] Pulak Banerjee et al. "QED at NNLO with McMule". In: *SciPost Phys.* 9 (2020), p. 027. DOI: 10.21468/SciPostPhys.9.2.027. arXiv: 2007.01654 [hep-ph].

[43] A. V. Gramolin et al. “A new event generator for the elastic scattering of charged leptons on protons”. In: *J. Phys. G* 41.11 (2014), p. 115001. DOI: 10.1088/0954-3899/41/11/115001. arXiv: 1401.2959 [nucl-ex].

[44] Axel Schmidt. “Measuring the lepton sign asymmetry in elastic electron-proton scattering with OLYMPUS”. PhD thesis. MIT, 2016. arXiv: 1711.09894 [nucl-ex].

[45] Andrei Afanasev. *Comparing electron and muon scattering for MUSE*. MUSE Collaboration Meeting. 2019.

[46] J. Grillenberger, C. Baumgarten, and M. Seidel. “The High Intensity Proton Accelerator Facility”. In: *SciPost Phys. Proc.* (5 2021), p. 2. DOI: 10.21468/SciPostPhysProc.5.002. URL: https://scipost.org/10.21468/SciPostPhysProc.5.002.

[47] E. Cline et al. “Characterization of muon and electron beams in the Paul Scherrer Institute PiM1 channel for the MUSE experiment”. In: *Phys. Rev. C* 105.5 (2022), p. 055201. DOI: 10.1103/PhysRevC.105.055201. arXiv: 2109.09508 [physics.ins-det].

[48] Ethan Cline. “Understanding the Paul Scherrer Institute’s PiM1 beamline for MUSE”. PhD thesis. Rutgers, The State University of New Jersey, 2019.

[49] Tigran Rostomyan et al. “Timing detectors with SiPM read-out for the MUSE experiment at PSI”. In: *Nucl. Instrum. Meth. A* 986 (2021), p. 164801. DOI: 10.1016/j.nima.2020.164801. arXiv: 2007.12207 [physics.ins-det].

[50] J. Allison et al. “Recent developments in Geant4”. In: *Nuclear Instruments and Methods in Physics Research Section A: Accelerators, Spectrometers, Detectors and Associated Equipment* 835 (2016), pp. 186–225. ISSN: 0168-9002. DOI: https://doi.org/10.1016/j.nima.2016.06.125. URL: https://www.sciencedirect.com/science/article/pii/S0168900216306957.

[51] R. Milner et al. “The OLYMPUS Experiment”. In: *Nucl. Instrum. Meth. A* 741 (2014), pp. 1–17. DOI: 10.1016/j.nima.2013.12.035. arXiv: 1312.1730 [physics.ins-det].

[52] J. A. Appel et al. “Performance of a Lead Glass Electromagnetic Shower Detector at Fermilab”. In: *Nucl. Instrum. Meth.* 127 (1975), p. 495. DOI: 10.1016/0029-554X(75)90653-9.

[53] P. Roy et al. “A Liquid Hydrogen Target for the MUSE Experiment at PSI”. In: *Nucl. Instrum. Meth. A* 949 (2020), p. 162874. DOI: 10.1016/j.nima.2019.162874. arXiv: 1907.03022 [physics.ins-det].

[54] M. F. M. Lutz et al. “Physics Performance Report for PANDA: Strong Interaction Studies with Antiprotons”. In: (Mar. 2009). arXiv: 0903.3905 [hep-ex].

[55] D. S. Carman et al. “The CLAS12 Forward Time-of-Flight system”. In: *Nucl. Instrum. Meth. A* 960 (2020), p. 163629. DOI: 10.1016/j.nima.2020.163629.

[56] Anne Flannery. *Calibration of Scintillators for MUon Scattering Experiment*. in preparation. 2022.

[57] F. Halzen and Alan D. Martin. *Quarks and Leptons: An Introductory Course In Modern Particle Physics*. 1984. ISBN: 978-0-471-88741-6.

[58] R. G. Sachs. “High-Energy Behavior of Nucleon Electromagnetic Form Factors”. In: *Phys. Rev.* 126 (1962), pp. 2256–2260. DOI: 10.1103/PhysRev.126.2256.

[59] B. M. Preedom and R. Tegen. “Nucleon electromagnetic form factors from scattering of polarized muons or electrons”. In: *Phys. Rev. C* 36 (1987), pp. 2466–2472. DOI: 10.1103/PhysRevC.36.2466.

[60] Pulak Talukdar, Fred Myhrer, and Udit Raha. “Low-Energy Effective Field Theory of Lepton-Proton Bremsstrahlung”. In: (Dec. 2017). arXiv: 1712.09963 [nucl-th].

[61] A. V. Afanasev et al. "ELRADGEN: Monte Carlo generator for radiative events in elastic electron proton scattering". In: *Czech. J. Phys.* 53 (2003). Ed. by M. Finger et al., B449–B454. DOI: 10.1023/A:1024699907910. arXiv: hep-ph/0308106.

[62] D. Yu. Bardin and N. M. Shumeiko. "An Exact Calculation of the Lowest Order Electromagnetic Correction to the Elastic Scattering". In: *Nucl. Phys. B* 127 (1977), pp. 242–258. DOI: 10.1016/0550-3213(77)90213-9.

[63] A. Afanasev, I. Akushevich, and N. Merenkov. "Model independent radiative corrections in processes of polarized electron nucleon elastic scattering". In: *Phys. Rev. D* 64 (2001), p. 113009. DOI: 10.1103/PhysRevD.64.113009. arXiv: hep-ph/0102086.

[64] I. Akushevich et al. "Monte Carlo Generator ELRADGEN 2.0 for Simulation of Radiative events in Elastic *ep*-Scattering of Polarized Particles". In: *Comput. Phys. Commun.* 183 (2012), pp. 1448–1467. DOI: 10.1016/j.cpc.2012.01.015. arXiv: 1104.0039 [hep-ph].

[65] A. Afanasev and A. Ilyichev. "Radiative corrections to the lepton current in unpolarized elastic *lp*-interaction for fixed Q^2 and scattering angle". In: *Eur. Phys. J. A* 57.9 (2021), p. 280. DOI: 10.1140/epja/s10050-021-00582-w. arXiv: 2106.11103 [hep-ph].

[66] O. Koshchii and A. Afanasev. "Charge asymmetry in elastic scattering of massive leptons on protons". In: *Phys. Rev. D* 96.1 (2017), p. 016005. DOI: 10.1103/PhysRevD.96.016005. arXiv: 1705.00338 [nucl-th].

[67] Andrei Afanasev and Alexander Ilyichev. "Contribution of hard photon emission to the charge asymmetry in elastic lepton- and antilepton-proton scattering". In: *Phys. Rev. D* 105.1 (2022), p. L011301. DOI: 10.1103/PhysRevD.105.L011301. arXiv: 2007.02087 [hep-ph].

[68] Jan C. Bernauer. "Measurement of the elastic electron-proton cross section and separation of the electric and magnetic form factor in the Q^2 range from 0.004 to 1 $(GeV/c)^2$". PhD thesis. Mainz U., Inst. Kernphys., 2010.

[69] Rebecca L. Russell. "A Measurement of the Two-Photon Exchange Effect in Elastic Electron-Proton Scattering with OLYMPUS". PhD thesis. MIT, 2016.

[70] Stefan Scherer. "Introduction to chiral perturbation theory". In: *Adv. Nucl. Phys.* 27 (2003). Ed. by John W. Negele and E. W. Vogt, p. 277. arXiv: hep-ph/0210398.

[71] D. R. Yennie, Steven C. Frautschi, and H. Suura. "The infrared divergence phenomena and high-energy processes". In: *Annals Phys.* 13 (1961), pp. 379–452. DOI: 10.1016/0003-4916(61)90151-8.

[72] V. Bernard, Norbert Kaiser, and Ulf-G. Meissner. "Chiral dynamics in nucleons and nuclei". In: *Int. J. Mod. Phys. E* 4 (1995), pp. 193–346. DOI: 10.1142/S0218301395000092. arXiv: hep-ph/9501384.

[73] Pulak Talukdar et al. "Low-Energy Lepton-Proton Bremsstrahlung via Effective Field Theory". In: *Eur. Phys. J. A* 54.11 (2018), p. 195. DOI: 10.1140/epja/i2018-12629-8. arXiv: 1810.04027 [nucl-th].

[74] Pulak Talukdar et al. "Lepton-Proton Two-Photon Exchange in Chiral Perturbation Theory". In: *Phys. Rev. D* 101.1 (2020), p. 013008. DOI: 10.1103/PhysRevD.101.013008. arXiv: 1911.06843 [nucl-th].

[75] Pulak Talukdar. private communication.

[76] Yannick Ulrich. "McMule – QED Corrections for Low-Energy Experiments". Other thesis. Aug. 2020. arXiv: 2008.09383 [hep-ph].

[77] Yannick Ulrich. private communication.

[78] Matteo Fael and Massimo Passera. "Muon-Electron Scattering at Next-To-Next-To-Leading Order: The Hadronic Corrections". In: *Phys. Rev. Lett.* 122.19 (2019), p. 192001. DOI: 10.1103/PhysRevLett.122.192001. arXiv: 1901.03106 [hep-ph].

[79] Florian Weissbach et al. "Improved radiative corrections to $(e, e'p)$ experiments: Explicit treatment of kinematical corrections in multiphoton bremsstrahlung". In: *Phys. Rev. C* 80 (2009), p. 024602. DOI: 10.1103/PhysRevC.80.024602. arXiv: 0805.1535 [nucl-th].

[80] A. B. Arbuzov and T. V. Kopylova. "On higher order radiative corrections to elastic electron–proton scattering". In: *Eur. Phys. J. C* 75.12 (2015), p. 603. DOI: 10.1140/epjc/s10052-015-3833-7. arXiv: 1510.06497 [hep-ph].

[81] R. D. Bucoveanu and H. Spiesberger. "Second-Order Leptonic Radiative Corrections for Lepton-Proton Scattering". In: *Eur. Phys. J. A* 55.4 (2019), p. 57. DOI: 10.1140/epja/i2019-12727-1. arXiv: 1811.04970 [hep-ph].

[82] Richard J. Hill. "Effective field theory for large logarithms in radiative corrections to electron proton scattering". In: *Phys. Rev. D* 95.1 (2017), p. 013001. DOI: 10.1103/PhysRevD.95.013001. arXiv: 1605.02613 [hep-ph].

[83] P.A. Zyla et al. "Review of Particle Physics". In: *PTEP* 2020.8 (2020), p. 083C01. DOI: 10.1093/ptep/ptaa104.

[84] G. Dietze and H. Klein. "Gamma-calibration of NE 213 scintillation counters". In: *Nuclear Instruments and Methods in Physics Research* 193.3 (1982), pp. 549–556. ISSN: 0167-5087. DOI: https://doi.org/10.1016/0029-554X(82)90249-X. URL: https://www.sciencedirect.com/science/article/pii/0029554X8290249X.

[85] ELJEN Technology. *GENERAL PURPOSE EJ-200, EJ-204, EJ-208, EJ-212*. URL: https://eljentechnology.com/products/plastic-scintillators/ej-200-ej-204-ej-208-ej-212.

[86] Win Lin et al. *Timing Detectors & Calorimeter (Part 1)*. Paul Scherrer Institute BVR 53 private communication. 2022.

[87] Ralf Gothe. private communication.

Appendix A

SPS Construction and Time Resolution Measurement

SPS Construction

There are two types of scintillation bars for the SPS detector in the MUSE experiment. The front wall has shorter bars that are 120 cm long and with a rectangular cross section of 6 cm $\times$ 3 cm. The rear wall has longer bars, 220 cm long and with a square cross section of 6 cm $\times$ 6 cm. Construction and characterizing of the SPS detectors followed largely the procedures and methods of Ref. [55]. The plastic scintillators were first inspected visually to record any defects. For the long bars, each end was fitted with black tape, which masks the corners while leaving a circular window. Then the scintillators were loaded onto the curing windmill, which held the bars vertically. The PMT was glued to the center of the upward-facing end of the scintillator (Fig. A.1 top left panel). A centering tool was used so that the glue can cure while the assembly was held upright. The centering tool was removed and the scintillator was rotated 180° after twenty-four hours. The second PMT was glued on the other end with the same process. All the PMTs were tested with a ^{90}Sr source for signal and high-voltage (HV) requirements before the assembly. After removing from the windmill, the bars were wrapped first with precision-cut aluminized Mylar (Fig. A.1 top right panel) and then Tedlar (Fig. A.1 bottom left panel). The Tedlar film extended beyond each PMT onto the anode, dynode, and HV cables, providing a single light-tight encasing for the entire counter. After the assembly, six bars were stacked together on the table

to perform six-bar cosmic ray resolution measurement (Fig. A.1 bottom right panel with three short and three long bars in the stack).

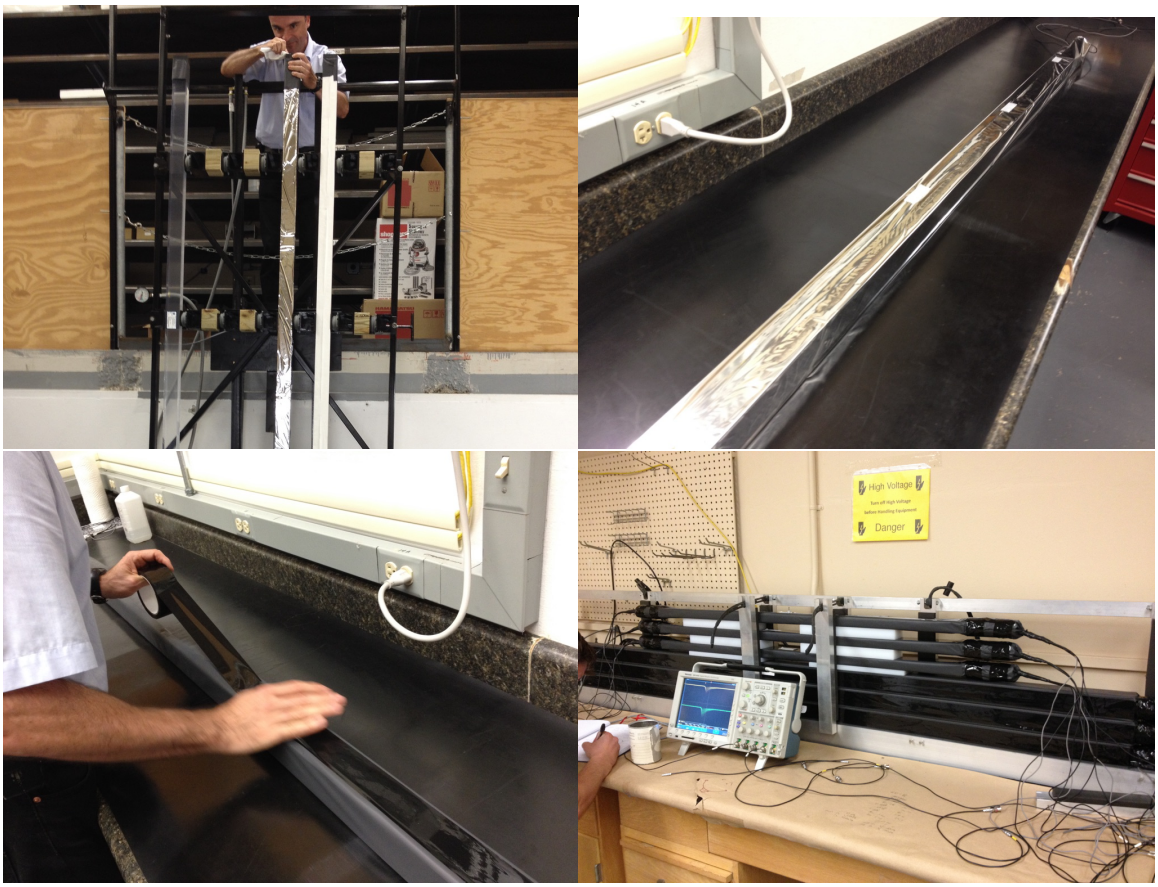

Figure A.1 Top left: Glue PMTs on both ends of the plastic scintillator. Top right: Wrap with precision-cut aluminized mylar. Bottom left: Wrap with Tedlar film and extend beyond PMT, covering the anode, dynode and high-voltage cables. Bottom right: Six bars were stacked together to test and measure the time resolution.

Time Resolution

To find out the time resolution of a scintillator bar, one method called the six-bar cosmic-ray method, which is a generalization and improvement on the three-bar cosmic-ray method, is used in this measurement [87]. The three-bar cosmic-ray method allows the determination of the average time resolution of three identical counters. It proceeds by stacking the three identical counters vertically with equal spacing between adjacent counters and each counter being parallel to the other two,

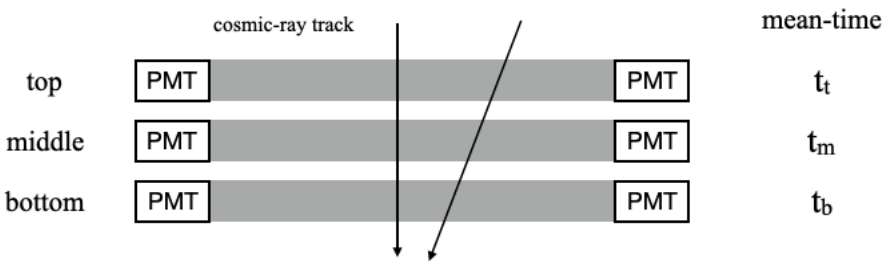

Figure A.2 A schematic view of the three-bar cosmic-ray method used to determine the counter's time resolution.

see Fig. A.2. When the cosmic-ray events that go through all three counters are considered, the equal spacing and the straight trajectory of the cosmic-ray particle ensure that the mean-time difference $T_{t,m,b}$, which is defined as

$$T_{t,m,b} = \frac{t_t + t_b}{2} - t_m, \tag{A.1}$$

is independent of the path traveled, and this value allows the determination of the average time resolution of the three identical counters. t_t, t_m and t_b are the times that the particle goes through the top, middle and bottom counters, respectively. When applying error propagation, the time resolution is

$$\sigma^2_{T_{t,m,b}} = \frac{\sigma_t^2 + \sigma_b^2}{4} + \sigma_m^2, \tag{A.2}$$

where the $\sigma^2_{T_{t,m,b}}$ is the variance measured from TDC channels. Figure A.3 shows one example of mean-time difference from TDC value in the time resolution measurement. The measured standard deviation is about 60 ps. If all bars have the same performance, $\sigma_t = \sigma_b = \sigma_m$, the resolution of the mean time for a given bar is $\sqrt{\frac{2}{3}}\sigma_{T_{t,m,b}}$; here 49 ps.

If the number of counters stacked together extends to six, similar to the three-bar method, there are six possible combinations of three-bar sets in which the spacing between adjacent counters is the same. Then there are six observables, allowing for the determination of the individual time resolutions of each of the six detectors. There is still one problem with this method. In the set of six equations, the inner two counters

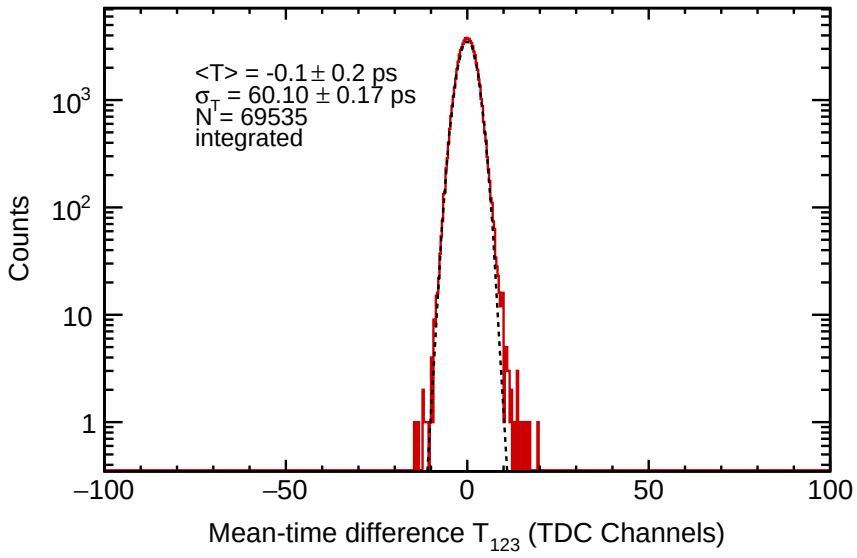

Figure A.3 Example of a mean-time difference, Eq. (A.1), for three long SPS detectors in the top, middle, and bottom positions. The standard deviation σ_T is not the time-resolution of a single bar; see text.

appear four times, whereas the outer two only involve two times. This causes some counters to have a larger fluctuation in the time resolution result. The way to modify it is exchanging the position of some counters to get the so-called complementary ordering as shown in Fig. A.4. This ordering guarantees that each counter has the same influence on the time resolution calculation. With the measurements from the

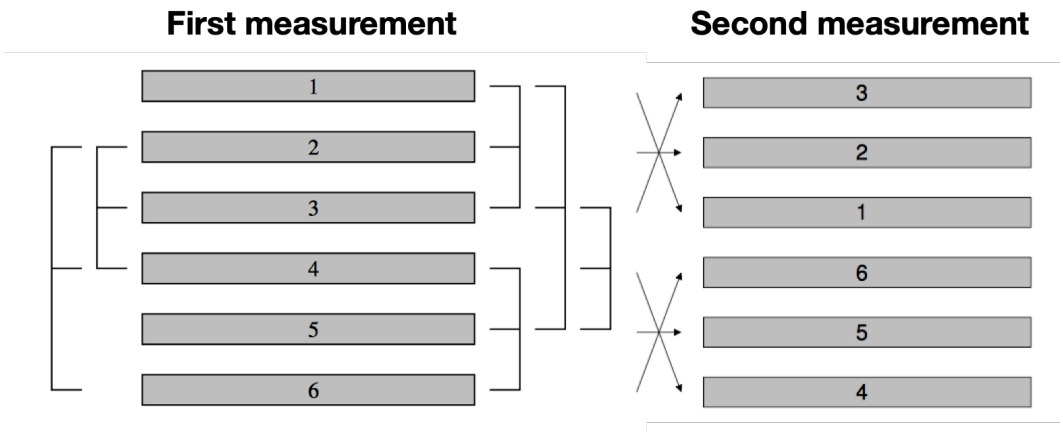

Figure A.4 Rearrangement of the six counters to symmetrize the system of equations with normal order and complementary order [87].

normal and the complementary order, there are twelve equations [87],

$$\begin{bmatrix} \sigma^2_{T(1,2,3)} \\ \sigma^2_{T(2,3,4)} \\ \sigma^2_{T(3,4,5)} \\ \sigma^2_{T(4,5,6)} \\ \sigma^2_{T(1,3,5)} \\ \sigma^2_{T(2,4,6)} \\ \sigma^2_{T(3,2,1)} \\ \sigma^2_{T(2,1,6)} \\ \sigma^2_{T(1,6,5)} \\ \sigma^2_{T(6,5,4)} \\ \sigma^2_{T(3,1,5)} \\ \sigma^2_{T(2,6,4)} \end{bmatrix} = \begin{bmatrix} \frac{1}{4} & 1 & \frac{1}{4} & 0 & 0 & 0 \\ 0 & \frac{1}{4} & 1 & \frac{1}{4} & 0 & 0 \\ 0 & 0 & \frac{1}{4} & 1 & \frac{1}{4} & 0 \\ 0 & 0 & 0 & \frac{1}{4} & 1 & \frac{1}{4} \\ \frac{1}{4} & 0 & 1 & 0 & \frac{1}{4} & 0 \\ 0 & \frac{1}{4} & 0 & 1 & 0 & \frac{1}{4} \\ \frac{1}{4} & 1 & \frac{1}{4} & 0 & 0 & 0 \\ 1 & \frac{1}{4} & 0 & 0 & 0 & \frac{1}{4} \\ \frac{1}{4} & 0 & 0 & 0 & \frac{1}{4} & 1 \\ 0 & 0 & 0 & \frac{1}{4} & 1 & \frac{1}{4} \\ 1 & 0 & \frac{1}{4} & 0 & \frac{1}{4} & 0 \\ 0 & \frac{1}{4} & 0 & \frac{1}{4} & 0 & 1 \end{bmatrix} \begin{bmatrix} \sigma^2_1 \\ \sigma^2_2 \\ \sigma^2_3 \\ \sigma^2_4 \\ \sigma^2_5 \\ \sigma^2_6 \end{bmatrix}. \tag{A.3}$$

The solution for the equations can be estimated by the method of linear equations. Figure A.5 shows examples of the time-resolution results along with the bar position for a short and a long bar. The time resolutions for the short bars are typically smaller than 50 ps, and for the long bars smaller than 60 ps. An overview of the time resolutions for all SPS detectors is given in Fig. 2.12.

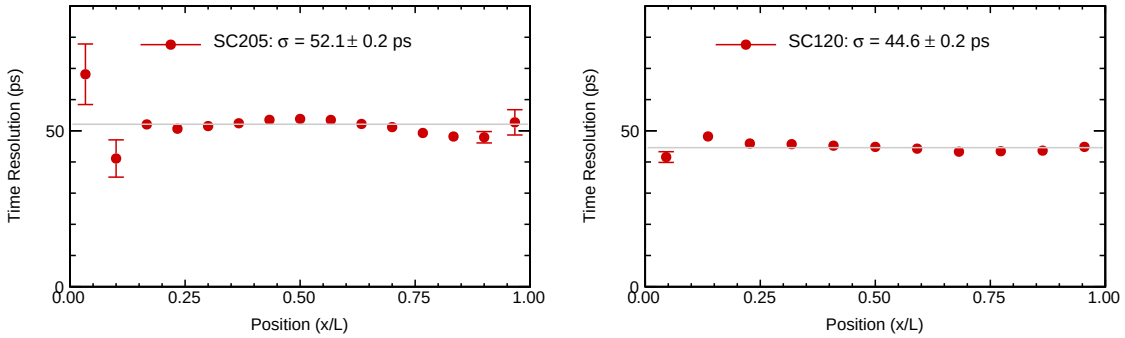

Figure A.5 Examples of time-resolution results from cosmic-ray measurements for a long bar (left) and for a short bar (right).